Application of Independent Component Analysis (ICA) in Pharmacokinetic Modeling of Tumors Using Dynamic Contrast Enhanced (DCE)-MRI

by

Hatef Mehrabian

A thesis submitted in conformity with the requirements
for the degree of Doctor of Philosophy

Department of Medical Biophysics

University of Toronto

Application of Independent Component Analysis (ICA) in Pharmacokinetic Modeling of Tumors Using Dynamic Contrast Enhanced (DCE)-MRI

Hatef Mehrabian

Doctor of Philosophy

Department of Medical Biophysics
University of Toronto

2014

Abstract

Dynamic contrast enhanced (DCE)-MRI combined with Pharmacokinetic (PK) modeling of a tumor tissue provides information about its perfusion and vascular permeability. These tumor characteristics have been shown to be related to prognostic factors and thus, their role as cancer biomarkers in assessing anti-angiogenic therapies is increasing. However, the quantitative parameters derived from PK analyses vary significantly between studies and need improvement.

Most PK models require the intravascular contrast agent concentration as an input. This vascular input function (VIF) is inseparable from the signal of extravascular extracellular space due to heterogeneity of tumor vasculature, partial volume effect, and low resolution of DCE-MRI. Thus, it is approximated with an arterial input function (AIF) measured outside of the tissue of interest (TOI). Variations and error in calculation of AIF is one of the major sources of discrepancy between PK parameters reported in different studies.

The objective of this thesis is developing image processing techniques to identify and separate the VIF at the TOI, which has the potential to improve PK analysis. Such VIF could also be used in cases no artery is available or in animal studies where finding an artery is difficult.

The thesis investigates feasibility of using independent component analysis for VIF calculation (using tissue-mimicking phantoms and animal models), and develops an adaptive complex independent component analysis (AC-ICA) algorithm to calculate the VIF and evaluates it using tissue-mimicking phantoms.

The AC-ICA algorithm is applied to DCE-MRI of prostate cancer and its performance in PK analysis is compared to AIF-based analyses. Results show the AC-ICA provides more consistent PK parameters and better separation of normal and tumor tissues. Moreover, the proposed VIF is less sensitive (compared to AIF) to decreasing temporal resolution which enables imaging with high spatial resolution that will further improve performance of both PK analysis and AC-ICA algorithm.

Acknowledgments

This thesis is dedicated to my wife Yasaman, and my parents Farideh and Ali. Without their continuous love and support I would never be able to reach this point in my life.

I would like to thank my advisor Dr. Anne L. Martel for her help, support, advice and encouragements throughout my PhD studies; she has been a great mentor for me. I am very grateful for the freedom that I was given to explore various research areas and encouragement and support that I received for participating in various workshops, conferences and scientific meeting during my PhD studies which enriched my knowledge and helped me better understand the field and also be exposed to novel ideas.

I also grateful to advisory committee members Dr. Greg Stanisz and Dr. Stephen Strother for their guidance, support, probing questions and suggestions during committee meetings and their help in my research in the past 5 years. The guidance that I received from them as well as my advisor paved the way for completion of my graduate studies.

I was fortunate to be involved in research with Dr. Masoom A. Haider and be exposed to his great vision in the field of prostate cancer. I am very grateful for the advice and suggestions that I received from him and the discussions that we had in several meetings and workshops in the past two years which directed me in the field of prostate cancer. I would also like to thank Dr. Michael Da Rosa for his help with the prostate cancer study.

Finally, I would like to highlight the contributions of Dr. Bojana Stefanovic and her group particularly Liis Lindvere for their collaborations at the early phases of my PhD and also the contributions from Dr. Rajiv Chopra and his group, particularly Dr. Chaitanya Chandrana and Ian Pang, which allowed me to explore my ideas and led to the main body of this thesis. I would also like to thank everyone at Martel group for their support.

Statement of Originality

I hereby certify that I am the sole author of this thesis and to the best of my knowledge, my thesis does not infringe upon anyone's copyright nor violates any proprietary rights, and that any ideas, techniques, quotations, or any other material from the work of other people included in my thesis, published or otherwise, are fully acknowledged in accordance with the standard referencing practices. The contributions of me and others to the thesis are listed below (these are acknowledged properly in their respective sections in the thesis):

1- The construction and DCE-MR imaging of the physical phantom presented in this thesis were performed by Ian Pang at Dr. Rajiv Chopra's Laboratory.

2- The VX2 tumor model development and its DCE-MRI and Ultrasound imaging were performed by Chaitanya Chandrana, John M. Hudson and Peter Bevan at Dr. Rajiv Chopra's laboratory.

3- The Multi-parametric MR imaging of prostate cancer patients were performed at Sunnybrook Health Sciences Centre and were provided by Dr. Masoom A. Haider.

4- All the ideas, analyses and experiments (excluding those mentioned above) that are presented in the thesis, such as construction of the numerical tissue-mimicking phantom and its DCE-MR images, development of vascular input function separation algorithms and their assessment techniques, pharmacokinetic analysis of prostate tissues, etc., were performed by me.

Table of Contents

List of Tables

List of Figures

List of Appendices

List of Abbreviations and Symbols

AATH	Adiabatic Approximation to Tissue Homogeneity
AC-ICA	Adaptive Complex Independent Component Analysis
ADC	Apparent Diffusion Coefficient
AIF	Arterial Input Function
ANOVA	Analysis of Variance
AUC	Area Under the Curve
BSS	Blind Source Separation
BW	Band Width
CA125	Cancer Antigen 125
CE-US	Contrast Enhanced Ultrasound
CT	Computed Tomography
CZ	Central Zone
DCE-MRI	Dynamic Contrast Enhanced-Magnetic Resonance Imaging
DNA	Deoxyribonucleic Acid
DRE	Digital Rectal Examination
DWI	Diffusion Weighted Imaging
DW-MRI	Diffusion Weighted Magnetic Resonance Imaging
EC	Endothelial Cell
EES	Extravascular Extracellular Space
EM	Expectation Maximization
FA	Flip Angle
FADS	Factor Analysis of Dynamic Structures
FDG-PET	Fludeoxyglucose-Positron Emission Tomography
FEA	Finite Element Analysis
FOV	Field Of View
fSPGR	fast Spoiled Gradient Recalled
FT	Fourier Transform

FWHM	Full Width at Half Maximum
Gd-DTPA	Gadolinium with diethylenetriaminepentacetate
GGD	Generalized Gaussian distribution
HIF	Hypoxia Inducible transcription Factor
IC	Independent Component
ICA	Independent Component Analysis
IFP	Interstitial Fluid Pressure
IR- SE	Inversion Recovery Spin Echo
Mag-ICA	Magnitude Independent Component Analysis
MI	Mechanical Index
MR	Magnetic Resonance
MRI	Magnetic Resonance Imaging
MRS	MR Spectroscopy
NEX	Number of Excitations
NMF	Non-negative Matrix Factorization
Nx	Number of frequency encoding steps
Ny	Number of phase encoding steps
PCA	Principal Component Analysis
pdf	Probability Density Function
PET	Positron Emission Tomography
PHD	Prolyl Hydroxylase Domain proteins
PIN	Prostatic Intraepithelial Neoplasia
PK	Pharmacokinetic
ppm	Parts Per Million
PSA	Prostate Specific Antigen
PW-MRI	Perfusion Weighted MRI
PZ	Peripheral Zone
QUS	Quantitative Ultrasound
RECIST	Response Evaluation Criteria In Solid Tumors
RF	Radio Frequency
RMSE	Root Mean Square Error

RNA	Ribonucleic Acid
ROI	Region Of Interest
SE	Spin Echo
SNR	Signal to Noise Ratio
SPGR	Spoiled Gradient Recalled
SVD	Singular Value Decomposition
TE	Echo Time
TH	Tissue Homogeneity
TI	Inversion Time
TOI	Tissue Of Interest
TR	Repetition Time
TRUS	Transrectal Ultrasound
U.S.	United States
US	Ultrasound
VE	Vascular Endothelial
VEGF	Vascular Endothelial Growth Factor
VEGF-A	Vascular Endothelial Growth Factor A
VEGFR2	VEGF Receptor
VIF	Vascular Input Function
v_e	EES volume
v_p	plasma-space volume
c_a	Artery concentration
c_p	Plasma concentration
c_e	Concentration at extravascular extracellular space
c_t	Tissue concentration
J	Indicator flux
F_p	Plasma flow
PS	Permeability surface area product of the capillary wall
E	Extraction fraction
K^{trans}	Volume transfer constant
K_{ep}	EES to plasma rate constant

T_{10}	Pre-contrast longitudinal relaxation
T_{20}	Pre-contrast transverse relaxation
R_1	Longitudinal relaxivity of contrast agent
R_2	Transverse relaxivity of contrast agent
B	Diffusion gradient b-value
λ	Lagrange multiplier
H_J	Complex Hessian matrix of J.
∇_J	Complex gradient matrix of J.
C^*	Complex conjugate of C
C'	First derivative of C
C''	Second derivative of C
N_r	Number of rows
N_c	Number of columns
Γ	Gamma function
ψ	Polygamma function
ω	Delay in contrast agent arrival

Academic Curriculum Vitae

The work presented in this thesis is based on the following publications:

Peer-reviewed Journal Publications

[1] **Mehrabian, H.,** Haider, M. A., and Martel, A. L., "Pharmacokinetic Analysis of Prostate tissue in dynamic contrast enhanced MRI using Independent Component Analysis", *Submitted to the journal of Magnetic Resonance Imaging*.

[2] **Mehrabian, H.,** Chopra, R., and Martel, A. L., "Calculation of intravascular signal in dynamic contrast enhanced MRI using adaptive complex independent component analysis", *IEEE Transactions on Medical Imaging*, 32(4), pp. 699-710, (2013).

[3] **Mehrabian, H.,** Chandrana, C., Pang, I., Chopra, R., and Martel, A. L., "Arterial input function calculation in dynamic contrast-enhanced MRI: an in vivo validation study using co-registered contrast-enhanced ultrasound imaging", *European Radiology* 22 (8) , pp. 1735-1747, (2012).

[4] **Mehrabian, H.**, Lindvere, L., Stefanovic, B., and Martel, A. L., "A constrained independent component analysis technique for artery-vein separation of two-photon laser scanning microscopy images of the cerebral microvasculature", *Medical Image Analysis*, 16 (1) , pp. 239-251, (2012).

Conference Proceedings

[5] **Mehrabian, H.,** Haider, M. A., and Martel, A. L., "Using Independent components analysis to calculate intravascular contrast agent concentration in prostate cancer", *Biomedical Imaging: From Nano to Macro, IEEE International Symposium on,* San Francisco, CA, USA, April 7-11, (2013).

[6] **Mehrabian, H.,** Pang, I., Chopra, R., and Martel, A. L., "An adaptive complex independent component analysis to analyze dynamic contrast enhanced-MRI", *Biomedical Imaging: From Nano to Macro, IEEE International Symposium on,* Barcelona, Spain, May2-5, (2012).

[7] **Mehrabian, H.,** Pang, I., Chandrana, C., Chopra, R., Martel, A.L., "Automatic mask generation using independent component analysis in dynamic contrast enhanced-MRI", *Biomedical Imaging: From Nano to Macro, IEEE International Symposium on ,* Chicago, IL, USA, March 30 - April 2, (2011).

[8] **Mehrabian, H.,** Lindvere, L., Stefanovic, B., and Martel, A. L., "Deconvolution of dynamic dual photon microscopy images of cerebral microvasculature to assess the hemodynamic status of the brain", in *Medical Imaging 2011: Biomedical Applications in Molecular, Structural, and Functional Imaging, Proceedings of SPIE* Vol. 7965 (2011) 79650A-1.

[9] **Mehrabian, H.,** Lindvere, L., Stefanovic, B., and Martel, A. L., "A temporally constrained ICA (TCICA) technique for artery-vein separation of cerebral microvasculature", in *Medical Imaging 2010: Biomedical Applications in Molecular, Structural, and Functional Imaging, Proceedings of SPIE* Vol. 7626 (2010) 762622.

Abstracts

[10] **Mehrabian, H.,** Haider, M. A., and Martel, A. L., "Assessing the effects of decreasing temporal resolution in pharmacokinetic analysis using a local vascular input function", *submitted to the international society for magnetic resonance in medicine (ISMRM) annual meeting*, Milan, Italy, 10-16 May, (2014)

[11] **Mehrabian, H.,** Haider, M. A., and Martel, A. L., "Local vascular input function for pharmacokinetic modeling of prostate cancer", *submitted to the international society of magnetic resonance for medicine (ISMRM) annual meeting*, Milan, Italy, 10-16 May, (2014)

[12]   **Mehrabian, H.,** Haider, M. A., and Martel, A. L., "Local vascular input function (VIF) calculation for prostate cancer assessment", *Imaging Applications in Prostate Cancer Workshop, London, ON, Canada* November 15, (2013)

[13]   **Mehrabian, H.,** Haider, M. A., and Martel, A. L., "Pharmacokinetic analysis of prostate cancer using independent components analysis", *Imaging Applications in Prostate Cancer Workshop,* London, ON, *Canada* November 16, (2012)

[14]   **Mehrabian, H**., Chandrana, C., Pang, I., Chopra, R., and Martel, A. L., "Calculating arterial input function in dynamic contrast enhanced-MRI of tumors: A validation study", ***Invited to*** *the Canadian Student Health Research Forum (CSHRF).* Winnipeg, MB, Canada, June 12-14, (2012).

[15]   **Mehrabian, H.**, Pang, I., Chandrana, C., Chopra, R., Martel, A.L., "Application of Independent Component Analysis (ICA) to Identify and Separate Tumor Arterial Input Function (AIF) in Dynamic Contrast Enhanced MRI", *Fields-MITACS: Conference on Mathematics of Medical,* Toronto, ON, Canada, June 20-24, (2011)

Chapter 1

Introduction and Motivation

Advances in our understanding of cancer biology have resulted in the development of novel therapeutics with the capability to target diseases based on their molecular characteristics. Given the specificity and cost of these approaches, proper selection of patients who would benefit from these treatments is essential. In addition, the ability to determine the response of a tumor to treatment early in the course of the therapy helps adjust the course of the treatment [1], [2]. Currently, imaging measurements of tumor size and evaluation of serum markers secreted by cancer cells are the two main approaches used clinically to assess therapeutic response. Serum markers are non-invasive, can be repeated frequently and have low cost. They are used routinely to monitor several cancers such as prostate cancer (prostate specific antigen or PSA) [3], ovarian cancer (cancer antigen 125 or CA125) [4], and thyroid cancer (thyroglobulin) [5]. However, the level of tumor serum markers is not regulated by the tumor mass only and other normal processes also affect their level. For instance, PSA is regulated by androgen level confounding its use in monitoring anti-hormonal therapies [3], or thyroglobulin level is regulated by thyroid stimulating hormone [5]. In addition, many malignancies do not produce sufficient markers to be used for monitoring [1]. Consequently, tumor size measurement with imaging has become the standard approach to evaluate tumor response [1]. This response evaluation criteria in solid tumors (RECIST) [6] assumes that reduction in tumor size after therapy shows better prognosis than no change or increase in tumor size. Despite its broad adoption, this assumption is not necessarily correct [7] and has some limitations as some molecular targeting agents may result in improved clinical response while making no significant change in tumor size [8].

Due to the limitations of current tumor therapeutic response assessment criteria, there has been significant interest in functional and molecular imaging techniques. Molecular imaging with PET has been shown to improve therapeutic response assessment for several tumors [9]–[12] and when combined with compartmental modeling enables studying biological changes

in the tumor [13]. Contrast enhanced ultrasound provides quantitative information about tumor vasculature [14], and dynamic contrast enhanced (DCE)-computed tomography (CT) is used to quantify vascular permeability and blood flow [15]. Non-contrast T_1-weighted or T_2-weighted MRI imaging provides information about morphological changes in the tumor or changes in its fluid content. Diffusion weighted MRI and perfusion weighted MRI also provide promising tools for response assessment [16], [17]. DCE-MRI, similar to DCE-CT, provides information on the vascular permeability and tumor perfusion [18] and will be used in this thesis to obtain quantitative information about the tumor.

This chapter provides the introductory information and literature review on the quantification of DCE-MRI in assessing tumor response to therapy using pharmacokinetic analysis. It will first discuss tumor angiogenesis which is different from normal angiogenesis and which could be used as a cancer biomarker. Quantitative information about this biomarker could be obtained by analyzing kinetics of tracer transport in tumor vasculature (e.g. passage of a contrast agent bolus through the vasculature). The tracer kinetic models that are used for such quantification will also be explained in this chapter. The objective of this thesis which is to calculate the vascular input function required in tracer kinetic models, will be introduced. The approaches that are currently used to acquire an input function as well as the possibility of utilizing a data-driven technique to calculate the vascular input function will be discussed. Finally, a prostate cancer model, which will be used as a clinical example to assess the performance of our proposed method, will be introduced.

1.1 Cancer Biomarkers

Cancer is a disease in which abnormal cells are able to proliferate without control and have the potential to invade other tissues. These cancerous cells can spread to other organs through blood vessels and the lymphatic system. There are more than 100 types of cancers that could be grouped into Carcinoma, Sarcoma, Leukemia, Lymphoma and Myeloma, and central nervous system cancers [19].

The main biological capabilities that a cancer acquires in the process of developing tumors are sustaining proliferative signaling, evading growth suppressors, resisting cell death, enabling replicative immortality, inducing angiogenesis, and activating invasion and metastasis [20]. In addition to these cancer cell characteristics, tumors contain a collection of normal cells that create the "tumor microenvironment" which provide the environment for cells to become cancerous [21]. The tumor microenvironment includes several components

2

including blood vessels (discussed in the next section) and the extracellular matrix [22], and is used to measure several cancer biomarkers.

Cancer biomarkers are substances secreted by the tumor or processes that can be used as indicators of presence of tumor in the body such as a molecule or an imaging metric that provides an objective measure of a pathological process [23]. In general, any biologically driven substance or molecule that could provide information about the presence or stage of cancer is considered as a cancer biomarker [24]. These biomarkers can be categorized based on the disease state (prediction, detection, diagnosis, and prognosis biomarkers), the bio-molecules (DNA, RNA, protein, glyco biomarkers) or other criteria such as imaging biomarkers or pathological biomarkers.

However, very few cancer biomarkers are sensitive or specific enough for cancer detection and assessing its response to therapy. There are challenges in validating these biomarkers in early detection, diagnosis or monitoring of the disease which prevents them from being used in routine clinical practices and thus more research is required to address these issues. The focus of this thesis is on improving the accuracy of imaging biomarkers that are based on the pharmacokinetics of tracers in the vascular network, and exploiting the differences between tumor and normal vasculature. The remainder of this subsection first briefly reviews the vascular network and microcirculatory system and then explains angiogenesis and the differences in normal and tumor angiogenesis that can be used in cancer studies.

1.1.1 Vascular Network

The blood circulatory system is a network of blood vessels that transports newly oxygenated blood as well as other nutrients to the cells that need them. As nutrients diffuse out of the blood into the interstitial fluid, waste diffuses back into the blood stream and is carried away. This blood transports waste to the liver or kidneys and moves back to the lungs to become oxygenated again.

The heart, blood and the vascular network (comprised of arteries, arterioles, capillaries, venules and veins) form the human circulatory system. There are three major types of blood vessels: the arteries that carry blood away from the heart, the capillaries which enable the exchange of nutrients and oxygen and other chemicals between the blood and the tissue, and the veins that carry blood away from the capillaries and back to the heart. The transport of

substances between blood and tissue occurs only in the capillaries that have a thin endothelium and are a component of microcirculatory network.

1.1.2 Microcirculation

Microcirculation, whose main function is delivering oxygen and nutrients and removing waste, is essential to many functions of the organism. It also plays an important role in fluid exchange between blood and tissue, delivery of hormones to target organs, and bulk delivery between organs. The microcirculatory system consists of three principal sections, arterioles, capillaries and venules; each with unique structure and function. The arterioles are innervated and surrounded by smooth muscle cells and are responsible for carrying blood to the tissue and regulating the rate of delivery. Capillaries are not innervated and have very thin walls with no smooth muscle cells and are responsible for exchange between blood and tissue. The venules drain blood from capillaries for return to the heart.

In addition to the blood vessels, the microcirculatory system includes the lymphatic capillaries and the collecting ducts. The main functions of the microcirculation are regulating blood flow, tissue perfusion, blood pressure, tissue fluid and body temperature, as well as delivery of oxygen and nutrients to the tissue and removal of carbon dioxide and other metabolic waste from the tissue [25]. The process of generating new blood vessels to maintain the circulatory system, which is essential for any new or growing organ, is called angiogenesis and has fundamental differences between normal and cancerous tissues.

1.1.3 Angiogenesis

The vascular network transports oxygen and nutrients that are essential for growth and survival of cells. The diffusion distance of oxygen in tissue is 100 [μm] to 200 [μm] and therefore cells have to be located not farther than this diffusion distance to survive. As a multi-cellular organism is growing it must recruit new blood vessels to support the new cells. Thus, the process of generating new blood vessel (angiogenesis) plays a crucial role in the growth of the organ.

Angiogenesis is important for the establishment of a well organized, heterogeneous vascular network as an organ grows. It is also one of the main factors of wound healing and tissue repair. When angiogenesis is taking place in normal tissues, the start and end of angiogenesis are tightly regulated and controlled by several molecular and mechanical factors [26], [27].

As such, the result of angiogenesis is a tissue-specific, structured, vascular tree that is optimized to meet the needs of the cells in the organ. Tumor angiogenesis on the other hand lacks most of these regulatory mechanisms and has fundamental differences with normal angiogenesis.

1.1.3.1 Tumor angiogenesis

Tumor angiogenesis was first observed around 100 years ago where several scientists such as Ferrara [19] and Hurwitz [20] confirmed the importance of abundant blood supply for tumor growth. In 1971 Folkman [28] suggested that a tumor could be starved to death if key molecular pathways of angiogenesis were identified. A few years later in 1978, Guliano [29] showed that precancerous cells acquire angiogenic capacity as they become cancerous. Since these findings, there have been numerous studies on identification of anti-angionegic mechanisms. These studies attempt to slow or stop the tumor angiogenic processes where the tumor either engulfs existing blood vessels to get their nutrients or generates new blood vessels using one of the following 3 methods:

1- Generating new blood vessels emerging from existing blood vessels (Angiogenesis).
2- Using bone marrow-derived endothelial progenitor cells (Vasculogenesis).
3- Expanding the capillary wall into the lumen to split a single blood vessel into two blood vessels (Intussusception).

However, tumor angiogenesis is not just a production of new blood vessels to feed growing tumor mass. Unlike normal angiogenesis which is tightly regulated, tumor angiogenesis occurs in an unregulated manner such that the resultant tumor vasculature is highly abnormal. One of the main characteristics of solid tumors is that they are hypoxic which reduces the activity of prolyl hydroxylase domain proteins (PHD) that act as oxygen sensors [30], [31]. This reduction in PHD affects the ubiquitination and degradation of hypoxia inducible transcription factor (HIF) [32] and allows the transcription of HIF-driven genes such as vascular endothelial growth factor (VEGF) which is a pro-angiogenic factor. Over expression of VEGF in tumors can also be initiated by other factors such as inflammatory cytokines, sex hormones, growth factors, and chemokines [33], [34]. The imbalance between the pro-angiogenic, such as vascular endothelial growth factor A (VEGF-A), and anti-angiogenic signaling in tumors causes unregulated production of new vasculature that are both macroscopically and microscopically abnormal. Presence of such an abnormal vascular

network significantly alters the way tumors grow and deal with the immune system, metastasize and respond to therapy.

1.1.3.2 Microscopic Abnormalities (vessel wall)

The mature endothelial cells (ECs) lining normal vessel walls are connected to the neighboring ECs with adherin junctions such as vascular endothelial (VE)-cadherin, which is a transmembrane receptor [35]. The proteins that connect the intracellular domain of VE-cadherin attached to the EC cytoskeleton also act as effectors of downstream molecular signaling. The downstream signaling from VEGF-VEGFR2 interactions contracts the EC cytoskeleton and weakens the VE-adherin junctions [35]. Thus, tumor ECs are poorly connected which leads to having irregular and disorganized morphology. Moreover, tumors express abundance of vesiculo-vascular organelles that are associated with vascular permeability. Tumor ECs also demonstrate a different gene expression profile compared to normal endothelium [36]. All of these factors contribute to the hyper-permeability of tumor blood vessels which allows the intravascular fluids and proteins to extravasate [37]. Considering that tumors lack a functional lymphatic system to clear the interstitial space, the extravasated substances build up and elevate the interstitial fluid pressure (IFP). This elevated IFP reduces the pressure gradient between the intravascular and extravascular spaces such that they reach equilibrium and the transvascular flow decreases.

1.1.3.3 Macroscopic Abnormalities (Morphology)

The macroscopic characteristics of tumor microvasculature include being dilated, tortuous, saccular, and having random branching and interconnections with random patterns of locally increased or reduced vessel density [37]–[40] (as shown in Figure 1-1 [41]). Tumor vasculature also expresses increased vascular shunting due to loss of vascular diameter control, high tendency for vessel growth and increased vascular reactivity [42], [43]. The heterogeneous and irregular arrangement and distribution of the blood vessels in the tumor leads to heterogeneity in blood flow both spatially and temporally.

The elevated IFP and the stress from the proliferating tumor cells cause collapse of the vessel walls [44]. All of these factors (elevated IFP, areas of poor perfusion and vessel collapse) lead to having regional hypoxia in the tumor [45]. Consequently, tumor cells undergo epigenetic changes in hypoxic conditions and become more resistant to hypoxia than normal cells. These resistant to hypoxia tumor cells demonstrate characteristics of malignant tumors

6

and have greater potential to metastasize [35], [46]. Some of the macroscopic abnormalities of the tumor vasculature such as the vascular leakiness are quantified using medical imaging to generate imaging biomarkers for tumor stage or therapeutic response assessment.
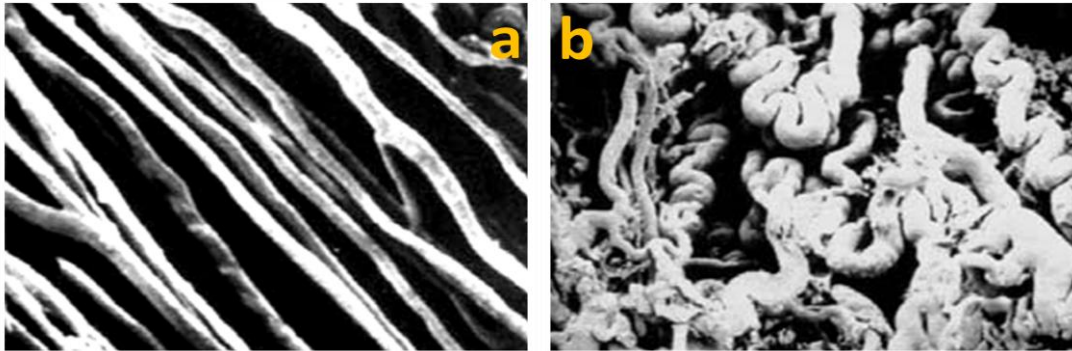
Figure 1-1 a) Normal vasculature of skeletal muscle that is well-organized with regular arrangement of the blood vessels, b) Tumor microvasculature (Sarcoma) that is incomplete, heterogeneous, and tortuous. Images reprinted with permission from Elsevier: Vaupel *et al.*, "Tumor microenvironmental physiology and its implications for radiation oncology", *Seminars in radiation oncology*, 14(3):198-206, © (2004).

1.2 Medical Imaging Biomarkers

Using imaging biomarkers in detection, diagnosis, staging and assessment of the therapeutic response of tumors is becoming important in cancer studies, particularly with the emerging trend towards personalized medicine. A major advantage of imaging biomarkers is that, unlike bio-fluids that measure information about the entire body, imaging biomarkers assess the exact focus of the disease. They are also generally non-invasive and allow follow up. The type of information that an imaging biomarker provides depends on the question it is trying to address, for instance therapeutic response assessment biomarkers include (but are not limited to) biomarkers that assess whether the drug has arrived in the target, whether it modulates its target, whether the dose is selected appropriately, and whether it changes tumor pharmacokinetics [24], [47].

There exist a wide variety of imaging biomarkers, where each biomarker provides information about a specific biological or physiological characteristic of the tumor (some of these biomarkers will be mentioned in section 1.2.1.2). However, there are several sources of uncertainty in imaging biomarkers (e.g. biological, imaging and analysis uncertainties) that limit their applicability and have to be resolved or optimized before using them in routine clinical decision making. Biological uncertainties are drug and patient dependent and thus, difficult to assess. Reliability and robustness of image acquisition procedures and analysis

tools used for quantitative measurement of the changes in the tumor as well as the clinicians that are interpreting the images are other sources of uncertainty in imaging biomarkers [48].

1.2.1 Assessing tumor response to therapy

Personalized therapy is becoming more viable as our understanding of cancer biology is increasing. Given the complexity and high cost of these therapies it is of upmost importance to identify responding and non-responding patients as early as possible in the course of the treatment [49]. However, there is large heterogeneity in tumors and although they present apparently identical clinical characteristics, tumor response to therapy is a fundamental but not well understood concept in clinical oncology. Currently there are two approaches that are used in clinical practices to assess tumor response to therapy:

1-   Measurement of markers secreted by cancer cells

2-   Tumor size measurements using medical imaging (RECIST criteria)

Some malignant tumors produce serum molecules at a level sufficient for monitoring[3]–[5], however the secretion of these biomarkers is not controlled by the tumor alone and several other factors affect their level which limits their application for therapy monitoring [3], [5]. Moreover, many malignant tumors do not produce biomarkers at sufficient level to be used in response assessment and thus tumor size measurement has become the main response assessment approach in clinical practice [1].

1.2.1.1 RECIST criteria

Currently the most commonly used marker for response assessment is tumor size measurement. The first international standards criteria based on tumor size measurement was published in 1979 [50], which was modified in 2000 and was called response evaluation criteria in solid tumor (RECIST) [51]. However, despite the advances in medical imaging, the definition for assessing tumor response to therapy has not changed. The RECIST criterion categorizes a tumor into one of the following 4 groups:

- **Complete response (CR)**: Disappearance of all known disease
- **Partial response (PR)**: At least 30% reduction in tumor size
- **Stable disease (SD)**: Patient does not meet criteria for CR or PR
- **Progressive disease (PD)**: 20% or more increase in tumor size with reference to the smallest size measured since the start of the treatment

The main assumption in using tumor size to assess tumor response to therapy is that reduction in tumor size after therapy indicates a better prognostic outcome than unchanged or increasing tumor size. This assumption is not necessarily correct as some molecular targeting agents may result in improved clinical response without affecting the tumor size [7], [52]. There are several drugs such as Sorafenib in renal cancer [53], Panitumumab in colorectal cancer [54], and Sunitinib in pancreatic cancer [55], that have been approved by U.S. Food and Drug Administration despite resulting in 10% or less change in tumor size which would not be approved if RECIST end points were used [52]. More importantly it may take a long time (several weeks or months) for the tumor size to change as a result of the therapy [56] which jeopardizes the ability to change or adjust the course of treatment. Moreover, the tumor size measurement may be inaccurate due to errors in tumor measurements, differentiation of tumor from the surrounding tissue, and inter-observer and intra-observer variability [52].

1.2.1.2 Quantitative Imaging

Due to the limitations in current therapeutic response assessment methods there has been significant interest in functional and molecular imaging techniques such as positron emission tomography with ^{18}F-fluorodeoxyglucose (FDG-PET) [8] and magnetic resonance imaging (MRI: non-contrast, T1/T2-weighted, diffusion-weighted, perfusion-weighted and dynamic contrast-enhanced) [9], [18], ultrasound (US) and computed tomography (CT). Such biomarkers, if correlated with patient outcome, could identify the responding patient to a specific treatment and significantly reduce the treatment cost. There are a large number of quantitative imaging biomarkers that are being used in clinic or are in research stages, that have been found useful in cancer assessment. Some of these quantitative cancer biomarkers are listed below:

- Texture analysis in computed tomography (CT) is used for assessing tumor heterogeneity [57]. CT perfusion imaging is used to assess the tumor vascularity [58]. Dynamic contrast enhanced (DCE)-CT combined with pharmacokinetic modeling of the tumor tissue is also used for quantifying tumor blood flow, tumor perfusion and vascular permeability [15].
- Positron emission tomography (PET) is widely used for metabolic assessment of cancer. Static FDG-PET imaging is used for measuring energy consumption in tumors and is used for detecting metastatic cancers [59]. Dynamic PET combined with compartmental modeling is also used for assessing biological changes using a tracer injection [13].

9

- Quantitative ultrasound (QUS) analyzes power distribution from the signals backscattered from the tissue. The spectral parameters calculated using QUS are used to characterize and distinguish between tumors particularly in prostate, breast and metastatic cancer in lymph nodes [60]. Contrast enhanced ultrasound on the other hand provides information about tumor vasculature such at its perfusion and vascular heterogeneity [14].

- MRI provides anatomical, functional and molecular information to assess response to therapy [61]. Non-contrast T_1- and T_2-weighted MRI provide information about tissue morphology, fluid content and fibrosis, while dynamic contrast enhanced (DCE)-MRI provides information about blood flow, perfusion and vascular permeability [18]. Other MR imaging techniques such as diffusion weighted (DW)-MRI, perfusion weighted (PW)-MRI and magnetic resonance spectroscopy (MRS) also provide promising functional and molecular imaging biomarkers [16], [17], [62].

The focus of this thesis is on the vascular permeability biomarkers that are extracted from DCE-MR imaging of the tumor tissue.

1.2.2 Pharmacokinetic modeling

Pharmacokinetic (PK) modeling of a tissue models the passage of a bolus of contrast agent through the tumor vasculature and provides quantitative information about its physiology such as the exchange rate of substances through the vasculature into the extravascular extracellular space. This quantitative information is used for detecting and diagnosing tumors as well as assessing their response to therapy.

Modeling the bolus passage through vascular network can be performed using contrast enhanced ultrasound (CE-US), DCE-CT, DCE-MRI and dynamic PET. However, Ultrasound contrast agents, i.e. microbubbles, are too large to pass through the vessel walls and thus stay intravascular which could provide information about tumor vasculature and perfusion. In addition to the limit in the contrast agent dose that can be administered in DCE-CT, it involves ionizing radiation which leads to compromises in the image contrast (low signal to noise ratio), coverage volume and the number of time points in the DCE-CT series [15], [63]. Moreover, there is higher incidence of adverse effects of CT contrast agent compared to MRI [15]. These issues limit the application of DCE-CT despite the major advantage it has compared to MRI, i.e. linear relationship between tissue attenuation and contrast agent

concentration. Dynamic PET, despite having high sensitivity and specificity, uses radionuclides as its tracer (dose limitations) and suffers from low spatial resolution [13].

DCE-MRI on the other hand is suitable for pharmacokinetic modeling of tumor tissues as it does not involve ionizing radiation, it has high spatial and temporal resolutions, and its contrast agent is not radioactive and is capable of crossing the vessel walls. As a result of these advantages, although DCE-MRI has several practical implementation vulnerabilities (e.g. non-linear relationship between MRI signal and contrast agent concentration, difficulty and error in T_1 measurement, tissue-dependant relaxivities, water exchange and incomplete mixing of the extravascular compartment [15]), there has been more than 100 early-phase clinical trial and investigator-lead studies assessing anti-vascular therapies that used end points based on DCE-MRI [64].

In DCE-MRI studies, the injected contrast agent has a low molecular weight (e.g. Magnevist, Onmiscan) and can diffuse through the vessel walls into the extravascular space. However, these contrast agent molecules are too large to the cross cell membrane and can only diffuse into the extravascular extracellular space (EES). The rate by which the contrast agent diffuses from blood plasma to the EES is determined by the blood flow, vascular permeability, and surface area of the vessel. PK modeling of DCE-MRI data provides quantitative information about these characteristics of the tumor vasculature (e.g. microvessel density and permeability [65], [66]) that have been shown to correlate with prognostic factors. The following section introduces the tracer-kinetic theory from which the pharmacokinetic models are derived. It will also explain some of the most common PK models that are used in DCE-MRI studies.

1.3 Tracer-Kinetic Theory

A tracer or indicator is a substance administered into a physiological system that could provide physiological information about the system such as Gadolinium-based MR contrast agents. The kinetics of an indicator in the body can be explained using the tracer-kinetic theory of linear and stationary systems [67]–[69]. Consider a tissue sample which has several inlets and outlets that transport tracers into and out of the tissue. Tissue concentration c_t [mMol], is defined as the mass of indicator in the tissue divided by the volume of the tissue. Indicator flux, $J \left[\frac{mMol}{min \cdot ml} \right]$, is defined as a non-negative quantity (unidirectional flux) that measures the amount of indicator that passes through an inlet or outlet per unit time [70].

11

Based on the mass continuity equation (equation 1-1), the difference between the total influx and outflux of the contrast agent equals the rate of change of the total amount of contrast agent in any section of the tissue:

$$\frac{\partial c_t(t,x)}{\partial t} = -\nabla J(t,x)$$
$$= \sum_{i \in inlets} J_i(t,x) - \sum_{o \in outlets} J_o(t,x) \qquad (1\text{-}1)$$

There are several tissue models that have been designed to model kinetics of an indicator in a tissue. In this section we will explain the exchange model [67] and its special forms that are known as Tofts-Kety models [71], [72], tissue homogeneity model [73] and the adiabatic approximation to tissue homogeneity model [74], and distributed parameter model [75]

These models that are commonly used in modeling the indicator kinetics in a two-region system (some of these models can be generalized to multi-region systems as well) are all based on the mass continuity equation (equation 1-1)

1.3.1 Two-region models

The exchange of MR contrast agent through the capillary wall can be modeled in most cases using a two-region system consisting of the plasma space and the extravascular extracellular space (EES) as shown in Figure 1-2. Once the contrast agent arrives in the capillary via the influx J_a, its particles pass through the capillary wall into the EES (they do not cross the cell membrane and stay extracellular) and eventually return to the capillary bed. Such a coupling could be modeled with an influx from the EES into the plasma space, J_l, and an outflux from the plasma space into the EES, J_e. Finally the contrast agent leaves the capillary through the outflux J_v. In such a two-region system the tissue concentration c_t, is the sum of the contribution of each space:

$$c_t(t) = v_p c_p(t) + v_e c_e(t) \qquad (1\text{-}2)$$

where v_p [ml/ml] (plasma-space fraction) is the volume of distribution for c_p (volume of the plasma space) divided by the total volume of the tissue, and c_p is the indicator concentration in the plasma space (amount of indicator in the plasma space divided by its volume of distribution), v_e $\left[\frac{ml}{ml}\right]$ is the fraction of the tissue that is extravascular extracellular, and c_e is the indicator concentration in EES. The exchange of indicator between the capillary bed and the EES can be modeled using a compartment model or a plug flow model. Both models have

12

the same assumption regarding transport of indicator across the capillary wall and only differ in the distribution of the indicator in the tissue.
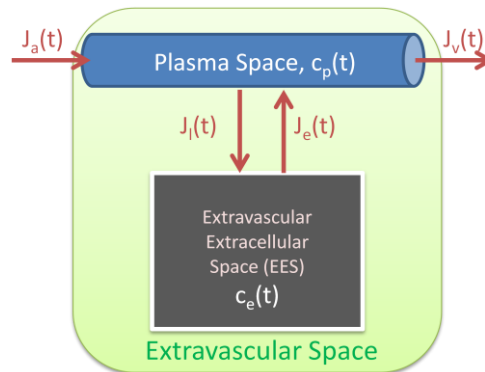
Figure 1-2 The schematic of a generic two region exchange system showing the influxes, outfluxes and the different spaces

1.3.1.1 Exchange Model

In exchange models each space is assumed to be a compartment. In a compartment (Figure 1-3b) it is assumed that as the indicator arrives in the compartment (capillary) it instantaneously mixes with the blood plasma and produces a homogeneous mixture. Thus, the concentrations at all outlets are c_p or in other words $J_v = F_p c_p(t)$ where $F_p \left[\frac{ml}{min \cdot ml}\right]$ is the plasma flow, and $J_l = PSc_p(t)$, where PS is the product of permeability $(P \left[\frac{ml}{min \cdot cm^2}\right])$ and surface area $(S \left[\frac{cm^2}{ml}\right])$ of the capillary wall. Substituting these fluxes in the mass continuity equation (equation 1-1) for the capillary compartment we have:

$$v_p \frac{dc_p}{dt}(t) = F_p c_a(t) - F_p c_p(t) - PSc_p(t) \qquad (1-3)$$

A two compartment exchange model assumes that both the plasma and the EES are compartments [67]. Applying the mass conservation equation to this system (Figure 1-4a), the following two equations (1-4 and 1-5) are derived that govern the exchange of contrast agent between the plasma space and the EES:

$$v_p \frac{dc_p}{dt}(t) = F_p c_a(t) - F_p c_p(t) + PSc_e(t) - PSc_p(t) \qquad (1-4)$$

$$v_e \frac{dc_e}{dt}(t) = PSc_p(t) - PSc_e(t) \qquad (1-5)$$

13

1.3.1.2 Tissue Homogeneity (TH) Model

Tissue homogeneity (TH) models [73] assume the plasma space is a plug flow system which is shown in Figure 1-3c. In a plug flow system it is assumed that all particles in the fluid have the same velocity in the direction parallel to the capillary (axial direction) and have zero velocity in the perpendicular direction (radial direction). Thus, the concentration does not change perpendicular to the capillary (radial) and can be expressed as a one-dimensional axial variation. If we consider an infinitesimal segment dx of the capillary at location x along the capillary, the concentration is $c_p(x,t)$ and could be assumed to be constant for the entire infinitesimal segment dx. Thus the outflux from the segment is $J_o = F_p c_p(x,t)$ and the influx is $J_i = F_p c_p(x - dx, t)$, the outflux through the capillary wall is $J_l = PS c_p(x,t)dx/L$ (L [m] is the capillary length), the total concentration of the segment is $c_p(x,t)dx/L$, the volume of the segment is $v_p dx/L$, and the surface area is Sdx/L. Thus, the indicator mass balance equation at point x is:

$$\frac{v_p}{L}\frac{dc_p}{dt}(x,t) = -F_p \frac{dc_p}{dx}(x,t) - \frac{PS}{L}c_p(x,t) \qquad (1\text{-}6)$$
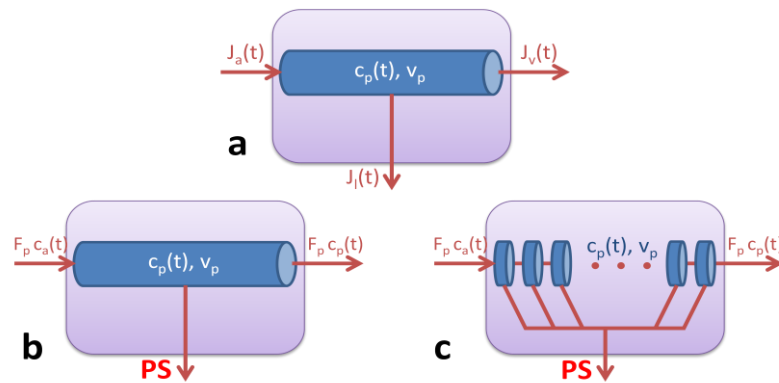
Figure 1-3 a) Schematic of an arbitrary capillary bed containing plasma with concentration $c_p(t)$, which has an influx, an outflux and a leakage outflux through the capillary wall. b) Schematic of a compartment model and, c) Schematic of a plug flow model having leakage through the wall with rate constant PS (permeability surface area product).

A two space tissue homogeneity system assumes the plasma space to be a plug flow system and the EES to be a compartment (Figure 1-4b). Thus, the mass conservation equation for EES is the same as the exchange model (equation 1-5). The total influx from the EES into the capillary $J_e = PS c_e(t)$ is distributed equally along the capillary wall. Thus, the influx from EES for a section dx of the capillary at location x is $J_e = PS c_e(t)dx/L$. Substituting these

terms in the mass conservation equation for location x in the continuum limit $dx \to 0$, we have the following governing equations (1-7 and 1-8) for the tissue homogeneity model:

$$\frac{v_p}{L}\frac{dc_p}{dt}(x,t) = -F_p\frac{dc_p}{dx}(x,t) - \frac{PS}{L}c_p(x,t) + \frac{PS}{L}c_e(t) \qquad (1\text{-}7)$$

$$v_e\frac{dc_e}{dt}(t) = PSc_p(t) - PSc_e(t) \qquad (1\text{-}8)$$

In these equations note that $c_p(t)$ is the average concentration of the capillary and $c_p(x,t)$ is the concentration in a infinitesimal segment of the capillary at location x.
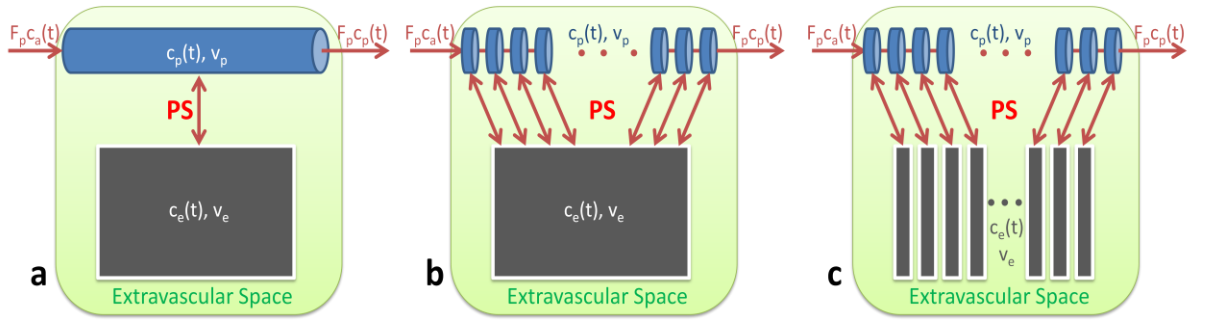
Figure 1-4 Schematic of a) the two compartment exchange model, b) the tissue homogeneity model and, c) the distributed-parameter model.

1.3.1.3 Adiabatic approximation to tissue homogeneity (AATH)

The adiabatic approximation to the tissue homogeneity model was introduced by St. Lawrence [74] and has become the most widely used model that provides a separate estimate to the F_p and PS. Similar to TH model, the AATH model assumes a plug flow for the capillary bed and a compartment model for the EES. However it assumes that the capillary wall is impermeable and the EES receives influx with clearance rate EF_p from the venous end of the capillary where E [%] is the extraction fraction (Figure 1-5a). The mass conservation equations for this system are:

$$\frac{v_p}{L}\frac{dc_p}{dt}(x,t) = -F_p\frac{dc_p}{dx}(x,t) \qquad (1\text{-}9)$$

$$v_e\frac{dc_e}{dt}(t) = EF_pc_p(L,t) - EF_pc_e(t) \qquad (1\text{-}10)$$

15

1.3.1.4 The distributed parameter model

The distributed parameter model that was introduced by Sangren and Sheppart [75] assumes the capillary bed as a plug flow and the EES as a series of infinitesimal compartments where each compartment can only exchange with its nearby locations in the capillary bed (Figure 1-4c). The EES does not allow transport of the particles parallel to the capillary from one compartment to the other and thus they cannot be transported from arterial end to the venous end in the EES. The mass conservation equation for plasma space and EES are given in equations 1-11 and 1-12 respectively:

$$\frac{v_p}{L}\frac{dc_p}{dt}(x,t) = -F_p\frac{dc_p}{dx}(x,t) - \frac{PS}{L}c_p(x,t) + \frac{PS}{L}c_e(x,t) \qquad (1\text{-}11)$$

$$\frac{v_e}{L}\frac{dc_e}{dt}(x,t) = \frac{PS}{L}c_p(x,t) - \frac{PS}{L}c_e(x,t) \qquad (1\text{-}12)$$
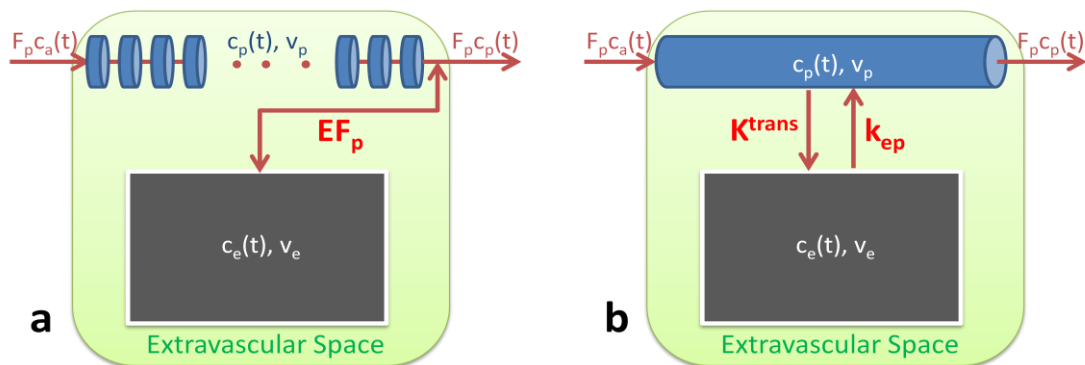
Figure 1-5 Schematic of a) adiabatic approximation to tissue homogeneity (AATH) model and, b) the Tofts-Kety model in which the contrast agent is being exchanged between the plasma space and the EES with rate constants K^{trans} and k_{ep}.

1.3.1.5 Tofts-Kety model

The Tofts-Kety [71], [72] model is a special form of the two compartment exchange model and was initially designed for tissues with negligible tracer concentration in the plasma space. Similar to the two space exchange model, Tofts-Kety model (Figure 1-5b) assumes having two spaces (Plasma and EES) that exchange the tracer with rate constants that are defined by the permeability surface area (PS) of the capillary and the plasma flow (F_p). It also assumes instantaneous mixing of the tracer in each space and assumes having one arterial inlet into and one venous outlet from the capillary while the EES only exchanges with the capillary

bed. The "Tofts-Kety" model is the weakly vascularized limit ($v_p = 0$) of exchange model. Applying this condition to equation 1-4 we have:

$$0 = F_p\left(c_a(t) - c_p(t)\right) + PS\left(c_e(t) - c_p(t)\right) \tag{1-13}$$

Thus, $c_p(t)$ in Tofts-Kety model is:

$$c_p(t) = \frac{F_p}{PS + F_p}c_a(t) + \frac{PS}{PS + F_p}c_e(t) \tag{1-14}$$

Substituting equation 1-14 in equation 1-5 we have:

$$v_e\frac{dc_e}{dt}(t) = F_p\frac{PS}{PS + F_p}\left(c_a(t) - c_e(t)\right) \tag{1-15}$$

Defining the rate constant of tracer transport from plasma space to the EES as $K^{trans} = EF_p$ ($K^{trans}\left[\frac{1}{min}\right]$) and the rate constant of tracer transport from the EES to the plasma space as $K_{ep} = \frac{EF_p}{v_e}$ ($K_{ep}\left[\frac{1}{min}\right]$), where $E = \frac{PS}{PS+F_p}$ is the extraction fraction, the Tofts-Kety model equations can be written as:

$$c_t(t) = v_e c_e(t)$$

$$v_e\frac{dc_e}{dt}(t) = K^{trans}\left(c_a(t) - c_e(t)\right) \tag{1-16}$$

Unlike the exchange models, the flow (F_p) and permeability surface area product (PS) cannot be quantified independently and the model parameters reflect a mixed effect of both parameters.

In many tissues and particularly in tumors, the assumption that the plasma space is negligible is not valid and thus the Tofts-Kety model is modified to include this term. This model which is the highly perfused limit ($F_p \rightarrow \infty$) of the exchange model is called the "extended Tofts-Kety" model. Under high flow condition the blood plasma can be considered as a single pool with equal arterial and venous concentrations, and the transport of the tracer out of the plasma space through the capillary wall is slow enough not to change the intravascular concentration ($\frac{dc_p}{dt}(t) = 0$). Substituting this condition ($\frac{dc_p}{dt}(t) = 0$) in equation 1-4 we have:

$$0 = F_p\left(c_a(t) - c_p(t)\right) + PS\left(c_e(t) - c_p(t)\right) \qquad \text{(1-17)}$$

which is the same as equation1-13 of Tofts-Kety model and thus the model equation derivation for extended Tofts-Kety model would be the same as the Tofts-Kety model. Thus the extended Tofts-Kety model equations are:

$$c_t(t) = v_p c_p(t) + v_e c_e(t)$$

$$v_e \frac{dc_e}{dt}(t) = K^{trans}\left(c_a(t) - c_e(t)\right) \qquad \text{(1-18)}$$

The Tofts-Kety model and the extended Tofts-Kety model are the most commonly used PK models in tumor characterization [76]–[80] and are recommended in consensuses [81]. Thus, in this thesis we have chosen these two models to study the tracer kinetics in tumors.

1.3.2 Vascular Input Function (VIF)

In order to solve the differential equations in any of the introduced tracer-kinetic models and calculate their model parameters, c_p or c_a, has to be known. These model equations are derived for individual capillaries while the spatial resolution in DCE imaging is such that each voxel covers an area comprised of several capillaries and extravascular space (the in-plane resolution is between 170 [μm] to 680 [μm] in our physical phantom, and is 1.8 [mm] in our prostate DCE-MRI). Consequently, solving these model equations for individual capillaries is impossible with the current imaging technology and thus, these equations are solved for every voxel and their calculated parameters represent the average value of the parameter in the voxel.

However, in order to solve these model equations at voxel level the contrast agent concentration in the intravascular space, c_p or c_a, is still required. Since there is only one measurement for signal of each voxel at each time point, the intravascular signal (vascular concentration or vascular input function) is combined with the EES signal and cannot be measured directly. Thus, it is approximated using an arterial input function [82]–[85] which is calculated outside of the tissue of interest (TOI). There are several methods to approximate the arterial input function (AIF) such as the following methods:

- **Adjacent Artery:** it is common to use the contrast agent concentration in an artery that is anatomically adjacent to the tumor [82], [86]. Such a signal is calculated using either the magnitude or phase of the MR signal in the artery [87].

- **Theoretical AIF:** this AIF usually takes the form of a bi-exponential curve [83], [88], [89] and its parameters are measured experimentally [90].

- **Population-averaged AIF:** such an AIF is usually measured experimentally through blood sampling or high temporal resolution imaging at a major artery for several subjects and then using the average of the measurement as the AIF for new subjects [84].

- **Reference-tissue based AIF:** this method attempts to estimate AIF from contrast agent concentration in a normal tissue with known physiological properties (from literature) [85].

- **Reference tissue with blood vessel:** in this method a local blood vessel (if such vessel exists) is used to calculate the physiological properties of the normal tissue (rather than using the literature values) [91].

- **Dual bolus AIF:** in this method a low dose bolus is first injected and AIF is measured in a major artery with high temporal resolution. Such an AIF has sufficient temporal resolution to capture the first pass of the bolus and the MR signal does not saturate in the artery due to high contrast agent concentration. Once the AIF is measured, the main bolus is injected and the tissue is imaged with relaxed temporal resolution [92].

In pharmacokinetic analysis of tumor tissues the concentration in the whole tumor region is considered as either extravascular (Tofts-Kety model) or a parameter is introduced (extended Tofts-Kety model) to account for the fraction that is intravascular (blood plasma volume per unit volume of tissue, v_p). In addition, in many tumors a feeding artery for the tumor in the imaging field of view does not exist which makes PK analysis difficult and inaccurate if not impossible. Some assumptions in the choice of these AIFs are:

1-   The chosen artery (for AIF measurement) is feeding the tumor

2-   No other artery is supplying blood and consequently contrast agent to the tumor

3-   There is no delay, i.e. contrast agent arrives in the artery and the tumor at the same time or an unknown (ω) is added to the system to account for the delay.

These unknown parameters produce systemic errors and make solving the system of equations complex and sensitive to noise, such that although introducing extra parameters make the model more realistic, due to increased complexity and instability of the system, the

performance of different models are similar and there is no optimal number of model parameters [93]. Thus, more sophisticated techniques are required to calculate this input function. In this thesis we propose using data-driven techniques to calculate this input function at the tissue of interest rather than approximating it outside of the tissue. We call this input function the vascular input function (VIF) as it represents the contrast agent concentration in the tumor vasculature.

1.3.3 Data-driven VIF

The main objective of this thesis is to identify and separate the contrast agent concentration in the intravascular space of the tissue of interest in order to use it as the VIF in PK modeling. However, this signal is mixed with signal of the EES and thus sophisticated signal processing techniques are required for such separation. There exist several data-driven signal separation techniques such as principal component analysis (PCA) [94], non-negative matrix factorization (NMF) [95], factor analysis of dynamic structures (FADS) [96], and independent component analysis (ICA) [97], that have been applied to dynamic contrast enhanced series to separate their underlying structures. These methods, which make no prior assumption about the physiology of the underlying structure and treat the time-series data as random variables, have been shown to segment them efficiently [97].

As mentioned in the previous section the contrast agent concentration in each MR voxel is the sum of the amount of contrast agent that is intravascular and the amount that is in EES (linear mixture of the signal in the two spaces). In addition, these two spaces (intravascular space and the EES) are anatomically separate and independent (spatially independent). These characteristics of DCE-MRI data satisfy the assumptions for spatial independent component analysis (ICA) and thus it can be used to separate the intravascular and EES signals in DCE-MRI. Our proposed VIF calculation algorithm is based on spatial independent component analysis (ICA) which assumes the underlying structure are spatially independent and are mixed linearly.

1.3.3.1 Spatial Independent component Analysis (ICA)-Based VIF

Independent component analysis (ICA) is a statistical signal processing algorithm that attempts to split a dataset into its underlying features, assuming these features are statistically independent and without assuming any knowledge of their mixing processes [98]. In this thesis we will use capital bold letter for 2-D matrices, lowercase bold letters for column

vectors, capital or lowercase letters (not bold) for scalars and, bold italic letters for functions. Having a linear mixture of the features, the spatial ICA model is expressed as:

$$\mathbf{X} = \mathbf{AS} \tag{1-19}$$

where $\mathbf{X} = [\mathbf{x}_1, \mathbf{x}_2, \dots, \mathbf{x}_N]^T$ represents the time-series dataset (DCE-MRI time-series data in our case) such that $\mathbf{x}_i$ represents the MRI image of the tissue acquired at time-point i, N is the number of time points in the DCE-MRI sequence, $\mathbf{S} = [\mathbf{s}_1, \mathbf{s}_2, \dots, \mathbf{s}_M]^T$ is a matrix containing the M structures that are known as independent components or ICs (usually $M \leq N$) and $\mathbf{A} \in \mathbb{R}^{N \times M}$ is the mixing matrix. Having the observed mixed signal $\mathbf{X}$, the spatial ICA algorithm attempts to estimate the underlying features (independent components) $\mathbf{S}$, and the mixing matrix $\mathbf{A}$. This is achieved by finding an unmixing matrix $\mathbf{W} \in \mathbb{R}^{M \times N}$ and estimating the IC matrix $\mathbf{Y} = [\mathbf{y}_1, \mathbf{y}_2, \dots, \mathbf{y}_M]^T$ (rows of $\mathbf{Y}$ are statistically independent) such that [98]:

$$\mathbf{Y} = \mathbf{WX} \tag{1-20}$$

Two independent component analysis (ICA)-based methods are proposed in this thesis to measure the contrast agent concentration in the tumor (VIF) and separate it from the extravascular signal of the tumor. Such a separation does not require an artery, accounts for variability between subjects and simplifies the PK modeling since some of the unknown parameters are eliminated. ICA has been applied to AIF measurement in brain perfusion studies [99], [100] in which, due to the presence of the blood brain barrier, there is no extravascular contrast enhancement. Measuring VIF in tumors differs from this as the objective is to separate two enhancing spaces (intravascular and extravascular) whose signals overlap due to partial volume effect and low resolution of the images. This makes the problem more challenging and has not been addressed before.

As mentioned earlier, several imaging modalities such as DCE-CT and DCE-MRI are used to image the tumor tissue and perform pharmacokinetic modeling. The focus of this thesis is on pharmacokinetic modeling of the tumor tissues using magnetic resonance imaging (MRI) which is briefly explained in the next section.

1.4 Magnetic Resonance Imaging

Certain materials, when placed in a magnetic field exhibit resonant characteristic and can absorb and reradiate electromagnetic radiation that has a specific frequency. This reradiated signal which is in the form of radio frequency signal (RF) is determined by the specific physical and chemical characteristics of the material. In magnetic resonance imaging this

reradiated RF signal also carries additional information about the location of the tissue within the human body (using the magnetic field gradients). The intensity of each voxel in an MR image is determined by the intensity of the RF signal of its corresponding tissue which is in turn determined by the three main characteristics of the tissue: nuclear density, longitudinal relaxation time (T_1), and transverse relaxation time (T_2).

The nuclei of the materials that participate in MR process must have magnetic moment which is determined by their neutron-proton composition. In medical magnetic resonance imaging Hydrogen is the principle imaging element as it has a large magnetic moment and is abundant in the tissues as part of water molecules. When these paramagnetic nuclei are placed in a strong magnetic field (B_0), their magnetic moment is aligned parallel or anti-parallel to the main magnetic field (B_0), and precess at an angular frequency (ω_0) that is proportional to B_0. Magnetic field gradients are also used to select the imaging plane and also spatially encode each voxel in this plane. An RF pulse (B_1) disrupts alignment of the moment with the main magnetic field and the return of these disrupted moments to equilibrium is governed by Bloch equations through the parameters T_1, T_2, T_2^* (which depends on the B_0 inhomogeneity), and spin density.

1.4.1 Dynamic contrast Enhanced MRI

An MRI pulse sequence is a sequence of RF pulses that are applied during MR imaging. Various characteristics of the tissue such as T_1, T_2, T_2^* or spin density could be emphasized using specific pulse sequences. If a pulse sequence is designed for the T_1 of the tissue, its image would be called a T_1-weighted image in which tissues with a shorter T_1 value appears brighter as they return to equilibrium faster than the tissues with longer T_1 value.

Dynamic contrast enhanced (DCE)-MR imaging involves an intravenous injection of a bolus of a low molecular weight contrast agent, e.g., Gadolinium (Gd)-DTPA, followed by repeated T_1-weighted imaging of the tissue of interest to track the passage of the bolus through its vasculature. The spoiled gradient recalled (SPGR) pulse sequence is used for DCE-MR imaging in this thesis whose signal intensity in a voxel without any contrast agent is expressed as:

$$SI = g\rho \, sin \, \alpha \, \frac{1 - exp(-\text{TR}/T_1)}{1 - cos \, \alpha \, exp(-\text{TR}/T_1)} \, exp(-\text{TE}/T_2^*) \qquad (1\text{-}21)$$

where SI is the measured signal intensity at the voxel, g is the scanner gain, ρ is the proton density, α is the flip angle, TE is the echo time, TR is the repetition time, T_2^* is the transverse relaxation and T_1 is the longitudinal relaxation of the tissue. The spoiled SPGR is used for DCE-MR imaging as it has a short TR and thus can image the tissue with high temporal resolution. As the contrast agent arrives in the tissue, it changes the magnetic characteristics of the tissue, i.e. the transverse and longitudinal relaxation times, and hence changes its signal intensity. The relationships between relaxation times before and after arrival of the contrast agent, c [mMol], are [101]:

$$\frac{1}{T_1} = \frac{1}{T_{10}} + R_1 c, \qquad \frac{1}{T_2^*} = \frac{1}{T_{20}^*} + R_2 c \qquad (1\text{-}22)$$

where T_{10} and T_{20}^* are the longitudinal and transverse relaxations respectively with no contrast agent. T_1 and T_2^* are the longitudinal and transverse relaxations respectively after the contrast agent enters the voxel and R_1 $[\frac{1}{mMol \cdot s}]$ and R_2 $[\frac{1}{mMol \cdot s}]$ are the longitudinal and transverse relaxivities of the contrast agent.

This thesis proposed data-driven algorithms for VIF calculation in DCE-MRI in tumors to be used in PK analysis instead of an AIF. The proposed algorithms are evaluated using phantoms and in-vivo studies as explained in the next section.

1.5 Evaluation of VIF calculation algorithms

Two ICA-based VIF calculation algorithms are developed in this thesis: i) Magnitude ICA (Mag-ICA) in chapter 3, and ii) Adaptive complex ICA (AC-ICA) in chapter 4. The accuracy of each algorithm in identifying and separating the intravascular contrast agent concentration is evaluated in there corresponding chapters using numerical and physical phantoms as well as in-vivo tumor models.

The Mag-ICA algorithm (chapter 3) is first introduced and its performance is evaluated using numerical and physical tissue-mimicking phantom where the actual intravascular signal is known ("ground truth" is available). It is then applied to in-vivo VX2 tumors in rabbit thigh muscles and its accuracy is evaluated spatially using contrast enhanced ultrasound (CE-US) images of the tumor. Ultrasound contrast agent, i.e. microbubbles, stay intravascular and thus their images represent the tumor vasculature (CE-US will be described in more detail in section 2.3.3). The accuracy of the separated intravascular signal of VX2 tumors in temporal

domain is also evaluated using contrast enhancement of a blood vessel feeding the tumor. These studies demonstrate the feasibility of VIF calculation using Mag-ICA and highlight the major issues with the algorithm that need to be resolved.

The AC-ICA algorithm is the improved version of the Mag-ICA and is developed to address its main issues, which are using the magnitude of the MRI data and also using a fixed non-linearity function in its ICA algorithm, and is presented in chapter 4. Similar to the Mag-ICA algorithm, the performance of the AC-ICA algorithm is evaluated using the numerical and physical phantoms and is compared to the performance of the Mag-ICA algorithm. A normalization step for the calculated VIF is also introduced in chapter 5 which normalized the curves (AIF and VIF) with respect to their area under the curve. The impact of this step on the PK analysis is evaluated using the numerical phantom and prostate DCE-MRI.

DCE-MRI datasets of prostate cancer patients are used in this thesis (explained in the next section) to assess the performance of the proposed data-driven VIFs and compare their PK parameters to the parameters that are achieved using current methods which use an AIF in their PK analysis. Prostate cancer is selected as there is a large artery in its DCE-MR imaging field of view (femoral artery) which can be used to measure an AIF and thus enables comparison between our data-driven estimate and an established "gold" standard. Moreover, there have been several studies on calculating the PK parameters of prostate tissue using currently available techniques in the literature which can be used to assess the performance of our method. Thus; in the remainder of this chapter, a brief review of prostate anatomy, prostate cancer and prostate cancer diagnosis methods is provided.

1.5.1 Prostate Anatomy

The prostate gland is a small, muscular, rounded organ with a diameter of about 4 cm that is located in the pelvis and as shown in Figure 1-6a is surrounded posteriorly by the rectum and superiorly by the bladder. The prostate gland encircles the proximal portion of the urethra and is comprised of branching glands with ducts that are lined by secretory epithelial and basal cells [102]. The majority of the gland is comprised of the secretory epithelial cells which produce prostate specific antigen (PSA). The basal cells contain the stem cell population for the epithelial prostate cells.

The prostate gland consists of three zones (Figure 1-6b): the peripheral zone, the central zone and the transitional zone. The peripheral zone, where more than 70% of prostate cancers

originate, is located along the posterior edge and apex of the prostate gland [103]. The transitional and central zones, which are often referred to as the central gland, are located in the center-to-superior aspect of the prostate and surround the urethra [104] .

The blood supply of the prostate gland is via branches of the inferior vesical and middle rectal arteries and it drains through the prostatic venous plexus which is between the prostate capsule and the fibrous sheath [105]. The lymph vessels from the prostate drain into the internal iliac nodes, and the nerve supply of the prostate is from the inferior hypogastric plexuses [105].
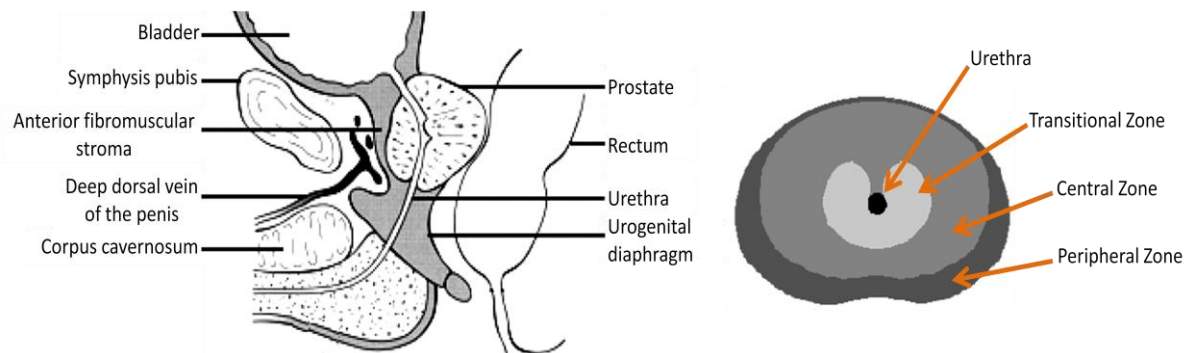
Figure 1-6 a) a) The anatomy of the prostate [106]: the prostate gland which is about 3-5 [cm] in diameter and is located anterior to the rectum and inferior to the bladder with urethra passing through it. Image reprinted with permission from Elsevier: Coakley et al., "Radiologic Radiologic anatomy of the prostate gland: A clinical approach", *Radiologic Clinics of North America* 38(1): 15-30, © (2000). b) Zonal anatomy of prostate: the prostate is composed of three zones: transitional, central and peripheral zones. The peripheral zone is located along the posterior edge and apex of the prostate gland and the transitional and central zones are located in the center-to-superior aspect of the prostate and surround the urethra. Image inspired by Snell [105].

1.5.2 Prostate cancer

Prostate cancer, with a worldwide incidence rate of 25.3 per 100,000, is the second most common type of cancer in men after lung cancer [107]. The mortality rate of prostate cancer is 8.1 per 100,000 and mainly affects men at older ages [108]. Some of the risk factors for prostate cancer are age (older men have higher risk) [109], genetic factors (higher risk of prostate cancer was shown in men with affected relatives) [110], environmental risk factors such as smoking, alcohol consumption, cadmium exposure, ionizing radiation, etc. [111].

Prostate cancer is a glandular malignant neoplasia of secretory or luminal cells. Prostate cancer has different types that are all considered to originate from prostate acini. The variability in prostate cancers can be explained by the number of different intermediate cells

that can evolve into malignant cells and are observed between the prostate acini and the final secretory cells [107].

1.5.3 Screening and Diagnosis

The most common symptom of abnormality in the prostate is obstruction in bladder outlet which is more often a sign of BPH (benign prostatic hyperplasia) than prostate cancer. Other symptoms of prostate cancer are perineal pain, impotence and hematuria. If any of these symptoms are present, the patient is examined for prostate cancer by one or a combination of the following methods [112]:

Digital Rectal Examination (DRE): The doctor puts a finger into the rectum to examine the prostate gland to feel tenderness or problems such as enlargement, hardness or growths. This method has poor sensitivity and specificity where only 30% of the cancers detected by DRE are organ confined and potentially curable [112].

Prostate Specific Antigen (PSA) test: PSA is a glycoprotein enzyme that is secreted by the epithelial cells of the prostate gland and is elevated in presence of prostate cancer and other abnormalities. PSA has a high false positive rate with only 30% of the patients with elevated PSA being confirmed for prostate cancer after biopsy [113].

Transrectal Ultrasound (TRUS): An ultrasound technique that is used to view the prostate and its surrounding tissues in which the prostate cancer appears as a hypoechoic nodule. However small tumors are usually not visible where only 10-15% of the cancers detected by TRUS are not palpable and 75% of these patients will have high PSA levels [114].

Multi-parametric MR imaging: The anatomical and functional information that MRI provides can be used for prostate cancer detection and diagnosis. A combination of anatomical T_2-weighted MR imaging and several functional imaging techniques such as dynamic contrast enhanced (DCE)-MRI, diffusion weighted (DW)-MRI and MR spectroscopic (MRS) imaging are usually used. Although these multi-parametric MR imaging techniques contribute to prostate cancer diagnosis, their results in detection, localization, and staging of the cancer vary significantly between studies and need to be improved [115]

Prostate Biopsy: Prostate cancer diagnosis requires histological confirmation which is usually done through TRUS-guided biopsy in which the samples are obtained systematically

from different areas of the prostate (three samples from each side of the peripheral zone and sometimes two cores from the transition zone are also obtained) [116].

1.5.3.1 Grading Prostate Cancer

Solid tumors are considered to be formed in a multi-step process where successive genetic events occur to transform a cell from healthy to malignant. The genetic and epigenetic phenomena that occur in prostate cancer are not well understood and thus all prostatic epithelial dysplasia and atypia are considered "prostatic intraepithelial neoplasia (PIN)". There are three different grades of PIN (low, moderate and severe), where moderate and severe PIN lesions are seen adjacent to prostate adenocarcinonas and high grade PIN lesions are often seen in multi-focal cancers. Autopsy studies suggest that PIN precedes prostate cancer development by at least 10 years [116].

Over 95% of prostate cancers are adenocarcinomas that arise from prostatic epithelial cells. Many studies have suggested the importance of the degree of histological differentiation of prostate adenocarcinona. The most widely internationally accepted grading system for prostate adenocarcinoma differentiation is the Gleason score (Figure 1-7), which is based on progressive loss of the gland pattern and increased peritumoral stroma invasion [117].
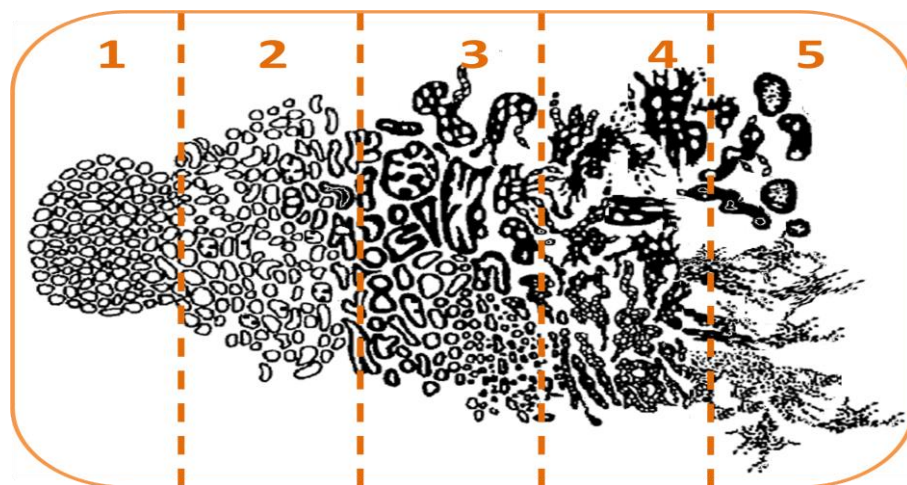
Figure 1-7 Drawing of histological patterns of prostate adenocarcinoma showing the degree of glandular differentiation (image adapted from Gleason [118]). The 5 different pattern of Gleason scoring system as shown in this figure are 1- single, well formed, closely packed, separate, round glands that resemble normal prostate tissue, 2- single, separate, less uniform, large glands separated with stroma up to one gland diameter, 3- glands are still separate and recognizable but are irregular with variable size and have darker cells (in high magnification some of these cells have left the gland and are beginning to invade surrounding tissue), 4- there are few recognizable glands (fused papillary glands with solid patterns) and a large number of cells are invading surrounding tissue, 5- few or no recognizable glands, masses with comedo pattern and there are often sheets of tumor cells throughout the surrounding tissue [119].

In the Gleason scoring system the prostate tumor is scored in two levels to account for its heterogeneity where the primary and secondary patterns of the tumor are each given a score of 1 to 5 (shown in Figure 1-7) and the Gleason grade of the tumor is the resultant two-digit score for example 3+4=7. Despite the limitations of this grading system it has shown excellent reproducibility and reliability [107].

1.6 Outline of the thesis

The main goal of this thesis is to develop a data-driven technique using independent component analysis, to identify and separate the intravascular component in DCE-MR images of tumors. The intravascular component is then used to generate a local vascular input function (VIF) for pharmacokinetic analysis of the tumor. Such a VIF that is measured locally at the tissue of interest has the potential to provide more accurate PK parameters compared to the conventional methods that use an arterial input function (AIF) in their analysis. In addition it could be used in cases where measuring an AIF is not feasible or is difficult such as PK analysis in small animals. The method could also potentially be used to relax the high temporal resolution acquisition (needed for accurate AIF measurement) and increase the spatial resolution of the acquired images.

1.6.1 The specific aims of this thesis

1-   Studying the feasibility of using independent component analysis in indentifying and separating the VIF (considering the VIF is mixed with the signal from extravascular space due to partial volume effect and the low temporal resolution of the DCE-MRI data). This aim is assessed using numerical and physical phantom studies as well as using co-registered DCE-MRI and contrast enhanced ultrasound images of VX2 tumor in rabbits.

2-   Developing an ICA-based VIF separation algorithm using the complex-valued MRI signal and an adaptive formulation to model the wide range of VIF signals which differ from one study to another due to heterogeneity in tumor structure and the site and type of the tumor. The algorithm is developed (chapter 4) and its performance was assessed using numerical and physical tissue-mimicking phantoms.

3-   Assessing the impact that using the proposed local VIF has on the pharmacokinetic parameters using a cohort of 28 prostate cancer DCE-MRI datasets, compared to conventional methods that use an AIF in their analysis.

1.6.2 Structure of the thesis

The remaining content of this thesis is structured as follows:

- The second chapter provides detail for: the design of the numerical phantom and the method of generating corresponding DCE-MRI data; the physical tissue-mimicking DCE-MRI phantom that is used in the analysis; the VX2 tumor model in rabbits (imaged with both DCE-MRI and CE-US); and the DCE-MRI data of the prostate cancer patients that are used in evaluating the methods and assessing their performance.

- Chapter three presents the classical ICA-based VIF calculation algorithm that is used to assess the feasibility of using ICA for VIF calculation (Mag-ICA). The results of applying this algorithm, which uses a fixed non-linearity function in its ICA implementation and is applied to the magnitude of the MRI data, to the numerical and physical phantoms as well as the VX2 tumor model are also presented.

- Chapter four provides the derivation of the proposed adaptive complex ICA (AC-ICA) algorithm for VIF calculation. It also presents the results of applying the developed AC-ICA algorithm, which uses an adaptive non-linearity function in its ICA implementation and is applied to the complex-valued MRI data, to the numerical and physical phantoms and assesses its performance.

- Chapter five explains the steps that have to be taken to convert the separated intravascular signal into contrast agent concentration and the normalization step that is required for PK analysis. It also applies the developed AC-ICA algorithm to DCE-MRI data of a cohort of 27 prostate cancer patients (28 datasets with one patient being imaged twice) and compares their pharmacokinetic parameters to those of conventional PK analysis methods using femoral artery as their AIF.

- In chapter six the conclusions of this thesis as well as the remaining challenges that have to be addressed and the future work that have to be performed to fully understand and assess the performance of the proposed local VIF in PK analysis are explained.

Chapter 2

DCE-MRI Data Acquisition

The previous chapter provided the background information and performed the literature review on cancer biomarkers and how tumor angiogenesis could be used to provide such biomarkers. It discussed extracting quantitative information about tumors through medical imaging combined with tracer-kinetic modeling which required an AIF. It also explained the need for measuring contrast agent concentration in the vasculature and calculating a local VIF to be used in tracer-kinetic modeling of the tissue rather than using an AIF. The DCE-MRI data that are used in this thesis are separately presented in this chapter to avoid repetition as each dataset is used in more than one chapter (e.g. the numerical phantom is used in chapters 3, 4 and 5). This chapter provides details of the numerical tissue-mimicking phantom, the physical tissue-mimicking phantom, the rabbit VX2 tumor model and the DCE-MRI and contrast enhanced ultrasound imaging protocols used, and the DCE-MRI images of prostate cancer that are used in the thesis to assess the performance of the two VIF calculation algorithms.

2.1 Numerical phantom

A simulation study was conducted to simulate DCE-MR images of a leaky phantom using a combination of finite element analysis (FEA) and classical description of MRI physics by means of Bloch equations. The numerical phantom was designed such that it simulated our physical tissue-mimicking phantom (explained in section 2.2). This numerical phantom is used in assessing the feasibility of separating the intravascular signal using Mag-ICA algorithm (chapter 3) and in assessing the performance of the proposed adaptive complex ICA (AC-ICA) algorithm in VIF calculation (chapter 4). It is also used in investigating the effects of normalizing VIF with respect to its area under the curve (AUC) in chapter 5.

2.1.1 Contrast agent concentration modeling

The Comsol Multiphysics (Comsol Inc., Burlington, USA) finite element analysis (FEA) software was used to construct the simulated phantom that is shown in Figure 2-1. This phantom was comprised of a grid of 10×10 leaky tubes that run in parallel through a chamber of agar gel (0.5% agar gel). The tubes had an internal diameter of 200 [μm], wall thickness of 30 [μm], and center to center spacing of 300 [μm]. To model our physical phantoms some of the tubes were removed to simulate the blocked or damaged tubes as shown in Figure 2-1a and c. The study simulated the passage of a bolus of contrast agent through the tubes and its leakage from the tubes into the agar gel over time. The spacing and diameter of the tubes were selected such that the vascular fraction of the phantom was 3.8% so that it simulated the vascular volume fraction of tumor tissue [120].

| (a) | (b) | (c) |
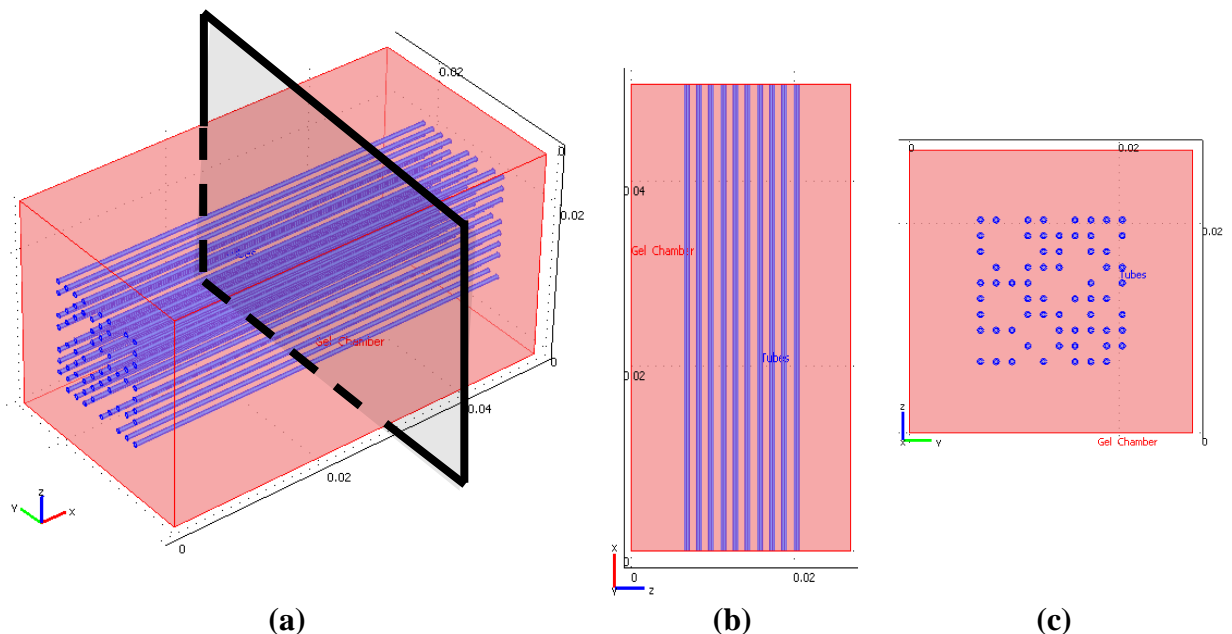
Figure 2-1 a) 3D view of the numerical phantom showing the imaging plane that is located halfway through the phantom in x-direction and lies in the yz-plane b) the xz-plane showing the tubes are parallel in the gel. c) The view of the phantom from zy-plane that lies in the MR imaging plane showing the arrangement of the tubes as well as the blocked tubes.

The contrast agent distribution of the phantom was simulated for an imaging plane half way through the length of the chamber, transverse to the phantom as depicted in Figure 2-1a. A cross-section showing the orientation of the tubes in the imaging plane is shown in Figure 2-1c. A 3D simulation was first performed to model the contrast agent concentration inside the tubes at the imaging plane. The contrast agent is injected to the tubes at the edge tubes located on the $x = 0$ plane. The flow rate and contrast concentration of the simulated bolus

31

was selected such that the concentration-time curve of the tubes in the imaging plane was the same as our physical phantom studies.

Once the contrast agent concentration of the tubes at the imaging plane was determined, a 2D numerical study was used to simulate the leakage of the contrast agent through the tubes at the imaging plane. As the contrast agent arrived in the transverse plane it diffused into the surrounding gel. A range of different diffusion coefficients were assigned to the gel, the tubes and tube walls to account for variability of diffusion throughout the gel and generate a heterogeneous leakage space. As such, the imaging plane was split into 2555 subdomains as shown in Figure 2-2a with different diffusion coefficients. The subdomains were fine near the tubes at there is more dynamic changes in these areas and were courser far from the tubes. The reason for using different subdomain sizes was to enable accurate calculation of the contrast agent distribution close to the tubes without having memory problem in performing the FEA. A single subdomain was used for inside of each tube as they were assigned the highest diffusion value and the contrast agent distributed in them very quickly. Once the phantom was built, the standard triangular meshing system of Comsol Multiphysics software was used to generate a mesh on the phantom to identify the elements in FEA.

It was assumed that the diffusion coefficient of the gel had a uniform distribution with mean value of 2.08×10^{-4} [$\frac{mm^2}{s}$] [121] and standard deviation of 1×10^{-5} [$\frac{mm^2}{s}$]. The subdomains corresponding to the inside of the tubes were given the highest diffusion coefficients (1×10^{-3} [$\frac{mm^2}{s}$]), which is close to the self-diffusion coefficient of water [122] as they were simulating the water flowing through the tubes, and the subdomains corresponding to the walls of the tubes were assigned the lowest diffusion coefficients ($2 \times 10^{-5} \pm 10^{-6}$ [$\frac{mm^2}{s}$]). The subdomains around one of the tubes showing the inner circle of the tube, the tube wall and the surrounding gel subdomains are also illustrated in Figure 2-2a. The relationship between this model (which was built using diffusion coefficients) and the pharmacokinetic parameters of the Tofts-Kety model is given in appendix I.

The simulation was performed for 6.48 [min] with a temporal resolution of 3.3 [s] which was chosen according to our physical phantom study. The contrast agent distribution at time 2.5 [min] after injection of the contrast agent is shown in Figure 2-2b which shows the heterogeneous distribution of contrast agent in the phantom.
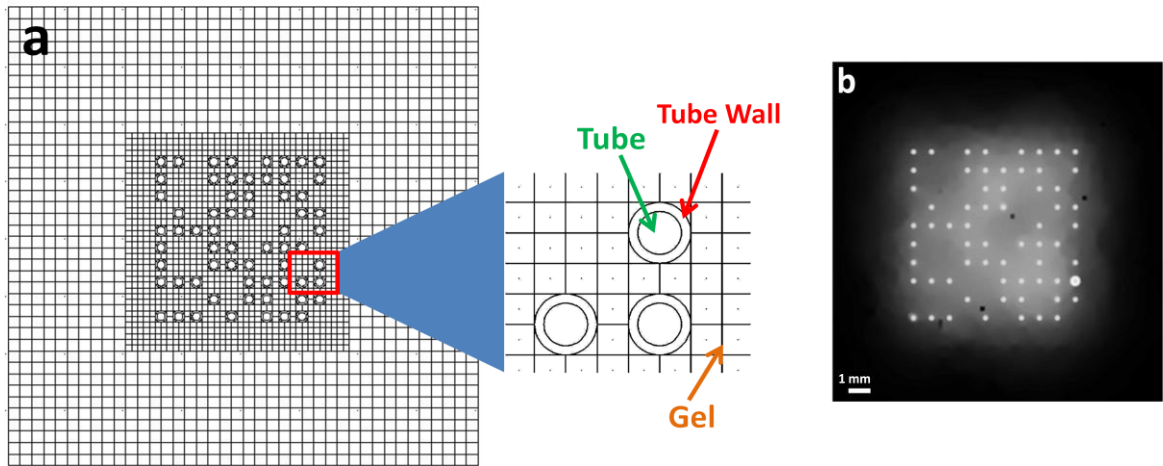
Figure 2-2 a) The FE subdomains of the phantom in the imaging plane. There are 2555 subdomains in this plane with different diffusion coefficients. As shown in the enlarged region of the phantom, the tubes, their walls and their surrounding gel areas are separated and proper diffusion coefficients are assigned to the subdomains of each region. b) The contrast agent distribution in the imaging plane, at t=2.5 [min] after injection of the contrast agent. This figure shows the heterogeneous distribution of the contrast agent in the phantom.

2.1.2 Generating DCE-MRI data (Bloch equation)

It was assumed that water was flowing through the tubes and a bolus of gadolinium (Gd)-DTPA contrast agent was added to the flowing water. The geometry and contrast concentration of the tubes and the agar gel that were calculated in the FEA were fed to the MRI simulation software, and 120 frames were simulated to generate the DCE-MRI dataset. This section provides an overview of the 2D MRI simulator that solved the Bloch equation at each voxel. It was developed based on the SIMRI project which was generated to simulate MR images [123]. The developed simulator started with assigning proton density ρ, longitudinal relaxation T_1 and transverse relaxation T_2 to each voxel; these parameters are necessary for computing local spin magnetization. It was assumed that each voxel was comprised of 2 isochromates [124] corresponding to the tube and gel compartments.

The proton density of each isochromate at each voxel was calculated by taking the percentage of the voxel that belonged to the tubes/gel, which was available from the FEA step, multiplied by the proton density of water/gel. The pre-contrast T_1 relaxations (T_{10}) of water and 0.5% agar gel were set to 3000 [ms] and 2100 [ms] respectively. The pre-contrast T_2 relaxations (T_{20}) of the water and gel were set to 250 [ms] and 65 [ms] respectively [123], [125]. The post-contrast T_1 and T_2 values were calculated using the following equations [101]:

33

$$\frac{1}{T_1} = \frac{1}{T_{10}} + R_1 c \qquad \& \qquad \frac{1}{T_2} = \frac{1}{T_{20}} + R_2 c$$

where R_1=4.5 $[\frac{1}{mMol \cdot s}]$ and R_2=5.5 $[\frac{1}{mMol \cdot s}]$ are the longitudinal and transverse relaxivities of contrast agent respectively, and c [mMol] is the contrast agent concentration in water or gel that was calculated in the FEA step for each voxel at each frame of the dynamic sequence. The use of 2 isochromates in each voxel facilitated a realistic simulation of the cases where there were two different materials in the voxel. It also allowed for simulation of intra-voxel de-phasing of spins in the voxel due to magnetic field inhomogeneity.

The dynamic contrast-enhanced MRI simulation was performed assuming a B_0 magnetic field of 1.5 [T] with 1 [ppm] inhomogeneity using a single coil RF pulse. 2D spoiled gradient recalled (SPGR) sequence of 120 frames (temporal resolution = 3.3 [s]) were simulated. Other imaging parameters of the MRI simulation were: TR = 12.5 [ms], TE = 2.9 [ms], FA (flip angle) = 20°, Band Width (BW) = 15.63 [kHz], Nx/Ny = 128/128, Field-of-View (FOV) = 19.2 [mm], Slice Thickness = 5 [mm]. Gaussian noise was added to the k-space data and its standard deviation was selected such that an SNR of 20 was achieved in the image space.

The simulated DCE-MRI data was reconstructed at four different resolutions. The high resolution dataset had in-plane resolution of 150 [μm]. In other datasets the high frequency elements in k-space were removed and low resolution datasets with in-plane resolutions of 300 [μm], 600 [μm] and 800 [μm] were constructed. A sample frame of each dataset at time=2.5 [min] after injection of the contrast agent is shown in Figure 2-3. These simulated DCE-MRI datasets were used to assess the performance of the Mag-ICA (chapter 3) and AC-ICA (chapter 4) VIF calculation algorithms. The use of DCE-MRI data with different resolutions was also used to assess the robustness of the two algorithms in separating the intravascular signal, particularly in low resolutions that are commonly encountered in clinic.
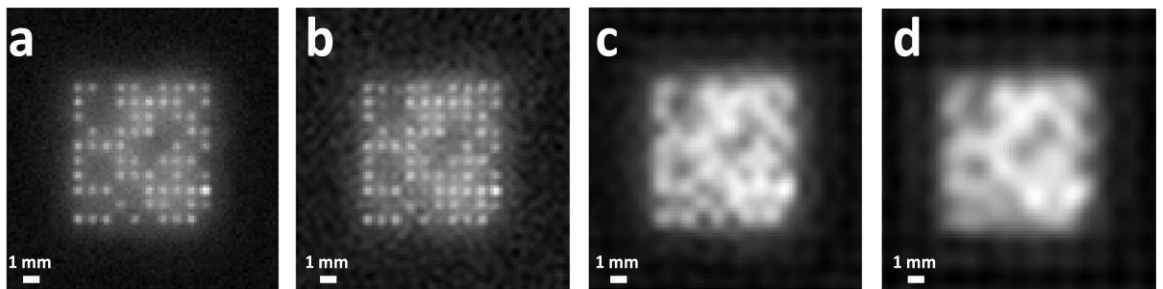
Figure 2-3 A sample frame of the simulated dataset (at t = 2.5 [min] after contrast agent injection) for in-plane resolution of a) 150 [μm], b) 300 [μm] c) 600 [μm], and d) 800 [μm].

Since ICA is a stochastic process, it is important to assess the reproducibility of the intravascular time-intensity curve calculation process. Therefore, to assess the reproducibility of the AC-ICA and Mag-ICA results, the DCE-MRI dataset at each resolution was generated 10 times. Although these datasets were generated with the same imaging, geometry, and physical parameters, they differed in distribution of B_0 inhomogeneity that was added to the main magnetic field as a random Gaussian signal (1 [ppm] inhomogeneity) and the Gaussian noise (SNR=20) that was added to the k-space data. The Gaussian noise was added to the simulated k-space data where standard deviation of noise was selected such that the SNR in image space was 20 (SNR=20).

2.2 Physical Phantom

We used a physical phantom[1] that was constructed to mimic the behavior of contrast agent in tumor microvasculature [126]. The phantom served as a platform to evaluate the two ICA-based VIF calculation algorithms. The phantom design was such that the true intravascular signal (VIF) was available to assess the performance of the two ICA-based algorithms. This physical phantom was used in assessing the feasibility of separating the intravascular signal using Mag-ICA algorithm (chapter 3) and in assessing the performance of the AC-ICA algorithm in VIF calculation (chapter 4).

2.2.1 Phantom design

The MR compatible phantom (Figure 2-4a) which was similar to the simulation phantom, was comprised of a grid of 10x10 dialysis tubing (Diapes PES-150, Baxter) embedded into a chamber of agar gel (0.5 wt%, Sigma-Aldrich Canada Ltd., Canada) [126]. The contrast agent could flow through the dialysis tubing that had inner diameter of 200 [μm], wall thickness of 30 [μm] and were aligned parallel to each other in a square grid with center to center spacing of 300 [μm] over an approximately 5 [cm] distance [126]. The pore size of the dialysis tubing ranged from 89 [nm] to 972 [nm] which enabled the low-molecular weight Gd-DTPA contrast agent to diffuse out of the tubes and into the surrounding gel. In this configuration, the dialysis tubing represented the leaky microvascular compartment of tissue, and the agar gel represented the extravascular component.

---

[1] The physical phantom was built and its DCE-MR images were acquired by Ian Pang from Dr. Rajiv Chopra's Laboratory.
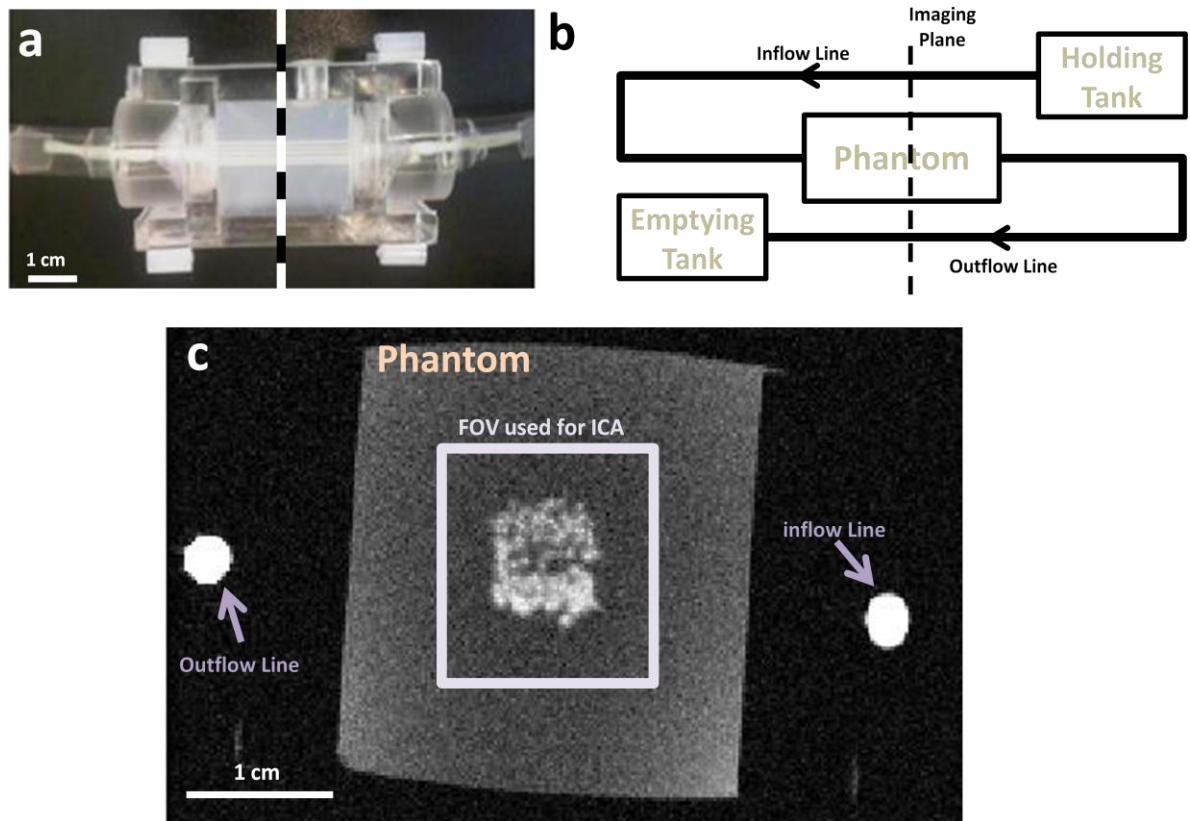
Figure 2-4. a) Photograph of the physical phantom used in this study. Imaging was performed across the dashed line in the middle of the phantom, in a plane perpendicular to view that is shown in the photo. b) Schematic of the tissue-mimicking phantom set up. Water was flowing at a constant rate (0.047 $\left[\frac{ml}{s}\right]$) from the holding tank to the emptying tank. The contrast agent was injected into the inflow line and the phantom was imaged at the imaging plane that included the phantom as well as the inflow and outflow lines as shown in the figure. c) A sample MR image of the full imaging field of view (FOV) at time = 1.8 [min] after injection of the contrast agent that shows the inflow line, the outflow line, the entire phantom at imaging plane and the field of view around the tubes that was used in ICA analysis

A fixed-height reservoir of water was used to produce a constant flow through the phantom at a rate of 0.047 $\left[\frac{ml}{s}\right]$ at an input pressure of ~35.6 [mmHg] which achieved a flow velocity within physiological range of arterioles [127]. An automatic syringe pump (Harvard Pump 11 Plus, Harvard Apparatus, Holliston, USA) was used to inject a bolus of gadolinium (Gd)-DTPA contrast agent into the flow line in order to achieve a constant injection rate and volume. Once the bolus reached the chamber that contained the gel, it was capable of leaking from the tubes into the gel. MR images were obtained transverse to the tubes during the passage of the respective contrast agents. The inflow effects in the phantom are negligible as explained in detail in appendix II. In order to measure the contrast agent concentration inside the tubes, the inflow line of the flow into and outflow line of the flow out of the chamber were oriented such that they passed through the imaging plane as shown in Figure 2-4b and

Figure 2-4c. The MR signal of the inflow line was used as the actual tubes' signal (with a delay of 6.6 [s]) and was used to validate the calculated intravascular time-intensity curve.

2.2.2 DCE-MR Imaging

DCE-MR imaging was performed at a transverse plane in the middle of the phantom as shown in Figure 2-4a. Dynamic contrast enhanced MR imaging was performed using a 2D fast spoiled gradient recalled (fSPGR) sequence with the following imaging parameters: TR = 12.5 [ms], TE = 2.9 [ms], Flip Angle = 20°, BW= 15.63 [kHz], Nx/Ny/NEX = 256/256/1, FOV = 45 [mm], Slice Thickness = 5 [mm]. A total of 120 images were acquired over about 6.48 [min] with a temporal resolution of 3.3 [s] and no delay between acquisitions. A sample frame of the DCE-MRI sequence (at time=1.8 [min]) showing the tubes and phantom (full field of view), the ROI that was used for ICA analysis as well as the inflow and outflow lines are shown in Figure 2-4c.

As in the simulation study, the data was reconstructed in different resolutions to assess the performance and robustness of the Mag-ICA and the AC-ICA algorithms and to compare the VIF curve estimated using ICA-based algorithms with the actual time-intensity curve of the tubes (measured at the inflow line). The image reconstruction was performed at 5 different in-plane resolutions of 170 [μm], 225 [μm], 340 [μm], 450 [μm] and 680 [μm]. The low resolution datasets were generated by removing (zero-padding) the high frequency terms of the acquired high resolution DCE-MRI data in k-space. A sample frame of each dataset at time=1.8 [min] after injection of the contrast agent, is shown in Fig. 2-5a to Fig. 2-5e. In order to assess the reproducibility of the intravascular time-intensity curve calculation processes, for both AC-ICA and Mag-ICA algorithms, two phantoms with identical specifications were built and DCE-MR imaging with the same imaging parameters was performed on both phantoms.
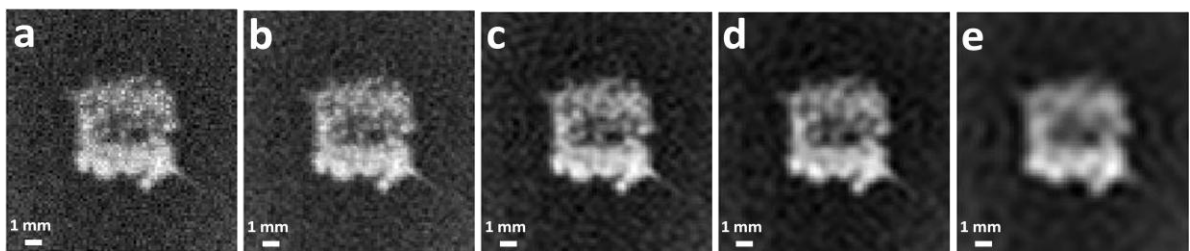
Fig. 2-5 A sample frame of the DCE-MRI dataset of the physical phantom (at time = 1.8 [min] after injection of the contrast agent) for in-plane resolution of a) 170 [μm], b) 225 [μm], c) 340 [μm], d) 450 [μm], and e) 680 [μm].

2.3 *In vivo* VX2 tumor

In addition to the numerical and physical phantom studies, we performed an *in vivo* study using VX2 tumors in thigh muscle of rabbits[2]. These *in vivo* tumors were used in assessing the feasibility of separating the intravascular signal using ICA (chapter 3).

2.3.1 VX2 tumor in Rabbits

Approval was obtained from local Animal Care Committee at Sunnybrook Health Sciences Centre for this study, which was performed in four New Zealand white rabbits (3-4.5 [kg]) (Charles River Laboratories, Wilmington, MA) [128]. Tumors were initiated in both thighs of the rabbits through intramuscular implantation of VX2 cells as explained in [129]. Fresh tumor was initially harvested within 30 minutes after sacrificing a live carrier and was cryopreserved for subsequent multiple transplantations. For each transplantation, the cryopreserved tumor was brought to room temperature and then grounded and homogenized. Viability of cells was estimated by Trypan Blue exclusion and the number of cells in suspension was counted under a microscope. The tumors were implanted into each animal by using approximately 0.15mL of tumor suspension (4 x 10^6 cells) injected slowly via an 18-gauge needle into musculature of the rabbit thigh. Imaging was performed approximately 13 days after implantation to enable tumors to grow to a desired volume of 1.5 [cm^3]. Rabbits were anaesthetized with an intramuscular injection of ketamine (50 $\left[\frac{mg}{kg}\right]$) and xylazine (10 $\left[\frac{mg}{kg}\right]$). Anesthesia was maintained during imaging using inhalation of isoflurane (3-4%). The animals were sacrificed after imaging by intracardiac injection (Euthanyl^{TM}). Imaging was performed with the rabbits in the lateral decubitus position, using an apparatus developed for co-registered ultrasound (US) and MR imaging, described previously [128], [130], [131].

Briefly, US imaging was first performed to obtain 20 axial images (2 [mm] apart). Out of the twenty imaging planes, two suitable imaging planes were selected where a combination of tissues (tumor tissue, muscle, fat and vessels) were visible. After US imaging, the rabbits were transferred in the co-registration apparatus to a 1.5 [T] MRI (Signa, GE Healthcare, USA) and MR images were obtained in the same orientation and locations as the US data. The selection of the two imaging planes was enforced by the co-registration system

---

[2] The implantation of VX2 tumors in thigh muscle of rabbits and their DCE-MRI and CE-US imaging were performed by Chaitanya Chandrana, John M. Hudson and Peter Bevan at Dr. Rajiv Chopra's Laboratory.

developed in [128]. Since the ultrasound and MR acquisitions were not performed simultaneously, the setup had two fiducials that were used to co-register the contrast enhanced ultrasound (explained in section 2.3.3) and DCE-MR images of each tumor.

To synchronize contrast injections for different modalities the following steps were taken:

1-   Contrast agents were injected 15 seconds after the start of data collection.

2-   The contrast injection volumes, flush rate and flush volume were kept the same (using injection pumps) to ensure that the rabbit's physiological reactions due to external injections were consistent.

Additional parameters used for MR and US contrast imaging are detailed in [128]. The thigh muscles of four rabbits with implanted tumors were imaged with both MR and US, and contrast kinetics were studied in two imaging planes.

2.3.2 DCE-MR imaging

The *in vivo* DCE-MR imaging was performed at 1.5 [T] MR system (Signa, GE Healthcare, USA) using a 5-inch surface RF receive coil. A total of 150 images were acquired using an axial 2D FSPGR sequence with TR = 5.3 [ms], TE = 1.5 [ms], Flip Angle = 30°, Nx/Ny/NE = 128/128/4, BW = 15.63 [kHz], slice thickness = 4 [mm], FOV = 15 [cm]. The DCE-MRI datasets had in-plane-resolution of 1100 [µm] and temporal resolution of 2.7 [s] and Gd DTPA-BMA (Omniscan, GE Healthcare, USA) was used as the contrast agent. A sample MR image of the full field of view that was imaged, showing the rabbit thigh and the tumor that was implanted as well as the water bath that contained the fiducial markers (used for US-MR co-registration) is demonstrated in Figure 2-6a. A large artery was also identified in this dataset whose signal enhancement was used as the actual AIF of the animal and was used to evaluate the performance of the Mag-ICA method (such an artery was not present in other datasets). The reduced field of view of MR image showing the tumor region is provided in Figure 2-6b.
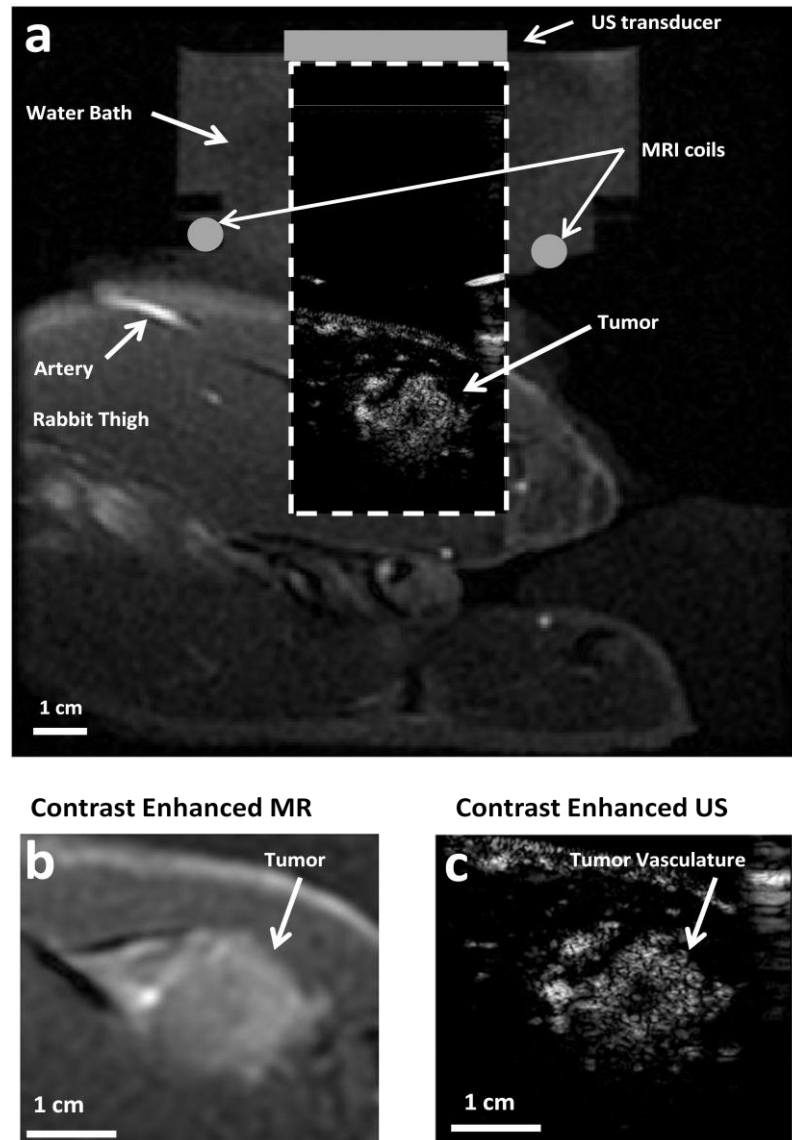
Figure 2-6 The DCE-MRI and CE-US data that was acquired *in vivo*. a) This image shows the full field of view of axial MR image of the thigh of the tumor-bearing rabbit with the co-registered ultrasound image superimposed (inside the dashed line). This image also shows the artery that was identified in the imaging plane. The time-intensity curve of this artery was used as the actual AIF in our analysis to evaluate separation results of Mag-ICA algorithm. Moreover, some of the imaging specifications such as the location of the 2 RF coils that were used for MR imaging and the location of US transducer as well as the water bath are shown in this figure. b) The co-registered images of the rabbit thigh (an area around the tumor) in DCE-MRI and c) in CE-US. It can be seen in these images that the contrast enhanced US and dynamic contrast enhanced MRI modalities are complementary to each other. MR shows the soft tissue more clearly while US shows a well defined vascular network. This figure shows the US and MR datasets were correctly acquired in the plane and the co-registration process was able to align them with good accuracy.

2.3.3 Contrast Enhanced ultrasound (CE-US) imaging

Diagnostic ultrasound imaging enables visualization and assessment of physiological structures with real-time images. Conventional ultrasound techniques such as Doppler

40

ultrasound can be used to assess blood flow. However, they are not sensitive enough to visualize small blood vessels and are useful only for assessing large blood vessels with fast flowing blood (e.g. carotid arteries, leg veins, portal vein). Thus, these techniques cannot be used for tissue perfusion studies [132], [133].

Contrast enhanced ultrasound (CE-US) on the other hand, which uses microbubbles (1-10 [µm] in diameter) [134] as contrast agent and employs specialized imaging techniques, is capable of showing small blood vessels and can be used for studying tissue perfusion. The contrast agent enhances the signal from the blood and the specialized imaging techniques suppress the signal from the background tissue. Microbubble contrast agents are comprised of small bubbles of gas in a supporting shell [132]. These microbubbles are small enough to pass through small blood vessels and are large enough to stay intravascular (unlike DCE-MRI contrast agents that leak through the tumor vasculature). Thus, the signal in CE-US arises only from the microbubbles inside the vasculature and there is no extravascular signal.

Although CE-US can be used to obtain quantitative perfusion information, it provides no information about permeability [135]. In addition, due to the differences in the kinetics of the CE-US and DCE-MRI contrast agents (e.g. different clearance mechanisms, no contrast agent leakage in US, etc.) and the technical difficulties in obtaining images of the same FOV in both modalities, the intravascular signal obtained from CE-US cannot be used in pharmacokinetic modeling of tumors with DCE-MRI. However, CE-US can be used to visualize the tumor vasculature with high accuracy. In this study we have used CE-US images to evaluate our estimation of the intravascular space in the spatial domain.

Ultrasound imaging in this study was performed using an iU22 ultrasound system (Philips Medical Systems, Bothell, WA,) with a linear array transducer (L9-3, 3-9 [MHz] bandwidth) operating in a mode that provides anatomic and contrast-specific images. Definity (Lantheus Medical Imaging, MA, USA) microbubbles were used as the contrast agent. A low mechanical index (MI) of 0.05 was chosen to minimize microbubble disruption in contrast imaging. To achieve an adequate temporal resolution for tracking the contrast agent, a frame rate of 8-10 [Hz] was used and the imaging was performed for 3 [min] in all studies. The CE-US dataset was acquired with temporal resolution of 100-125 [µs] and the pixel size of the images was 136 [µm] in both axial and lateral directions [128].

The VX2 tumors in rabbits were imaged with DCE-MRI and CE-US for all 4 rabbits (two planes were imaged for each tumor) and the images of the two modalities were co-registered

41

[128]. Figure 2-6a shows the full field of view for co-registered ultrasound and MR images of one of the rabbits. The reduced field of view comparisons of different acquisitions (MRI and US) showing the VX2 tumor are shown in Figure 2-6b and Figure 2-6c respectively.

2.4 Prostate MR imaging

Multi-parametric MR images of a cohort of 27 prostate cancer patients were acquired[3] and are used to assess the performance of the VIF calculation algorithm (AC-ICA). The proposed AC-ICA algorithm was used to calculate VIF and pharmacokinetic analysis was performed on the prostate DCE-MRI datasets. The results were comparing to using an AIF measured at the femoral artery in the pharmacokinetic analysis (chapter 5).

2.4.1 Multi-parametric MR Imaging

Magnetic resonance imaging of prostate was first performed in mid 1980s and has since become a mature imaging modality for prostate cancer diagnosis [136][137]. To use MRI in prostate cancer diagnosis both anatomical and functional information that this modality provides have to be used. The combination of anatomical T_2-weighted MR imaging and several functional imaging techniques such as DCE-MRI, apparent diffusion coefficient (derived from diffusion weighted MRI) and MR spectroscopic (MRS) imaging are usually used to increase accuracy in prostate cancer diagnosis. Although these multiparametric MR imaging techniques contribute to prostate cancer diagnosis, their results in detection, localization, and staging of the cancer vary significantly between studies and need to be improved [115]. The T_2-weighted MRI, apparent diffusion coefficient and DCE-MRI that are used in the thesis will be introduced briefly in this section. A sample frame of DCE-MR images of one of the prostate cancer patient is shown in Figure 2-7 along with its T_2-weighted image and apparent diffusion coefficient (ADC) map generated using its diffusion weighted MR images.

2.4.1.1 T_2-weighted MRI

The T_2-weighted MR imaging which uses a long echo time (TE) and a long repetition time (TR), depicts the differences in the spin-spin relaxation times of various tissues. T_2-weighted images of the prostate are acquired with high spatial resolution and can clearly differentiate

---

[3] The Multi-parametric MR imaging of the prostate cancer patients were performed at Sunnybrook Health Sciences Centre and were provided by Dr. Masoom A. Haider.

the peripheral zone from the central and transition zones particularly in young subjects [138]. In these images that are used to visualize the prostate anatomy, prostate tumor in the peripheral zone (PZ) appears as a hypointense region surrounded by high intensity normal PZ tissue (Figure 2-7b). The degree of signal loss changes with Gleason score (lower intensity for higher Gleason score tumors) and the density of the tumor [139]. The tumors in central and transitional zones are usually difficult to detect, however regions of homogeneously low signal intensity with ill-defined edges or with invasion into the urethra might be cancerous [140]. The main issue of T_2-weigthed MRI is that low signal intensity regions do not always represent cancer and can be due to benign abnormalities (e.g. prostatitis and scar) [141].
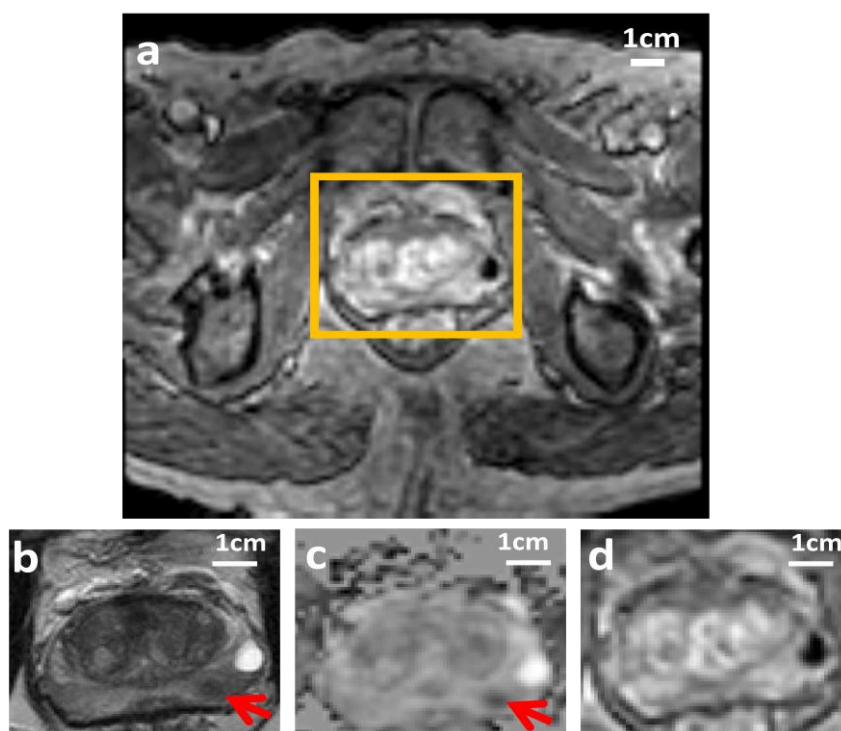
Figure 2-7 a) Full field of view of the DCE-MR images which shows the prostate region used in ICA analyses (yellow box), b) the T_2-weighted image, c) the ADC map, and d) the prostate in the DCE-MR image of the prostate. The cancer in the peripheral zone of the prostate which appears as a hypo-intense region in T_2-weighted image and ADC map is identified with red arrows.

2.4.1.2 Apparent Diffusion Coefficient

Diffusion weighted (DW)-MR imaging applies a motion encoding gradient which causes phase shift in moving protons and generates an image that depends on the direction and amplitude of these movements. The MR signal attenuation that is caused by the motion depends on the motion encoding gradient (b-value) which expresses the amount of diffusion weighting and the apparent diffusion coefficient (ADC) of the tissue which reflects the motion of water molecules during the applied pulse [142]. The ADC map (Figure 2-7c) that is

generated using two or more DW images with different b-values, reflects both the capillary perfusion and the diffusion characteristics of the tissue [143].

Apparent diffusion coefficient calculation [144] requires at least two diffusion weighted images of the tissue with different diffusion gradient b-values. The signal intensity of a tissue decays exponentially as the b-value is increased. This relationship is given with equation 2-1:

$$SI_{b_1} = SI_0 \exp(-b\,ADC) \tag{2-1}$$

where SI_{b_1} is the signal intensity at b-value of $b_1 (b = b_1)$ and SI_0 is the signal intensity at b-value of 0 (b = 0). Having SI_{b_1} and SI_0 from two DW-MR images, the ADC can be calculated as:

$$ADC = -\frac{1}{b_1} \ln\left(\frac{SI_{b_1}}{SI_0}\right) \tag{2-2}$$

Prostate cancer destroys the tubular structure of the prostate and also has a higher cellular density which results in lower diffusion of molecules and hence lower ADC (particularly in PZ) compared to healthy prostate tissue [145]. However, due to the dependence of ADC to imaging sequence and parameters, there are discrepancies between the reported values for prostate cancer in different studies. Moreover, there is inter-subject and intra-subject overlap between ADC values of healthy and cancerous prostate tissues which limits its diagnostic capability [146].

2.4.1.3 Dynamic Contrast Enhanced (DCE)-MRI

Dynamic contrast enhanced (DCE)-MR imaging involves an intravenous injection of a bolus of low molecular weight contrast agent, e.g. Gadolinium (Gd)-DTPA, followed by repeated T_1-weighted MR imaging of the prostate area to monitor the passage of the bolus through the prostate vasculature (Figure 2-7d). The signal intensity change in the DCE-MR images is due to several factors such as the native T_1 of the tissue, contrast agent concentration, imaging parameters and the behavior of the contrast agent in the physiology [147].

The dynamic DCE-MRI sequence can be used to extract qualitative information (e.g. shape of the signal intensity-time curve), semi-quantitative information (e.g. washout rate of the contrast agent), or quantitative information (e.g. contrast agent exchange rate between intravascular and extravascular extracellular spaces) about contrast agent kinetics as it passes through prostate tissue. Such information can be utilized in prostate cancer detection, diagnosis and localization [115]. However, there are several shortcomings in analyzing the

DCE-MR images of prostate such as differentiating the PZ cancer from highly vascular BPH in transitional zone or prostatitis in PZ, lack of standardized approaches for calibration, and analysis and lack of consensus in acquisition protocols [148]. The focus of this thesis is on quantitative analysis of the contrast agent kinetics in the prostate vasculature and aims at improving these methods.

2.4.2 Patient population

A total of 28 MRI datasets (27 patients with one patient being imaged twice), where both the magnitude and the phase images were available in their DCE-MRI sequence, were included in this study. The patients had elevated PSA readings and some of them had undergone TRUS-guided biopsy before imaging or were biopsied after imaging was performed. Details of the patient age, PSA reading and biopsy results (tumor location and Gleason score) are summarized in Table 2-1.

Table 2-1 Summary of patient and tumor characteristics of MRI datasets (PZ refers to the peripheral zone, and CZ refers to the central zone).

Parameter	Number	Location
Number of patients	27	-
Number of datasets (n)	28	-
Number of patients biopsied	27	-
Number of Gleason 6 (3+3) cases	11	4 PZ, 7 CZ
Number of Gleason 7 (3+4) cases	1	PZ
Number of Gleason 7 (3+4) cases	4	PZ
Number of negative biopsy cases	12	-
Parameter	**Mean**	**Range**
Age [years]	66	46-78
PSA $\left[\frac{ng}{l}\right]$	9.32	[0.9-21.44]

2.4.3 DCE-MR imaging

MR imaging was performed on a 3T Achieva Philips scanner (Philips Medical Systems). A set of images were acquired to localize the prostate followed by several image sets to depict the prostate anatomy and enable PK parameter calculation. Anatomical images were obtained using T_2-weighted spin echo (SE) sequence acquired in sagittal, axial and coronal planes. The

T_2-weighted imaging was followed by axial diffusion weighted imaging (DWI) with two diffusion gradient b-values of $b = 0$ $[\frac{s}{mm^2}]$ and $b = 1000$ $[\frac{s}{mm^2}]$. These DW images were used to generate maps of apparent diffusion coefficient (ADC). Diffusion weighted imaging was followed by acquiring multiple flip angle T_1-weighted images with two flip angles of $FA = 5°$ and $FA = 15°$ that were used to generate the pre-contrast T_1-maps of the prostate tissue. The final step of the MR imaging was DCE-MR imaging which was performed using 3D SPGR sequence where the contrast agent, Magnevist (Gd-DTPA), was injected intravenously with a dose of 4 $[\frac{mMol}{Kg}]$.

The T_2-weighted, DW and T_1-weighted (multiple flip angle and DCE) MR images were acquired over field of views of 15 [cm], 24 [cm] and 20 [cm] respectively. For each MR sequence a total of 20 axial planes through the prostate were imaged with a slice thickness of 3.5 [mm] and spacing of 3.5 [mm] between slices. The DCE-MR imaging was performed for approximately 6 [min] (with a temporal resolution of approximately 4.8 [s]) where 75 frames were acquired. Imaging parameters details for each MR sequence are given in Table 2-2.

Table 2-2 Details of MRI sequences that are used in T_2-weighted, DW and T_1-weighted MR imaging of the prostate tissue.

Sequence	TR/TE [ms]	Flip Angle [degrees]	b-value $[\frac{s}{mm^2}]$	FOV [cm]	Slice thickness [cm]	Reconstructed Matrix
T2w-axial	6800/120	90	-	15×15	3.5	224×224
T2w-sagittal	3000/120	90	-	15×15	3.5	224×224
T2w-coronal	3000/120	90	-	15×15	3.5	224×224
DWI	4120/60	90	0 & 1000	24×24	3.5	144×144
Multi-FA (SPGR)	10/1.81	5 & 15	-	20×20	3.5	112×112
DCE-MRI (3D-SPGR)	3.91/1.81	8	-	20×20	3.5	112×112

2.5 Summary

This chapter presented details of the following datasets:

1-   The numerical phantom that was designed (both dynamic contrast agent concentration modeling and MR image simulation)

2-   The physical tissue-mimicking phantom and its DCE-MR imaging

3-   The rabbit VX2 tumor model and its imaging with both DCE-MRI and contrast enhanced ultrasound, that are used for evaluating the VIF calculated using the Mag-ICA algorithm

4-   The MRI data of prostate cancer patients that are used in the thesis to assess the performance of the AC-ICA algorithm for VIF calculation.

The next chapter (chapter 3) presents the Mag-ICA algorithm for calculating the VIF which uses a fixed non-linearity function in its ICA implementation and is applied to the magnitude of the MR images. Chapter 3 also presents the results of applying the Mag-ICA algorithm to DCE-MR images of the numerical phantom, physical phantom, and VX2 tumor model in rabbits. It will also discuss the results and their problems, and explains the reasons that a more sophisticated VIF calculation algorithm was required for analyzing clinical DCE-MRI data which led to the development of the AC-ICA algorithm (chapter 4).

Chapter 3

Feasibility of VIF Calculation Using ICA[4]

The details of the numerical phantom that was constructed and simulation of its DCE-MRI images, the physical tissue-mimicking phantom and its DCE-MR imaging, the rabbit VX2 tumor model and its imaging with both DCE-MRI and contrast enhanced ultrasound, and the DCE-MRI data of prostate cancer that are used in the thesis to assess the performance of the VIF calculation algorithms were presented in the previous chapter (Chapter 2). In this chapter the feasibility of calculating VIF using ICA is studied. An ICA-based VIF calculation algorithm (Mag-ICA) is first introduced in this chapter that has a fixed non-linearity function in its ICA implementation and uses the magnitude of DCE-MR images. This algorithm is then applied to DCE-MR images of the numerical phantom, physical phantom, and rabbit VX2 tumor model and the results are presented. This chapter also discusses the results of Mag-ICA (in the discussions section) and explains (in summary section) the need for a more sophisticated VIF calculation algorithm for analyzing clinical DCE-MRI data which led to the development of the AC-ICA algorithm (chapter 4).

3.1 ICA model for MRI data

Each voxel in an MR image is partially occupied by blood vessels or the intravascular space and the rest is occupied by the extravascular structures. Thus, the MR signal in each voxel is the sum of the signal that is generated in the intravascular space and the signal from the extravascular space. The low molecular weight contrast agents used in DCE-MRI studies do

---

[4] The material presented in this chapter is reproduced from the following publication:

[1] Hatef Mehrabian *et al.*, "Arterial input function calculation in dynamic contrast-enhanced MRI: an in vivo validation study using co-registered contrast-enhanced ultrasound imaging", *European Radiology* 22 (8), pp. 1735-1747, (2012).

ICA implementation of Mag-ICA algorithm was also presented and explained in more detail in the following publication:

[2] Hatef Mehrabian *et al.,* "A constrained independent component analysis technique for artery-vein separation of two-photon laser scanning microscopy images of the cerebral microvasculature", Medical Image Analysis, 16 (1) , pp. 239-251, (2012).

not enter the cells, hence the signal can be assumed to be generated in the intravascular and the extravascular extracellular spaces (EES). This linear mixing of the intravascular and EES signals to form the MR image led us to investigate the possibility of unmixing or separating these signals using a blind source separation (BSS) algorithm known as independent component analysis (ICA). ICA has been applied to AIF measurement in brain perfusion studies [149], however this is a less complex problem than the one we address in this study as the presence of the blood brain barrier minimizes the extravascular contrast enhancement. The separation of intravascular and extravascular components in tumor studies using ICA has not been addressed before.

3.1.1 Spatial Independent component analysis

Spatial Independent component analysis (ICA) is a statistical signal processing algorithm that attempts to split a dataset into its underlying features, assuming these features are statistically independent and without assuming any knowledge of the mixing coefficients [98]. When the features are mixed linearly, the spatial ICA model is expressed as:

$$\mathbf{X} = \mathbf{AS} \qquad (3\text{-}1)$$

where $\mathbf{X} = [\mathbf{x_1}, \mathbf{x_2}, \dots, \mathbf{x_N}]^T$ represents the time-series dataset which in this study is the magnitude of the DCE-MRI data of a tumor or a tissue-mimicking phantom (observed mixtures) and N is the number of time point in the DCE-MRI sequence, $\mathbf{S} = [\mathbf{s_1}, \mathbf{s_2}, \dots, \mathbf{s_M}]^T$ is a matrix containing the M underlying structures that are known as spatially independent components or ICs (usually $M \leq N$) and in this study these are the images representing the intravascular and extravascular extracellular spaces of the tumor tissue. Although we assume that there are only 2 spaces in our model (intravascular and extravascular extracellular), since ICA makes no assumption about the spatial distribution of these spaces, it might split each space into several components. In practice more than 2 ICs are required to achieve accurate separation, i.e. each space (intravascular or extravascular) might be represented with more than one IC. $\mathbf{A} \in \mathbb{R}^{N \times M}$ is the mixing matrix whose columns represent the contrast uptake curves of the intravascular and extravascular extracellular compartments. Having the observed mixed signal $\mathbf{X}$, the ICA algorithm attempts to estimate the underlying features (independent components) $\mathbf{S}$ and the mixing matrix $\mathbf{A}$ assuming that rows of $\mathbf{S}$ are statistically spatially independent. This is achieved by finding an unmixing matrix $\mathbf{W} \in \mathbb{R}^{M \times N}$ and estimating the IC matrix $\mathbf{Y} = [\mathbf{y_1}, \mathbf{y_2}, \dots, \mathbf{y_M}]^T$ such that:

$$Y = WX \tag{3-2}$$

where the rows of **Y** are statistically spatially independent and have zero mean, unit variance ($E\{YY^T\} = I$) and, $E\{.\}$ is the expectation operator. The IC's can be recovered up to a scaling and permutation [98].

3.1.2 Magnitude ICA (Mag-ICA)

According to the central limit theorem, the distribution of a sum of independent random variables with finite support probability density functions (pdf) tends towards a Gaussian distribution [150]. Thus, by maximizing the non-Gaussianity of the estimated components, the independent components can be identified. In an information theoretic framework, one way of measuring non-Gaussianity of a real-valued random variable ($\mathbf{y}$) is to measure its Negentropy [98] given by:

$$J_{negentropy}(\mathbf{y}) = H(\mathbf{y}_{gauss}) - H(\mathbf{y}) \tag{3-3}$$

where $H(\mathbf{y}) = -E\{log(p(\mathbf{y}))\}$ is the differential entropy of $\mathbf{y}$, $p(.)$ is the probability density function (pdf), $\mathbf{y}_{gauss}$ is a Gaussian random variable with the same variance as $\mathbf{y}$, and $log(.)$ is the natural logarithm. Since the probability distributions of the ICs are not known, it is common in ICA algorithms to maximize the Negentropy by maximizing the following equation [97], [151]:

$$J_{negentropy}(\mathbf{w}) = \left[E\{G(\mathbf{y})\} - E\{G(\mathbf{y}_{gauss})\}\right]^2 \tag{3-4}$$

where $\mathbf{w}$ is a column of the unmixing matrix, $\mathbf{y} = \mathbf{w}^T\mathbf{X}$, and $G(.)$ is a non-quadratic non-linearity function. The proposed Mag-ICA algorithm used the third moment of $\mathbf{y}$ as its contrast function, $G(\mathbf{y}) = \mathbf{y}^3$.

Considering the fact that the second term in equation 3-4 is constant, maximizing Negentropy is equivalent to maximizing the following equation with respect to $\mathbf{w}$ (subject to the constraint $\|\mathbf{w}\| = 1$) [97], [151]:

$$J_{negentropy}(\mathbf{w}) = |E\{G(\mathbf{w}^T\mathbf{X})\}| \tag{3-5}$$

This constrained optimization which is maximizing the absolute value of skewness on unit sphere for Mag-ICA algorithm was solved using a quasi-Newton method. The Lagrangian function for this optimization is [97]:

$$L(\mathbf{w}, \lambda) = J_{negentropy}(\mathbf{w}) + \lambda(\mathbf{w}^T \mathbf{w} - 1) \qquad (3\text{-}6)$$

where λ is the Lagrange multiplier. The fixed point update for $\mathbf{w}$, at iteration k, derived from equation 3-6 is as follows [97]:

$$\mathbf{w}_{k+1} = -E\{G'(\mathbf{w}_k^T \mathbf{X})\mathbf{X}\} + E\{G''(\mathbf{w}_k^T \mathbf{X})\}\mathbf{w}_k \qquad (3\text{-}7)$$

where G' and G'' are the first derivative and the second derivative of G respectively.

3.1.3 ICA implementation and VIF identification

Dimensionality reduction was performed on the DCE-MRI data as a pre-processing step in order to reduce noise. This step was performed on each dataset through singular value decomposition (SVD) of the covariance matrix of the data and only the eigenvalues that were larger than 0.1% of the largest eigenvalue (significant eigenvalues) were kept which translated into keeping approximately 99.9% of the information in the dataset. The data was then Whitened by making its rows zero-mean and unit variance [151]. The ICA algorithm (as explained in the previous section) was applied to the dataset after dimensionality reduction and Whitening. The number of extracted independent components (IC) was equal to the number of significant eigenvalues which were kept at the dimensionality reduction step. The intravascular components were selected heuristically such that the curve or curves that had uniform pre-contrast uptake phase, an uptake phase in which the intensity increased rapidly and a washout phase in which the intensity dropped to less than 60% of the peak value after the peak were selected as the intravascular components (if more than one IC satisfied this criterion, they were combined using the method that is explained in section 5.1.1). This heuristic criterion was selected as we observed throughout our study that the time-intensity curves of the components that behaved like an intravascular signal dropped to less that 60% of their peak value.

The intravascular component MR signal has to be converted into contrast agent concentration to represent the VIF and be used in pharmacokinetic modeling. This step will be explained in chapter 5 where PK modeling will be performed on DCE-MR images of prostate cancer

patients. The next section presents the results of applying Mag-ICA algorithm to several DCE-MRI datasets.

3.2 Mag-ICA separation results

The Mag-ICA algorithm for VIF calculation was applied to the numerical phantom and to the physical tissue-mimicking phantom to separate the signal of the tubes, which represented the intravascular signal, from the DCE-MR images. This algorithm was also applied to the *in vivo* DCE-MRI of VX2 tumors in rabbit thigh muscle and the intravascular signal was separated. The Mag-ICA algorithm was implemented in MATLAB (The MathWorks Inc., Natick, USA) software and was applied to the DCE-MRI datasets on a Pentium IV PC with 3.00 GHz Core2 CPU and 3 GB of RAM.

3.2.1 Numerical phantom

The Mag-ICA algorithm was applied to all simulated datasets (four different resolutions) and the signal from inside the tubes (intravascular signal) was extracted. The number of the eigenvalues that were kept for analysis after dimensionality reduction (section 3.1.3) ranged between 5 and 8 which is the maximum number of IC's that could be estimated. In all cases, all IC's were estimated and the IC that corresponded to the tubes' signal was selected heuristically. In brief, the IC that had a uniform pre-contrast uptake followed by a rapid contrast uptake and also a rapid washout of the contrast agent to less than 60% of the peak signal intensity within 3 [min] of bolus injection was selected as the tubes' signal. The 3 [min] threshold is selected here for the numerical phantom, however it has to be determined if DCE-MRI of other tissues or phantoms are being analyzed.

Figure 3-1 illustrates the Mag-ICA intravascular signal separation algorithm and the heuristic intravascular component identification for the numerical phantom. This figure shows the results of applying Mag-ICA algorithm to DCE-MR images of the numerical phantom reconstructed with in-plane resolution of 300 [μm]. Mag-ICA algorithm was applied after dimensionality reduction and Whitening, and all independent components (n = 5 in this case) were extracted. Figure 3-1 shows the extracted ICs in both spatial and temporal domains. In this particular dataset the component number one (IC 1) was selected as the intravascular IC according to the heuristic criterion.
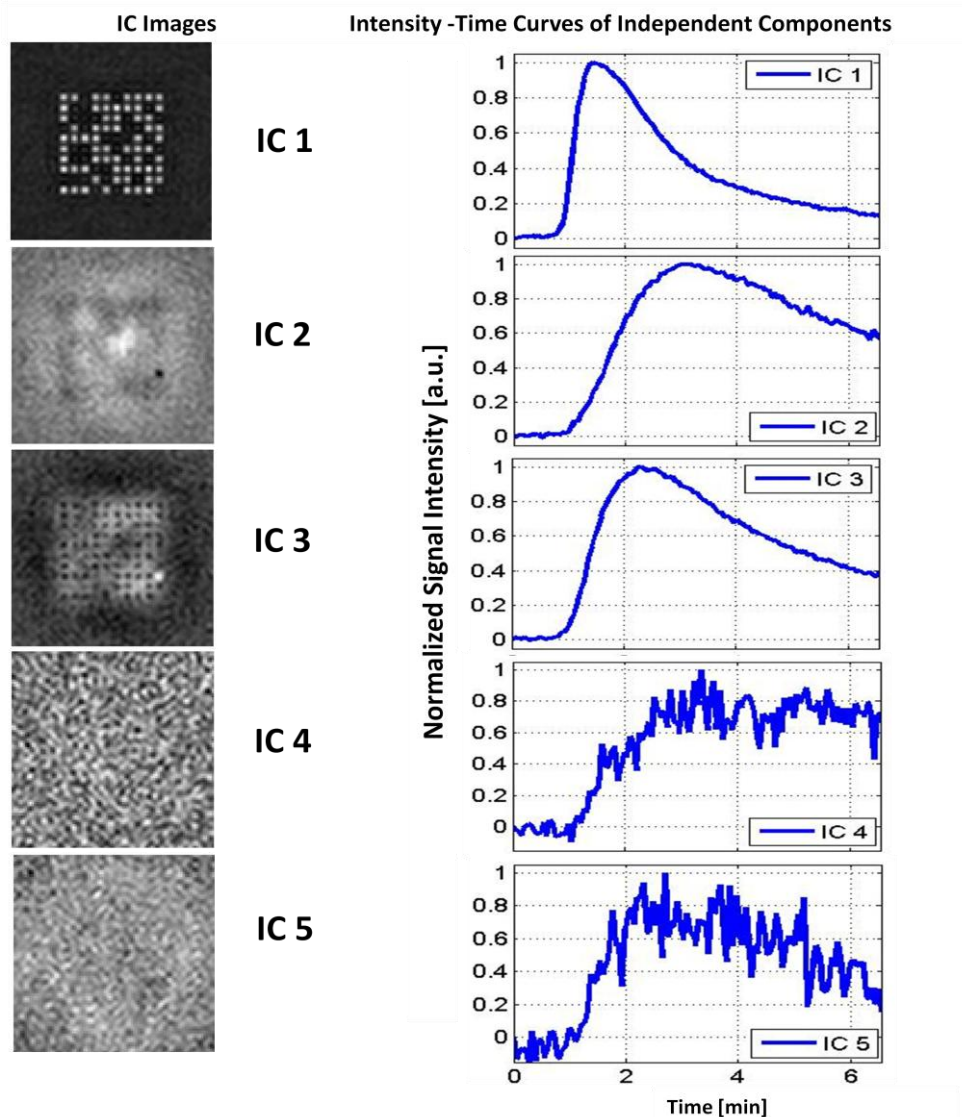
Figure 3-1 The results of applying Mag-ICA algorithm to DCE-MR images of numerical phantom with in-plane resolution of 300 [μm]. The figure shows the 5 spatially independent component images (5 eigenvalues were kept in the dimensionality reduction step) on the left column, and their corresponding temporal components on the right column (these curves are normalized with respect to their maximum values and their baseline value is removed). The only temporal curve that had the pre-contrast uptake and washout phases and in the washout phase its value dropped to 60% of the peak value within 3 [min] was component number 1 (IC 1). Thus, this component was selected as the intravascular component and its time-intensity curve was used as the VIF.

Figure 3-2 shows the results of applying the Mag-ICA algorithm to the simulated DCE-MR images of different resolutions. The intravascular component images for all datasets (4 different resolutions) are shown in Figure 3-2a-d. Figure 3-2e shows the intravascular time-intensity curve of the 4 datasets. These curves represent the average signal intensity over time of all the voxels that are separated by Mag-ICA as the intravascular space (tubes). Figure 3-2e also shows the actual intravascular time-intensity curve which was used in the

simulation of DCE-MRI data as well as the raw data curve calculated by averaging the signal across the full FOV of the MRI images (without post processing) over time. The time-intensity curves are normalized with respect to their maximum and the baseline signal intensity is set to zero in order to enable comparison. Although the separated tubes' signals for different resolutions look very different spatially, their time-intensity curves are similar and have the same arrival times as the actual tubes signal.
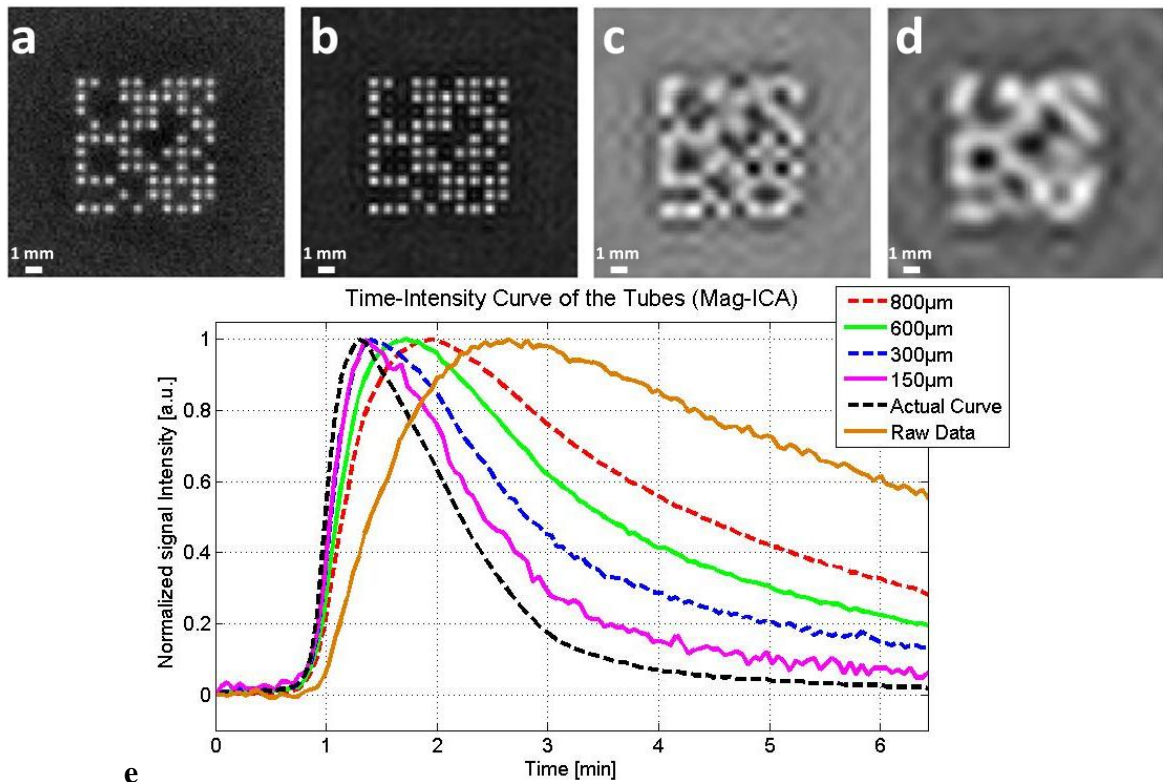
Figure 3-2 The separated tubes' image and the time-intensity curve of the tubes calculated using Mag-ICA for each of the four simulated DCE-MRI datasets. Tubes' images for datasets with in-plane resolutions of a) 150 [μm], b) 300 [μm], c) 600 [μm], d) 800 [μm]. e) this plot shows the calculated time-intensity curves of the tubes corresponding to the 4 simulated datasets, the actual time-intensity curve of the tubes (Actual Curve) and the curve corresponding to the mean across the entire raw (not analyzed) images over time (Raw Data).

For each in-plane resolution, 10 DCE-MRI data sets of the phantom were simulated with SNR=20 and the Mag-ICA algorithm was applied to all datasets. Table 3-1 reports the root mean square error (RMSE) between the estimated time-intensity curves of the tubes obtained using Mag-ICA algorithm and the actual curve for all 4 datasets. Table 3-1 also reports the correlation coefficient between the estimated and actual time-intensity curves of the tubes. These values are calculated using the results of applying Mag-ICA to the 10 different

implementations of the phantom for each resolution which differed in the added noise (SNR = 20) and B_0 inhomogeneity (1 [ppm]).

Table 3-1 The root mean square error (RMSE) and correlation coefficient between the estimated tubes' time-intensity curves and the actual curve for 4 dataset in numerical phantom for Mag-ICA algorithm. These values are calculated using the results of applying Mag-ICA to 10 different implementations of the phantom for each resolution. (RMSE and correlation coefficients are calculated after setting the baseline values of the curves to zero and normalizing them with respect to their maximum value).

In-plane Resolution	150µm	300µm	600µm	800µm
	Root Mean Square Error (RMSE)			
Mag- ICA	0.11± 0.03	0.20±0.01	0.31±0.08	0.36±0.04
	Correlation Coefficient			
Mag-ICA	0.96±0.02	0.92±0.01	0.77±0.09	0.69±0.06

3.2.2 Physical tissue-mimicking phantom

The Mag-ICA algorithm was also applied to DCE-MRI images of the physical tissue-mimicking phantom. Similar to the simulation study, dimensionality reduction and Whitening was performed first, which resulted in keeping 5 to 8 significant eigenvalues. Figure 3-3 illustrates the Mag-ICA separation procedure and the heuristic intravascular component identification for the physical phantom with in-plane resolution of 170 [µm]. Mag-ICA was applied after dimensionality reduction and Whitening, and all independent components (n = 6 in this case) were extracted. Figure 3-3 shows the extracted independent components in both spatial and temporal domains. In this particular dataset the component number one (IC 1) was selected as the intravascular component according to the heuristic criterion.

IC Images

Intensity -Time Curves of Independent Components
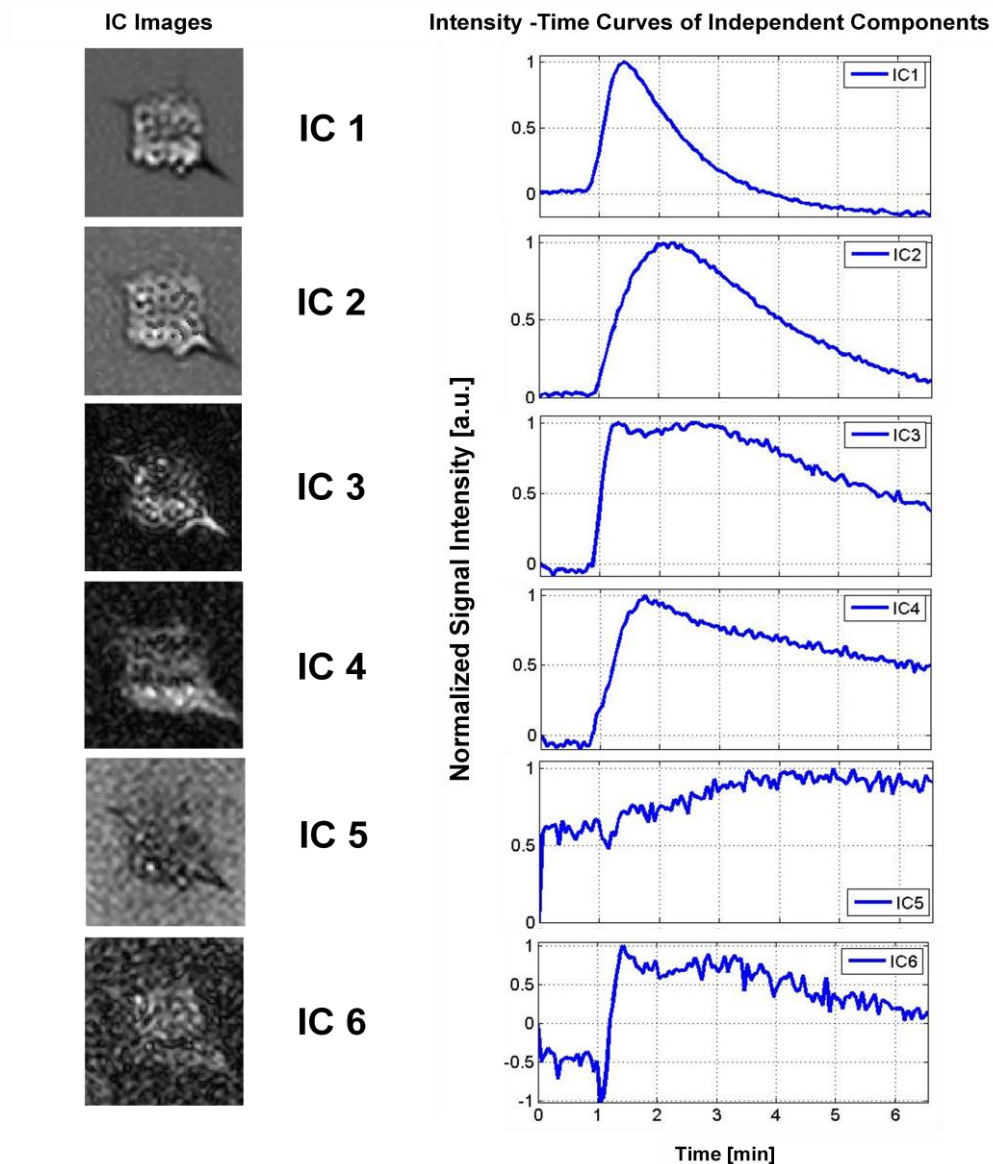
Figure 3-3 The results of applying Mag-ICA algorithm to DCE-MRI of the physical phantom with in-plane resolution of 170 [μm]. The figure shows the 6 spatially independent component images (6 eigenvalues were kept in the dimensionality reduction step) on the left column, and their corresponding temporal curves on the right column (these curves are normalized with respect to their maximum values and their baseline values are set to zero). The only curve that had the pre-contrast uptake and washout phases and, in the washout phase its value dropped to 60% of the peak value after 3 [min] was component number 1 (IC 1). Thus, this component was selected as the intravascular component and its time-intensity curve was used as the VIF.

The phantom data was reconstructed in 5 different in-plane resolutions and separation of the tubes' signal was performed on all 5 datasets and the results are shown in Figure 3-4. The IC images corresponding to the tubes' signal of the 5 datasets are shown in Figure 3-4a-e. The time-intensity curves of the 5 datasets as well as the actual time-intensity curve of the tubes that was measured at the inflow line and the curve measured at the outflow line of the phantom as well as the raw data curve calculated by averaging the signal across the full FOV

56

of the MRI images (without post-processing) over time are shown in Figure 3-4f. The baseline values of the time-intensity curves of all datasets were set to zero and they were normalized with respect to their maximum values. In order to account for their delays in the arrival times of the curves the time-intensity curves of the inflow and outflow lines were shifted to have the same onset time as the ICA curve. Similar to the numerical study, the separated tubes' signals for different resolutions look very different spatially; however their time-intensity curves are similar and are close to the time-intensity curve measured at the inflow and outflow lines.
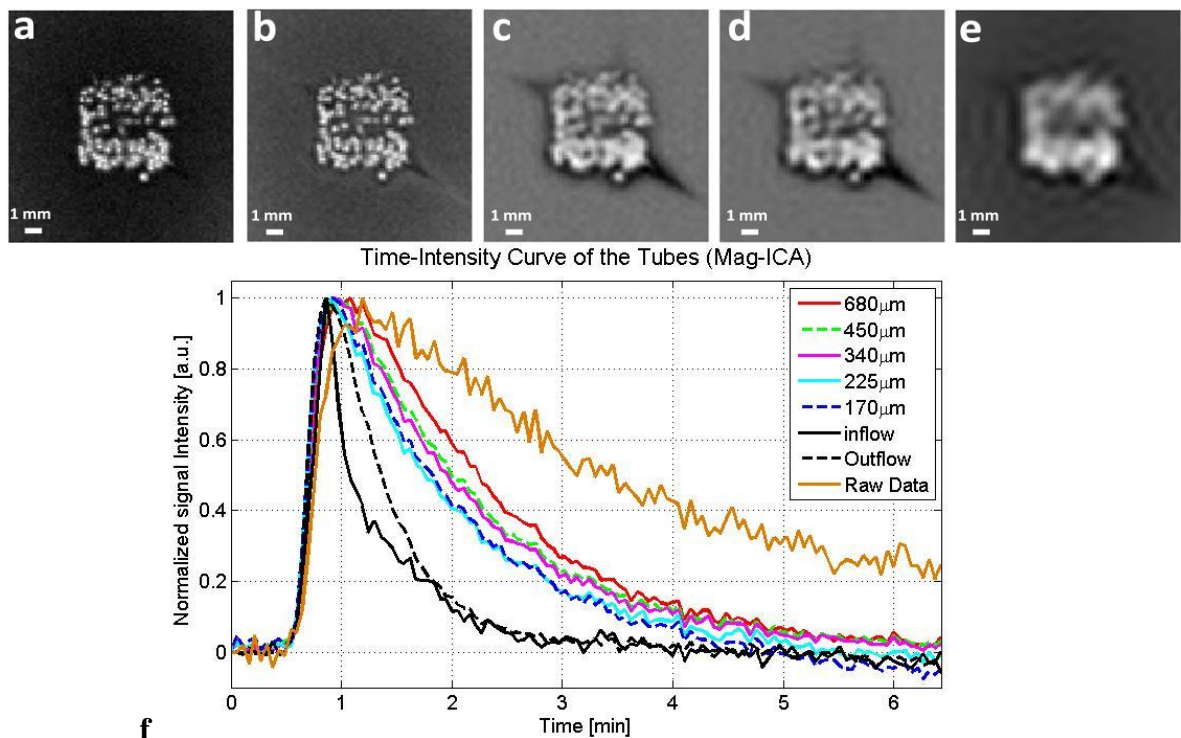
Figure 3-4 The separated tubes' image and the time-intensity curve of the tubes calculated using Mag-ICA for each of the five DCE-MRI datasets for the physical tissue-mimicking phantom. Tubes' images for datasets with in-plane resolutions of a) 170 [μm], b) 225 [μm], c) 340 [μm], d) 450 [μm] and e) 680 [μm]. e) This plot shows the calculated time-intensity curves of the tubes corresponding to the 5 datasets, the actual time-intensity curve of the tubes (inflow line), the time-intensity curve of the tubes at the outflow line, and the curve corresponding to the mean across the entire raw (not analyzed) images over time (Raw Data).

Two physical phantoms were built and DCE-MRI imaging was performed on both phantoms to assess the reproducibility of the results for Mag-ICA intravascular time-intensity curve calculation algorithm. Table 3-2 reports the root mean square error (RMSE) between the estimated and the actual time-intensity curves of the tubes (inflow) for all 5 datasets of both phantoms. This table also reports the correlation coefficient between the estimated and actual time-intensity curves of the tubes for Mag-ICA algorithm in all 5 in-plane resolutions.

57

Table 3-2 The root mean square error (RMSE) and the correlation coefficient between the estimated and actual time-intensity curves of the tubes (inflow) for all 5 datasets of both physical phantoms using Mag-ICA Algorithm (RMSE and correlation coefficients are calculated after setting the baseline of the curves to zero and normalizing them).

In-plane Resolution	170μm	225μm	340μm	450μm	680μm
	Root Mean Square Error (RMSE)				
Mag- ICA	0.20±0.04	0.18±0.01	0.20±0.03	0.21±0.02	0.30±0.05
	Correlation Coefficient				
Mag-ICA	0.88±0.05	0.91±0.02	0.89±0.01	0.88±0.02	0.78±0.08

3.2.3 *In vivo* VX2 tumor (Rabbit)

The final step in assessing the performance of the Mag-ICA algorithm was applying it to DCE-MRI of VX2 tumors in thigh muscle of rabbits and separating their intravascular signal. The Mag-ICA algorithm was applied to the dataset after dimensionality reduction, where about 5 to 8 eigenvalues were kept, and then Whitening, and all independent components were extracted. In order to illustrate the Mag-ICA separation procedure and the heuristic intravascular component identification, Figure 3-5 shows the results of applying Mag-ICA to DCE-MR images of a sample slice in one of the VX2 tumors (the dataset was shown and explained in detail in chapter 2). Mag-ICA was applied after dimensionality reduction and Whitening, and all independent components (n = 8 in this case) were extracted. Figure 3-5 shows the extracted independent components in both spatial and temporal domains. In this particular dataset the component number one (IC 1) was selected as the intravascular component according to the heuristic criterion.

Figure 3-6a shows a sample frame of the DCE-MR images of the tumor (raw data), along with its identified intravascular component using Mag-ICA algorithm. It shows the corresponding co-registered CE-US image as well, which has been averaged over time to reduce noise and to show the areas that are enhancing. Figure 3-6a also shows the normalized time-intensity curves of the identified intravascular component, DCE-MRI signal of the artery that was detected in the imaging plane (the delay in its arrival time was removed to enable comparison of the curves), and the enhancement curve from the CE-US data. The

pre-contrast signal intensities of all curves are removed and the MRI curves are normalized with respect to their area under the curve to enable comparison of their respective enhancement. The CE-US curve had a different shape after peak and lasted for only 3 [min], thus it was scaled to have the same peak as the intravascular MR curve. The same curves and images are shown for the second slice of the tumor in Figure 3-6b. For both slices the actual AIF (measured at the artery) and the intravascular time-intensity curve of the tumor obtained using Mag-ICA are highly correlated and the p-values, assessing how well the ICA curves fit the actual AIF are less than 0.05 (Table 3-3).
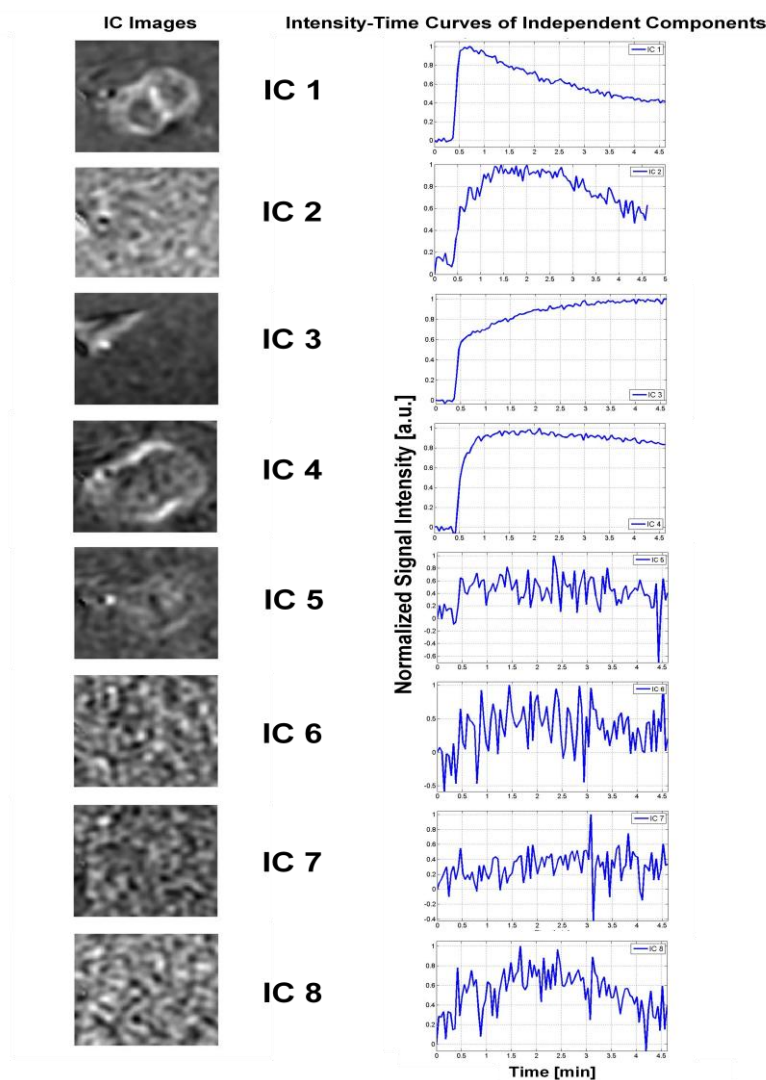
Figure 3-5 The results of applying Mag-ICA algorithm to DCE-MR images of a VX2 tumor in thigh muscle of a rabbit. The figure shows the 8 spatially independent component images (8 eigenvalues were kept in the dimensionality reduction step) on the left column, and the corresponding temporal curves on the right column (the curves are normalized with respect to their maximum values and their baseline values are set to zero). The only curve that had the pre-contrast uptake and washout phases, and in the washout phase its value dropped to 60% of the peak value after 4.5 [min] was IC 1 and was selected as the intravascular component.
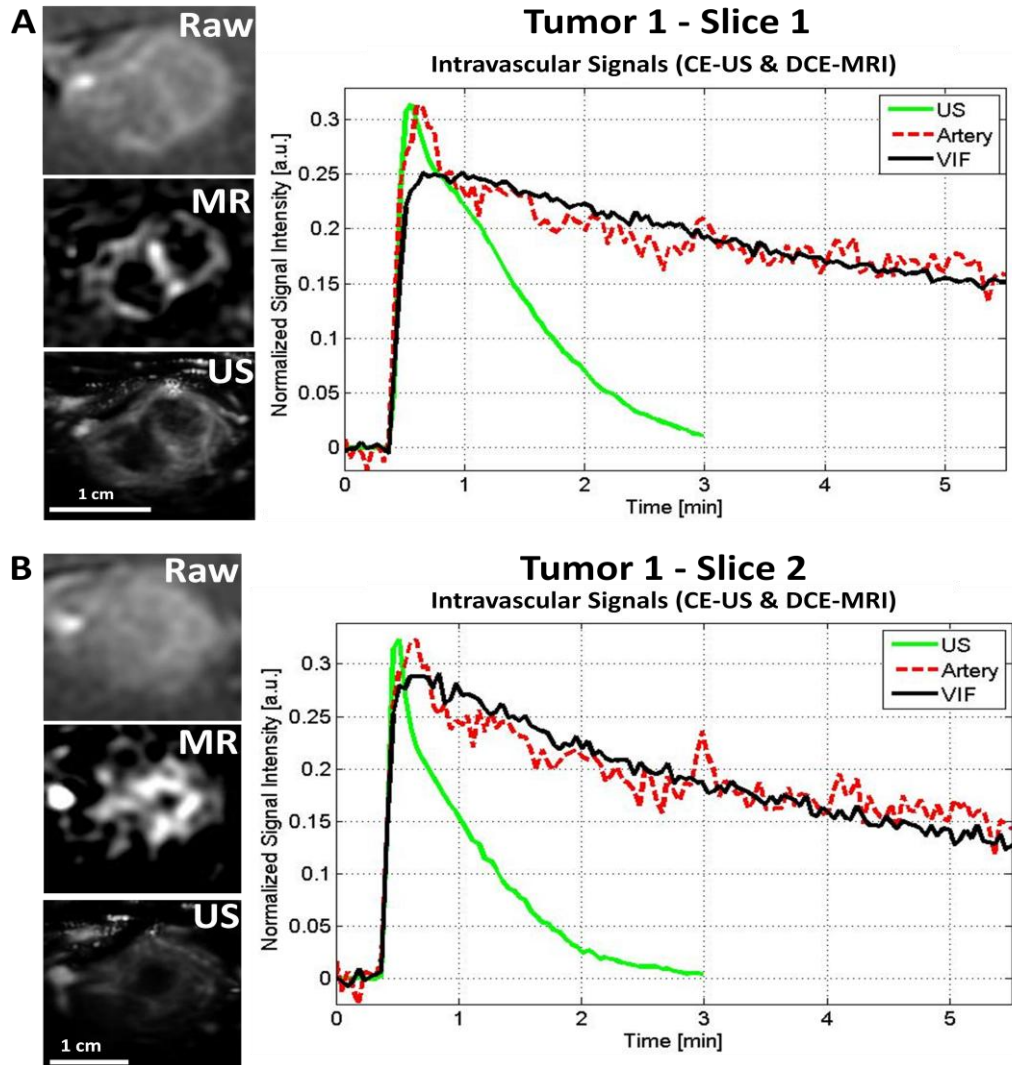
Figure 3-6 Results of applying Mag-ICA algorithm to the DCE-MRI data of the tumor shown in Figure 2-6 and Figure 3-5 in a) Slice 1 and b) Slice 2 of the tumor. This figure shows a sample frame of the raw data (Raw), the intravascular component (MR) that was separated using Mag-ICA in the spatial domain and the corresponding contrast enhanced ultrasound (CE-US) image for both slices. The US image is averaged over time thus the noise is suppressed and the regions that have higher signal intensity (brighter regions) correspond to the areas that have more blood vessels. The plots show the normalized time-intensity curves of the intravascular space obtained by Mag-ICA, the actual AIF measured at the artery that is close to the tumor and the contrast enhancement of the tumor in the ultrasound dataset for both slices. The MRI curves are normalized with respect to their area under the curve and their pre-contrast enhancements are removed to enable comparison. The US curve is scaled to have the same maximum value as the MRI curve of the artery. The intravascular MR images are thresholded by removing the pixels that enhance less that 50% of the maximum intensity value to better visualize the enhancing areas.

Mag-ICA algorithm was applied to all eight datasets (4 tumors and 2 slices for each tumor). For seven datasets the method succeeded in identifying and separating the intravascular component. It failed in one of the datasets where the DCE-MR imaging protocol was adjusted to a lower signal to noise ratio (SNR) in an attempt to acquire images at a higher rate

(NEX=1, temporal resolution=0.9 [s]). Figure 3-7 shows the performance of the method on 5 other datasets (other than the 2 datasets that were shown in Figure 3-6). This figure shows the co-registered contrast ultrasound image of the tumor and Mag-ICA intravascular component.

Table 3-3 The correlation coefficient between the normalized intravascular time-intensity curve extracted by Mag-ICA and the normalized AIF measured from the artery that is located near the tumor (actual AIF) and the p-values, assessing how well the Mag-ICA curves fit the actual AIF for both planes of the tumor.

	Correlation coefficient	p-value
Tumor 1, Slice A	0.92	0.04
Tumor 1, Slice B	0.96	0.03

Table 3-4 reports the onset time (the time point at which contrast agent arrives in the tumor) and the peak time (the time point at which signal intensity reaches its maximum value) of ultrasound and intravascular MR time-intensity curve for both imaging slices of all eight *in vivo* dataset shown in Figure 3-7 (there was no visible artery in MRI slices of other datasets to be compared with the intravascular enhancement of the tumor and thus no correlation coefficients or p-values could be calculated).

Table 3-4 The onset time (the time point at which contrast agent arrives in the tumor) and the peak time (the time point at which signal intensity reaches its maximum) of ultrasound and intravascular MR time-intensity curve for both imaging slices of all four tumors

	Onset Time [min]		Peak Time [min]	
	Intravascular MR	Ultrasound	Intravascular MR	Ultrasound
Tumor 1, Slice 1	0.32	0.41	0.65	0.55
Tumor 1, Slice 2	0.37	0.38	0.60	0.51
Tumor 2, Slice 1	0.50	0.57	0.89	0.80
Tumor 2, Slice 2	0.43	0.55	0.75	0.75
Tumor 3, Slice 1	0.31	0.38	0.54	0.54
Tumor 3, Slice 2	0.31	0.38	0.54	0.54
Tumor 4, Slice 1	0.39	0.39	0.56	0.52
Tumor 4, Slice 2	Failed			
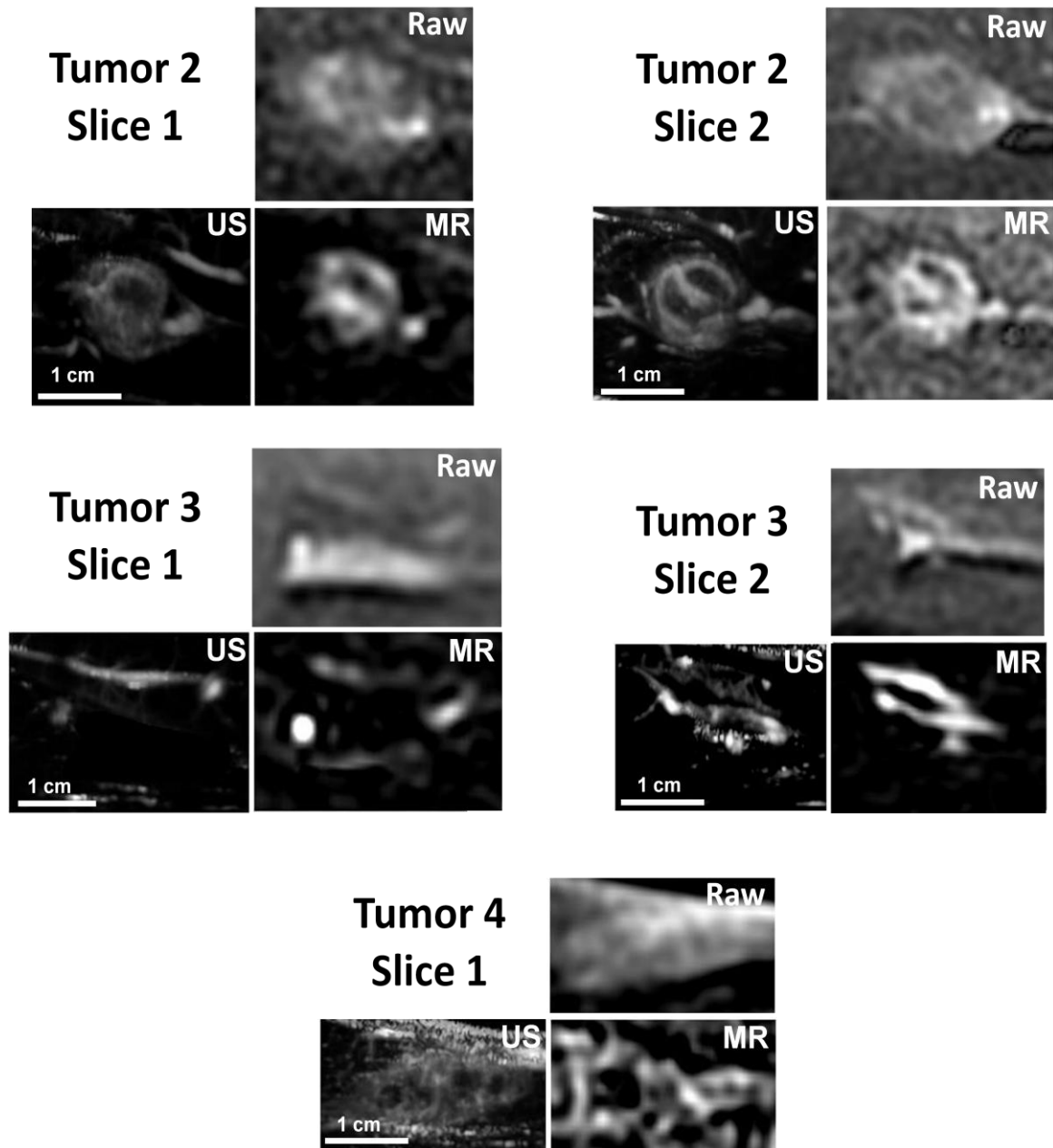
Figure 3-7 Results of applying the proposed separation method to 5 other DCE-MRI datasets. For each dataset a sample frame of the raw data (Raw) and the intravascular component image (MR) that was identified and separated using Mag-ICA algorithm are shown. In addition, the corresponding ultrasound image (US) of each dataset that shows the intravascular components of the tissue (the US data is averaged over time to reduce noise and clearly show the regions that enhance) is shown. The method was applied to the 8 available tumor datasets. In 7 out of 8 datasets the method succeeded in identifying and separating the intravascular space form the dataset. Results for 5 datasets (other than the two datasets that were shown in Figure 3-6) are shown in this figure. The intravascular MR images are thresholded by removing the pixels that enhanced less that 50% of the maximum intensity value to better visualize the enhancing areas. This figure shows the reproducibility of the algorithm in calculating the VIF *in vivo*. In the dataset that the method failed to calculate VIF the imaging parameters were modified to achieve higher temporal resolution which resulted in poor image quality (low SNR).

3.3 Discussions

In a pharmacokinetic model, the determination of vascular parameters relies on accurate measurement of the contrast agent concentration in the plasma volume (AIF or VIF) [152]. However; measuring such a signal in the tumor is usually impossible. Currently an AIF is approximated outside the tumor which may result in inaccurate PK parameters and makes the governing equation complicated. Current AIF measurement techniques have several disadvantages. In many tumors a feeding artery for the tumor in the imaging field of view does not exist which makes PK analysis difficult and inaccurate if not impossible. A theoretical AIF assumes a predefined bi-exponential form for the AIF which is not necessarily correct and does not account for variability between individuals. A population-averaged AIF also does not account for variability between patients and heterogeneity of the tumor vasculature. A reference-tissue based technique requires knowing the PK parameters of normal tissues surrounding the tumor and a dual bolus AIF requires injecting an extra contrast agent bolus.

The proposed Mag-ICA separation algorithm provided promising results in identifying and separating the intravascular signal in DCE-MRI. The initial results obtained in the numerical and physical tissue-mimicking phantoms demonstrated the ability of Mag-ICA in separating the signal from within the tubes (Figure 3-2 and Figure 3-4). They also showed the robustness of the method in dealing with low-resolution DCE-MRI data where these compartments could not be physically separated by voxel boundaries. As shown in Figure 3-2, Figure 3-4, Table 3-1 and Table 3-2 the results of performing the separation on datasets with different resolutions were similar and were relatively close to the actual intravascular (tubes) signal. However as the voxel size was increased (decreasing the resolution), the time-intensity curves began to deviate from the actual curve (delayed peak and longer tail).

Similar results were achieved *in vivo*, where the Mag-ICA algorithm was able to produce intravascular images of tumors that had good resemblance to the contrast enhanced ultrasound images (actual intravascular image). A large artery close to the tumor was also identified in the imaging field of view and was used to evaluate the separation results of our algorithm temporally. This artery was oriented such that it was parallel to the imaging plane. It also extended towards the tumor, as can be seen in figure 3-6, which suggested that it was probably feeding the tumor. These characteristics made this artery a good candidate to be used as the actual AIF signal (such an artery was not present in other datasets).

The accuracy of the proposed method was demonstrated by comparing its separated intravascular time-intensity curves with an arterial enhancement (DCE-MRI) from an artery close to the tumor and with its corresponding CE-US contrast enhancement curve as shown in Figure 3-6 and reported in Table 3-3. All three curves show a similar arrival time and peak time of enhancement, and the actual AIF (measure in the artery) and Mag-ICA curve show similar washout of contrast agent, as would be expected. Also expected is the different rate of decay of the DCE-MRI signals compared to the ultrasound curve, likely due to the different clearance mechanisms (US contrast agent is cleared through longs while MR contrast agent is cleared through kidneys) and clearance rates (US contrast agent gets clear faster than MR contrast agent) for the contrast agents as well as their physiological half lives (in healthy subjects elimination half-life of Magnevist which is the MR contrast agent used in our in-vivo studies is 1.6 [hours] while elimination half-life of definity microbubbles that is the contrast agent we sued in CE-US studies is 1.3 [min]).

Figure 3-7 and Table 3-4 show the results of applying the separation to all datasets. There were eight rabbit tumor datasets available (four rabbits and two slices for each one) and the method succeeded in separating the two spaces in seven datasets. The dataset that the method failed had a higher temporal resolution and thus a much lower signal to noise ratio (SNR) compared to the other seven datasets (3.4 times lower SNR). Therefore, the image quality of the failed dataset was much lower than the other datasets and the method was not able to separate the vasculature.

In conclusion, the Mag-ICA algorithm appears to be capable of separating the intravascular spaces in *in vivo* datasets. The Mag-ICA intravascular curve is very similar to the AIF that was measured in the artery that was located near the tumor. The *in vivo* intravascular component images were also very similar to the tumor vasculature imaged using CE-US. The phantom and *in vivo* studies show that the ICA-based algorithm have the potential to improve the calculation of the AIF, which is required for PK modeling.

In this chapter we used the MR signal intensity to assess the performance of the separation algorithm. However, in order for the intravascular time-intensity curve to be used in PK modeling, it has to be converted into contrast agent concentration. This is not a trivial step as ICA suffers from an intrinsic arbitrary scaling and since it is a data-driven algorithm it might split the intravascular component into several components. The steps required for conversion

of MR signal intensity to contrast agent concentration will be explained in chapter 5 where the ICA-based VIF will be applied to DCE-MRI sequences of prostate cancer patients.

3.4 Summary

This chapter introduced Mag-ICA algorithm and demonstrated its potential in identifying and separating the intravascular signal in DCE-MRI by applying it to numerical and physical tissue-mimicking phantoms as well as *in vivo* rabbit tumor models. Such a data-driven local VIF may improve the results of conventional PK analysis as it allows for an arterial input function to be estimated automatically from the tumor. This shows the potential of this approach in cancer imaging, where it is impossible to find an ROI that identifies and separates the intravascular signal and there might not exist an artery in the imaging field of view. However, the Mag-ICA algorithm has several shortcomings as it used the magnitude of MR images which violates the main assumption (linear mixing of the components) in ICA and also used a fixed non-linearity function in the implementation of ICA which does not account for inter-subject and intra-subject variability in the spatial distribution of the vasculature.

A more rigorous way of addressing these problems is to analyze the complex-valued MRI data rather than the magnitude data and also to estimate the probability distribution of the intravascular signal adaptively as the ICA components are being extracted. These issues led to the development of an adaptive complex ICA (AC-ICA) algorithm (presented in chapter 4) that used the complex-valued MRI data where the linear mixture assumption of ICA was satisfied and also determined the ICA non-linearity function based on the distribution of the vasculature through an expectation maximization (EM) procedure by performing online density estimation at each iteration. The performance of the AC-ICA algorithm was evaluated using simulation and physical tissue-mimicking phantoms that were used in this chapter and is presented in the next chapter (chapter 4).

Chapter 4

Vascular Input Function (VIF) Calculation in

Complex-Valued DCE-MRI[5]

The previous chapter introduced the Mag-ICA algorithm and presented the results of applying the algorithm to DCE-MR images of the numerical phantom, the physical tissue-mimicking phantom, and the rabbit VX2 tumor model which showed its potential in separating the intravascular component. Chapter 3 also briefly introduced the shortcomings of the Mag-ICA algorithm which led to the development of AC-ICA algorithm. Chapter 4 first discusses the limitations of Mag-ICA algorithm in detail and then introduces the AC-ICA algorithm and provides details of its derivation. It also presents the results of applying the AC-ICA algorithm to DCE-MR images of the numerical phantom and the physical tissue-mimicking phantom, and compares these results to those of Mag-ICA algorithm to highlight the superior performance of the AC-ICA algorithm (discussions section). The AC-ICA algorithm will be used in the next chapter for PK analysis of prostate DCE-MRI.

4.1 Limitations of Mag-ICA algorithm

Chapter 3 introduced the Mag-ICA algorithm which used the magnitude of the MRI data (which is common in DCE-MRI studies) and an ICA algorithm with a fixed non-linearity function (which is common in ICA studies). This method was shown to have good performance in calculating the intravascular time-intensity curve and separating it from the DCE-MRI data and its results were evaluated using tissue-mimicking phantoms and contrast enhanced ultrasound imaging of the tumor vasculature *in vivo*. However, the Mag-ICA algorithm has two main shortcomings:

---

[5] The material presented in this chapter is reproduced from the following publication:

[3] Hatef Mehrabian *et al.*, "Calculation of intravascular signal in dynamic contrast enhanced MRI using adaptive complex independent component analysis", *IEEE Transactions on Medical Imaging*, 32(4), pp. 699-710, (2013).

1-   Using the magnitude of the MR signal (i.e. it violates the linear mixture assumption of ICA).

2-   Using a fixed non-linearity function in its ICA implementation (i.e. it assumes the probability density function of the intravascular signal has a fixed shape).

To address these shortcomings an adaptive complex ICA (AC-ICA) algorithm is developed and evaluated in this chapter.

4.1.1 Magnitude vs. Complex-valued ICA

In practice, the main limitation of the Mag-ICA algorithm arises from violation of the ICA assumption that the intravascular and extravascular signals are linearly combined to form the images. There are different tissue types in each MR voxel and their signals contribute to its average MR signal. Even within a single tissue type in a voxel, there will be a small range of magnetic field strengths due to varying molecular environment of spins and proximity to other tissue types. Thus, their magnetization vectors might not be in-phase. Thus, the magnitude of the sum of the signals of these two spaces would not be equal to the sum of the magnitudes of their signals. In other words, assuming the MR signal of a voxel ($\mathbf{x}$) is the sum of its complex-valued intravascular ($\mathbf{x}_{IV} = \mathbf{x}_{IV}^R + i\mathbf{x}_{IV}^I$) and extravascular ($\mathbf{x}_{EV} = \mathbf{x}_{EV}^R + i\mathbf{x}_{EV}^I$) components (where R and I superscripts represent the real and imaginary parts of the signal), the magnitude of the MR signal of the voxel is: $|\mathbf{x}| = (|\mathbf{x}_{IV}^R + \mathbf{x}_{EV}^R|^2 + |\mathbf{x}_{IV}^I + \mathbf{x}_{EV}^I|^2)^{1/2}$. The Mag-ICA algorithm attempts to separate the intravascular component from this magnitude signal, $|\mathbf{x}|$, which is not equal to the sum of the magnitudes of the intravascular and extravascular components ($|\mathbf{x}| \neq |\mathbf{x}_{IV}| + |\mathbf{x}_{EV}|$), and thus violates the linear mixing assumption in ICA (unless these two signals are in-phase). This intra-voxel de-phasing can be reduced by shortening the echo time (TE) and we used a short TE to minimize it (TE = 2.9 [ms] in numerical and physical phantoms and TE = 1.5 [ms] in rabbit VX2 tumors).

4.1.2 Density estimation

In addition to using the magnitude of MRI data, in the Mag-ICA algorithm the probability distribution functions of the intravascular and extravascular extracellular spaces are not estimated and, as is common in ICA algorithms, a fixed non-linearity function is used instead. Using a fixed non-linearity function assumes a pre-defined shape for the probability distribution of the intravascular component spatially (such information is not available in

practice) and also does not account for the inter- and intra-subject variability between the spatial distributions of the tumor vasculature. We examined several ICA non-linearity functions for Mag-ICA and selected the third moment of a random variable as it performed better in separating the intravascular component of DCE-MRI sequences.

A more rigorous way of addressing these problems would be to estimate the probability distribution of the intravascular signal and to use the complex-valued MRI data. The proposed adaptive complex ICA (AC-ICA) method which will be explained in this chapter determines the ICA non-linearity function based on the distribution of the vasculature through an expectation maximization (EM) procedure by performing online density estimation at each iteration on the complex-valued MRI data.

4.2 Adaptive complex independent component analysis

An adaptive complex independent component analysis (AC-ICA) algorithm was developed in this thesis for VIF calculation which used the complex-valued DCE-MRI data and performed density estimation at each iteration. This section first introduces ICA for complex-valued signals and then explains the generalized Gaussian distribution model that was used to derive the non-linearity of the AC-ICA algorithm. The derivation of the AC-ICA algorithm through density estimation at each iteration using an expectation maximization framework is then presented.

4.2.1 Complex ICA

As mentioned in previous chapter, spatial ICA is a statistical signal processing algorithm that attempts to unmix a dataset into its underlying features, assuming they are statistically spatially independent and without any prior information about the features or their mixing processes [98]. The spatial ICA model for a linear mixture is:

$$\mathbf{Z} = \mathbf{AS} \tag{4-1}$$

where $\mathbf{A} \in \mathbb{R}^{N \times M}$ is the mixing matrix, $\mathbf{Z} = [\mathbf{z}_1, \mathbf{z}_2, ..., \mathbf{z}_N]^T$ is the complex-valued DCE-MRI dataset, N is the number of frames, $\mathbf{S} = [\mathbf{s}_1, \mathbf{s}_2, ..., \mathbf{s}_M]^T$ is a matrix containing the M spatially independent components (usually $M \leq N$) and in this study these are the images representing the intravascular space and EES. As explained in the previous chapter, although we assume there are only 2 spaces in our model (intravascular space and EES), since ICA makes no assumption about the spatial distribution of these spaces, it might split each space into several

68

components. Having the observed mixture signals $\mathbf{Z}$, the spatial ICA algorithm attempts to estimate the IC matrix $\mathbf{S}$ and the mixing matrix $\mathbf{A}$. This is achieved by finding an unmixing matrix $\mathbf{W} \in \mathbb{R}^{M \times N}$ and estimating the IC matrix $\mathbf{Y} = [\mathbf{y}_1, \mathbf{y}_2, \ldots, \mathbf{y}_M]^T$ such that:

$$\mathbf{Y} = \mathbf{WZ} \tag{4-2}$$

where the rows of $\mathbf{Y}$ are statistically spatially independent and have zero mean, unit variance (i.e. $\boldsymbol{E}\{\mathbf{YY}^H\} = \boldsymbol{I}$, where H is the Hermitian transform) and, $\boldsymbol{E}\{.\}$ is the expectation operator. The IC's can be recovered up to a scaling and permutation [98].

The Negentropy for a complex-valued random variable is defined using the joint distribution of its real and imaginary parts, i.e. $\boldsymbol{p}(\mathbf{y}^R, \mathbf{y}^I)$ [153]:

$$\boldsymbol{J}_{negentropy}(\mathbf{z}^R, \mathbf{z}^I) = \boldsymbol{H}\left(\mathbf{y}_{gauss}^R, \mathbf{z}_{gauss}^I\right) - \boldsymbol{H}(\mathbf{y}^R, \mathbf{y}^I) \tag{4-3}$$

where $\mathbf{y}^R$ and $\mathbf{y}^I$ are the real and imaginary parts of $\mathbf{y}$, $\boldsymbol{H}(\mathbf{y}^R, \mathbf{y}^I) = -\boldsymbol{E}\{log(\boldsymbol{p}(\mathbf{y}^R, \mathbf{y}^I))\}$ is the bi-variate differential entropy, and $log(.)$ is the natural logarithm. The complex Negentropy is always non-negative, and for a fixed covariance of $[\mathbf{y}^R, \mathbf{y}^I]^T$, the bi-variate differential entropy has its largest value for $\left[\mathbf{y}_{gauss}^R, \mathbf{y}_{gauss}^I\right]$.

Estimating the Negentropy in equation 4-3 is difficult and thus, it is common to use the following equation for approximating Negentropy:

$$\boldsymbol{J}_{negentropy}(\mathbf{w}) = \left[\boldsymbol{E}\{\boldsymbol{G}(\mathbf{y})\} - \boldsymbol{E}\{\boldsymbol{G}(\mathbf{y}_{gauss})\}\right]^2 \tag{4-4}$$

where $\mathbf{y} = \mathbf{w}^H \mathbf{Z}$, and $\boldsymbol{G}(\mathbf{y}) = |\boldsymbol{C}(\mathbf{y})|^2$ in which $\boldsymbol{G}(.)$ is called the contrast function and $\boldsymbol{C}(.)$ is the non-linearity function for ICA. The optimal contrast function in information theoretic sense satisfies $\boldsymbol{p}(\mathbf{y}^R, \mathbf{y}^I) = \exp(-\boldsymbol{G}(\mathbf{y}))$. Considering the fact that the second term in equation 4-4 is constant, maximizing Negentropy is equivalent to maximizing the following equation with respect to $\mathbf{w}$ (subject to the constraint $\|\mathbf{w}\| = 1$) [153]:

$$\boldsymbol{J}_{negentropy}(\mathbf{w}) = \boldsymbol{E}\{|\boldsymbol{C}(\mathbf{w}^T \mathbf{Z})|^2\} \tag{4-5}$$

This constrained optimization can be solved using a quasi-Newton method [153]. The Lagrangian function for this optimization problem is:

$$\boldsymbol{L}(\mathbf{w}, \lambda) = \boldsymbol{J}_{negentropy}(\mathbf{w}) + \lambda(\mathbf{w}^H \mathbf{w} - 1) \tag{4-6}$$

where λ is the Lagrange multiplier. Using the complex Newton update rule defined in [154], the optimization update rule becomes [153]:

$$\mathbf{w}_{k+1} = \mathbf{w}_k - \left(\boldsymbol{H}_J - \lambda \mathbf{I}\right)^{-1}\left(\boldsymbol{\nabla}_J^* + \lambda \mathbf{w}_k\right) \tag{4-7}$$

where $\boldsymbol{H}_J$ and $\boldsymbol{\nabla}_J$ are the complex Hessian and the complex gradient matrices of $\boldsymbol{J}$ respectively. The fixed point update rule for $\mathbf{w}$ was derived from equation 4-7 in [153] as the following equation:

$$\begin{aligned}
\mathbf{w}_{k+1} = &-E\{\boldsymbol{C}^*(\mathbf{w}_k^H \mathbf{Z})\boldsymbol{C}'(\mathbf{w}_k^H \mathbf{Z})\mathbf{Z}\} \\
&+E\{\boldsymbol{C}'(\mathbf{w}_k^H \mathbf{Z})\boldsymbol{C}'^*(\mathbf{w}_k^H \mathbf{Z})\}\mathbf{w}_k \\
&+E\{\mathbf{Z}\mathbf{Z}^T\}E\{\boldsymbol{C}^*(\mathbf{w}_k^H \mathbf{Z})\boldsymbol{C}''(\mathbf{w}_k^H \mathbf{Z})\}\mathbf{w}_k^*
\end{aligned} \tag{4-8}$$

where $\boldsymbol{C}^*$, $\boldsymbol{C}'$ and $\boldsymbol{C}''$ are the complex conjugate, the first derivative and the second derivative of $\boldsymbol{C}$ respectively.

4.2.2 Phase shifting of DCE-MRI data for ICA

Assume a 2-dimensional matrix $\mathbf{Q} \in \mathbb{R}^{N_r \times N_c}$, where N_r represents the number of rows and N_c represents the number of columns of $\mathbf{Q}$, is being used as the input to Fourier Transform (FT) to generate the MRI data. FT assumes that the zero frequency point is the initial point of the signal located at the first row and the first column of $\mathbf{Q}$. However, in MRI data acquisition in k-space, the zero frequency point is stored at the center of the k-space (located at the row $N_r/2$ and column $N_c/2$) and then higher frequency elements are stored around this center point which is not the arrangement that is expected by Fourier Transform.

This rearrangement of the k-space values corresponds to displacement of data located at row n and column m with $N_r/2$ rows and $N_c/2$ columns in k-space, respectively. This is equivalent to a phase shift of $e^{i2\pi n(N_r/2)/N_r}e^{i2\pi m(N_c/2)/N_c} = (-1)^{n+m}$ in image space which translates to a sign alteration of every other point. This phase shift has to be corrected by changing the sign of every other point in complex DCE-MRI data. The phase shift has no effect when using the magnitude of the MRI data but affects the analysis when the complex data is being used. If this phase shift is not corrected prior to the application of ICA, then the values of neighboring voxels cancel out, in particular when computing the mean and the covariance of the signal.

4.2.3 Generalized Gaussian distribution

The optimal non-Gaussianity in an information theoretic framework is the logarithm of the joint probability density function of the source that is being estimated, i.e. $\boldsymbol{G}_{optimal}(\mathbf{z}) = -log(\boldsymbol{p}(\mathbf{z}^R, \mathbf{z}^I))$. However, the joint probability density of the source is not known in ICA and thus has to be estimated. We used the generalized Gaussian distribution (GGD), which covers a wide range of distributions [155] and has been used in modeling various physical phenomena [156]–[158], to model the spatial distribution of the sources (intravascular space and EES) in the implementation of AC-ICA algorithm. The GGD model is given as:

$$g(\mathbf{y}; \alpha, \beta) = \frac{\beta}{2\alpha \boldsymbol{\Gamma}(1/\beta)} exp\left(-\frac{|\mathbf{y}|^\beta}{\alpha^\beta}\right) \tag{4-9}$$

where $\boldsymbol{\Gamma}(.)$ is the gamma function defined as $\boldsymbol{\Gamma}(\boldsymbol{x}) = \int_0^\infty e^{-t} t^{x-1} dt$, and β and α are the model parameters. GGD was introduced in [155] as a non-linearity function for ICA. We have observed that distributions of the real and imaginary parts of the MR images of each compartment (source) fit well into the GGD formulation. There is no theoretical proof for the fact that MR data fit well into GGD model. However, given the wide range of distributions that GGD model covers (shown in the examples in Figure 4-1), using the combination of a number of GGDs is capable of modeling most functions.
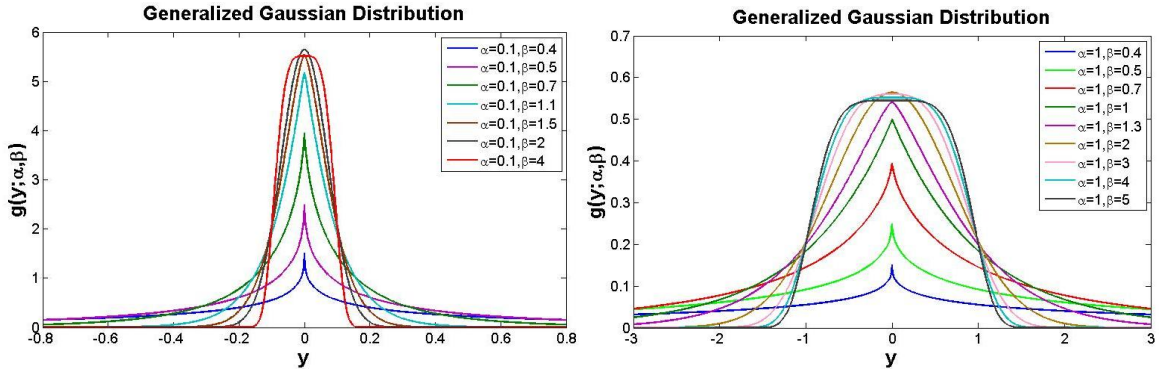
Figure 4-1 Two different families of generalized Gaussian distributions where in each plot α is kept constant ($\alpha = 0.1$ in left plot and $\alpha = 1$ in the right plot) and β is changed.

We investigated this in various MR images and observed that GGD is a good approximation to our distribution of MRI signal in spatial domain. As an example, the histogram of an MR image of the physical phantom where a high resolution image of the phantom was acquired prior to administration of contrast agent (only water was flowing through the tubes) is given in Figure 4-2. These histograms (histogram of the real and imaginary parts of the image)

71

show the distributions fit well to the GGD model. Similar distributions were observed using the numerical phantom data as well (not shown) however, we selected this example to show the MR signal distributions using actual MRI data.
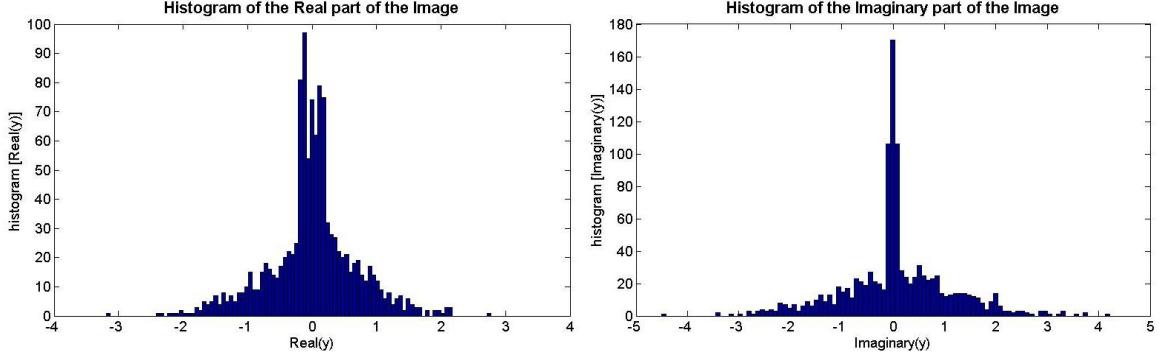
Figure 4-2 A high resolution MR image of the tubes was acquired prior to administration of the contrast agent. The histograms of the real (left) and imaginary (right) parts of this tubes' image are shown here. It can be seen from these images that the distribution (histogram) of the tubes' image can be approximated using GGD model.

Thus, assuming the linear mixture model holds for the MRI data in the complex domain, we modeled the MR image as a sum of a number of functions with GGD distributions. Using an expectation maximization framework (explained in the next section) the parameters of these GGD distributions were found at each iteration and the GGD distribution with the highest membership probability was used to derive the non-linearity in our AC-ICA algorithm. Substituting the parameters (α, β) of the selected GGD distribution in equation 4-9 and using the relationship between the ICA non-linearity and the pdf of the sources, i.e. $\boldsymbol{p}(\mathbf{z}^R, \mathbf{z}^I) = exp\left(-|\boldsymbol{C}(\mathbf{z})|^2\right)$, the ICA non-linearity function was defined as equation 4-10:

$$\boldsymbol{C}(\mathbf{z}) = \left(\frac{\mathbf{z}}{\alpha}\right)^{\beta/2} \tag{4-10}$$

4.2.4 Expectation maximization

We developed an expectation maximization framework to calculate the parameters of the probability distribution of the sources by modeling the probability density function (pdf) of the estimated component as a mixture of a number of GGDs at each iteration. Assuming the pdf of the estimated component $\mathbf{y}$ at each iteration, i.e. $\boldsymbol{f}(\mathbf{y}, \boldsymbol{\Theta})$, is comprised of k random variables with GGD distributions of the form $\boldsymbol{g}(\mathbf{y}; \alpha_k, \beta_k) = \frac{\beta_k}{2\alpha_k \Gamma(1/\beta_k)} exp\left(-\frac{|y|^{\beta_k}}{\alpha_k^{\beta_k}}\right)$, and each GGD contributes to formation of the pdf of $\mathbf{y}$ with a membership probability p_k we have:

72

$$f(\mathbf{y}, \boldsymbol{\Theta}) = \sum_{k=1}^{K} p_k \boldsymbol{g}(\mathbf{y}; \alpha_k, \beta_k) \qquad (4\text{-}11)$$

where $\boldsymbol{\Theta} = [\boldsymbol{\theta_1}, \boldsymbol{\theta_2}, \dots, \boldsymbol{\theta_k}] = [(p_1, \alpha_1, \beta_1), \dots, (p_k, \alpha_k, \beta_k)]$ is the parameter space. $f(\mathbf{y}, \boldsymbol{\Theta})$ is a probability density function, thus:

$$\int_{R^2} f(\mathbf{y}, \boldsymbol{\Theta}) = \int_{R^2} \sum_{k=1}^{K} p_k \boldsymbol{g}(\mathbf{y}; \alpha_k, \beta_k) = \sum_{k=1}^{K} p_k \int_{R^2} \boldsymbol{g}(\mathbf{y}; \alpha_k, \beta_k) = 1 \qquad (4\text{-}12)$$

$\boldsymbol{g}(\mathbf{y}; \alpha_k, \beta_k)$ is also a probability density function, therefore $\int_{R^2} \boldsymbol{g}(\mathbf{y}; \alpha_k, \beta_k) = 1$, and thus:

$$\int_{R^2} f(\mathbf{y}, \boldsymbol{\Theta}) = \sum_{k=1}^{K} p_k = 1 \qquad (4\text{-}13)$$

and since p_k are probabilities they are non-negative ($p_k \geq 0$). The maximum Log-likelihood estimate can be formulated as:

$$\Lambda(\mathbf{y}, \boldsymbol{\Theta}) = log \prod_{n=1}^{N} f(y_n, \boldsymbol{\Theta}) = log \prod_{n=1}^{N} \sum_{k=1}^{K} p_k \boldsymbol{g}(y_n; \alpha_k, \beta_k)$$
$$= \sum_{n=1}^{N} log \sum_{k=1}^{K} p_k \boldsymbol{g}(y_n; \alpha_k, \beta_k) \qquad (4\text{-}14)$$

where N represents the number of samples in $\mathbf{y}$. The maximum likelihood estimation is formulated as:

$$\widehat{\boldsymbol{\Theta}} = \underset{\boldsymbol{\Theta}}{argmax}\{\Lambda(\mathbf{y}, \boldsymbol{\Theta})\} \qquad (4\text{-}15)$$

defining $\boldsymbol{q}(k, n) = p_k \boldsymbol{g}(y_n; \alpha_k, \beta_k)$ results in the following conditional probabilities that are called membership probabilities:

$$\boldsymbol{p}(k|n) = \frac{\boldsymbol{q}(k, n)}{\sum_{m=1}^{K} \boldsymbol{q}(m, n)} \qquad (4\text{-}16)$$

using Jensen's inequalities [159], i.e. $log \sum_{k=1}^{K} b_k \geq \sum_{k=1}^{K} a_k \, log \frac{b_k}{a_k}$, the Log-likelihood at each iteration (i) can be expressed as:

$$\Lambda(\mathbf{y}, \mathbf{\Theta}) = \sum_{n=1}^{N} log \sum_{k=1}^{K} \boldsymbol{q}(k, n)$$

$$\geq \sum_{n=1}^{N} \sum_{k=1}^{K} \boldsymbol{p}^{(i)}(k|n) \, log \, \frac{\boldsymbol{q}(k, n)}{\boldsymbol{p}^{(i)}(k|n)} = \boldsymbol{b}_{(i)}(\mathbf{\Theta}) \qquad (4\text{-}17)$$

where $\boldsymbol{b}_{(i)}(\mathbf{\Theta})$ is the lower bound for the Log-likelihood function. To calculate the maximum Log-likelihood estimator we need to maximize its lower bound, $\boldsymbol{b}_{(i)}(\mathbf{\Theta})$, iteratively.

$$\boldsymbol{b}_{(i)}(\mathbf{\Theta}) = \sum_{n=1}^{N} \sum_{k=1}^{K} \boldsymbol{p}^{(i)}(k|n) \, log \, \boldsymbol{q}(k, n) - \sum_{n=1}^{N} \sum_{k=1}^{K} \boldsymbol{p}^{(i)}(k|n) \, log \, \boldsymbol{p}^{(i)}(k|n) \qquad (4\text{-}18)$$

The second term of the right hand side of equation 4-18 is a constant as it is calculated from the old values. Thus, the maximization problem is simplified to:

$$\widehat{\mathbf{\Theta}} = \max_{\mathbf{\Theta}} \{\boldsymbol{b}_{(i)}(\mathbf{\Theta})\} = \max_{p_k, \alpha_k, \beta_k} \left\{ \sum_{n=1}^{N} \sum_{k=1}^{K} \boldsymbol{p}^{(i)}(k|n) \, log \, \boldsymbol{q}(k, n) \right\} \qquad (4\text{-}19)$$

The probabilities $\boldsymbol{p}(k|n)$ can be calculated at each iteration (i) using equation 4-20:

$$\boldsymbol{p}^{(i)}(k|n) = \frac{p_k^{(i)} \boldsymbol{g}\left(y_n; \alpha_k^{(i)}, \beta_k^{(i)}\right)}{\sum_{m=1}^{K} p_m^{(i)} \boldsymbol{g}\left(y_n; \alpha_m^{(i)}, \beta_m^{(i)}\right)} \qquad \& \qquad \sum_{k=1}^{K} \boldsymbol{p}^{(i)}(k|n) = 1 \qquad (4\text{-}20)$$

Setting the derivative of $\boldsymbol{b}_{(i)}(\mathbf{\Theta})$ with respect to α_k equal to zero we have:

$$\frac{\partial[\boldsymbol{b}(\mathbf{\Theta})]}{\partial \alpha_k} = \sum_{n=1}^{N} \boldsymbol{p}(k|n) \frac{\partial\left[log\left(p_k \boldsymbol{g}(y_n; \alpha_k, \beta_k)\right)\right]}{\partial \alpha_k} = 0 \qquad (4\text{-}21)$$

which results in the following expression for $\alpha_k^{(i)}$ at each iteration:

$$\alpha_k^{(i)} = \left[\frac{\beta_k^{(i)} \sum_{n=1}^{N}\left(\boldsymbol{p}^{(i)}(k|n)|y_n|^{\beta_k^{(i)}}\right)}{N} \right]^{1/\beta_k^{(i)}} \qquad (4\text{-}22)$$

Setting the derivative of $\boldsymbol{b}_{(i)}(\mathbf{\Theta})$ with respect to β_k equal to zero we have:

$$\frac{\partial[\boldsymbol{b}(\mathbf{\Theta})]}{\partial \beta_k} = \sum_{n=1}^{N} \boldsymbol{p}(k|n) \frac{\partial\left[log\left(p_k \boldsymbol{g}(y_n; \alpha_k, \beta_k)\right)\right]}{\partial \beta_k} = 0 \qquad (4\text{-}23)$$

this equation results in equation 4-24 to calculate $\beta_k^{(i)}$ at each iteration:

$$\frac{1}{\beta_k^{(i)}}\left(1 + \frac{1}{\beta_k^{(i)}}\psi\left(\frac{1}{\beta_k^{(i)}}\right)\right)\sum_{n=1}^{N}\boldsymbol{p}^{(i)}(k|n) - \sum_{n=1}^{N}\boldsymbol{p}^{(i)}(k|n)\left(\frac{|y_n|}{\alpha_k^{(i)}}\right)^{\beta_k^{(i)}} log\left(\frac{|y_n|}{\alpha_k^{(i)}}\right) = 0 \qquad (4\text{-}24)$$

74

where $\boldsymbol{\psi}(\mathbf{x}) = d\left(log(\boldsymbol{\Gamma}(\mathbf{x}))\right)/d\mathbf{x}$, is the polygamma function. This equation can be solved using any optimization algorithm. We used the fzero function of MATLAB (The MathWorks Inc., Natick, USA) software to find the value of $\beta_k^{(i)}$ at each iteration. These three equations (equation 4-20, equation 4-22 and equation 4-24) were solved at each iteration and the parameter set $\left(p_{optimum}, \alpha_{optimum}, \beta_{optimum}\right)$ were calculated for each GGD distribution. The GGD that had the highest membership probability ($p_{optimum}$) was selected as the pdf of the source and its parameters were used in the ICA algorithm.

4.2.5 AC-ICA implementation and VIF identification

Dimensionality reduction and Whitening were performed as pre-processing steps in order to reduce noise and make the signal zero mean and unit variance (similar to the Mag-ICA algorithm). Singular value decomposition (SVD) was performed on the dataset and the significant eigenvalues (the eigenvalues that were bigger than 0.1% of the largest eigenvalue) that accounted for 99.9% of the information in the dataset were kept. AC-ICA was applied to the dataset after dimensionality reduction and Whitening, and the number of extracted independent components (IC) was equal to the number of significant eigenvalues which were kept at the dimensionality reduction step. The intravascular components were selected heuristically such that the curves that had a uniform pre-contrast uptake phase, an uptake phase in which the intensity increased rapidly and a washout phase in which the intensity dropped to less than 60% of the peak value were selected as the intravascular components.

4.3 AC-ICA separation results

The AC-ICA algorithm for separating the intravascular component was first applied to the numerical phantom (described in chapter 2) to separate the signal of the tubes, which represented the intravascular space, from the simulated DCE-MR images of the phantom.

4.3.1 Numerical phantom

The adaptive complex ICA (AC-ICA) for intravascular time-intensity curve calculation was applied to all simulated datasets (four different resolutions) and the signal from inside the tubes (intravascular signal) was extracted. Dimensionality reduction was performed on each dataset through singular value decomposition (SVD) of the covariance matrix of the data. The number of the eigenvalues that were kept for analysis ranged between 8 and 15 which is the

maximum number of IC's that could be estimated. The data was then Whitened to make it zero mean and unit variance. In all cases, all IC's were estimated and the IC (or ICs) that corresponded to the tubes' signal was selected using the heuristic criterion. In brief the IC that had a uniform pre-contrast uptake followed by a rapid contrast uptake and also a rapid washout of the contrast agent to less than 60% of the peak signal intensity within 3 [min] of injection of the bolus was selected as the tubes' signal.

In Figure 4-3 the results of applying AC-ICA to the simulated complex-valued DCE-MRI data are illustrated (compare to Figure 3-2 at page 54 which showed these results for Mag-ICA algorithm). The extracted IC images of tubes for all 4 resolutions are shown in Figure 4-3a-d. The time-intensity curves of the tubes for all four simulated datasets are shown in Figure 4-3e. These curves represent the average signal intensity over time of all the voxels that are separated by ICA as the intravascular space (tubes). Figure 4-3e also shows the actual intravascular time-intensity curves as well as the raw data curve calculated by averaging the signal across the raw MRI images. The time-intensity curves are normalized with respect to their maximum and their pre-contrast signal intensities are set to zero to enable comparison.
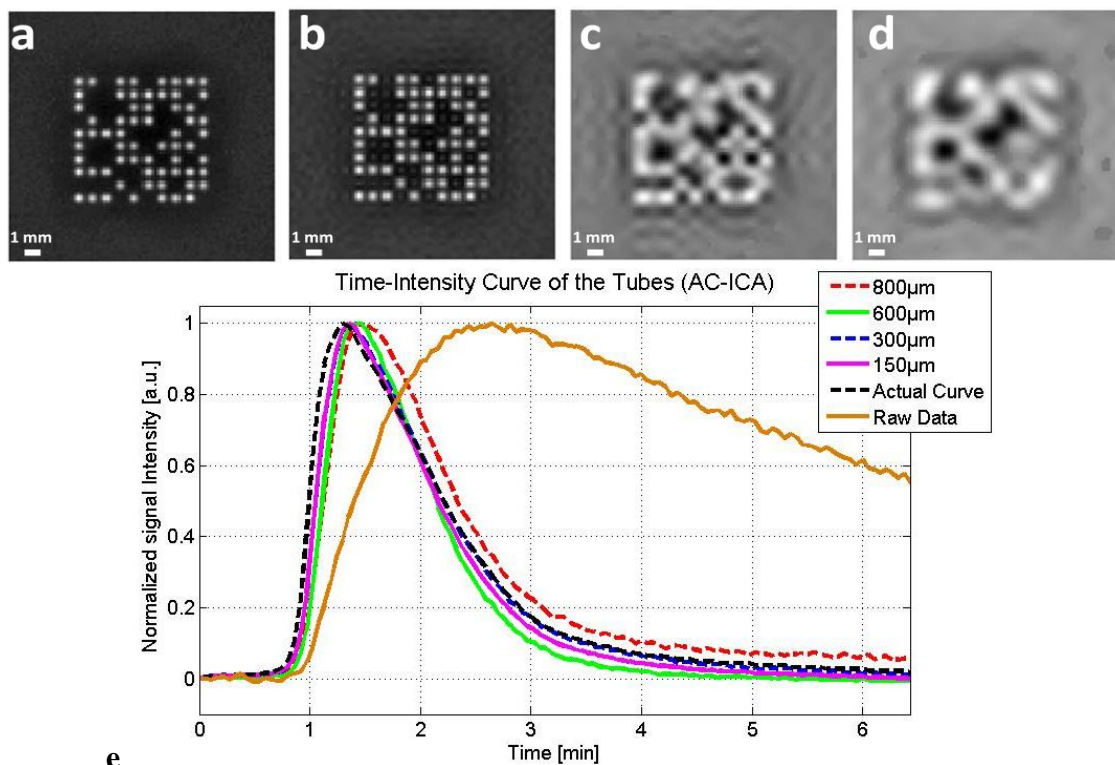
Figure 4-3 The separated tubes' image and the time-intensity curve of the tubes calculated using AC-ICA for the four simulated DCE-MRI datasets. Tubes images for datasets with in-plane resolutions of a) 150 [μm], b) 300 [μm], c) 600 [μm], d) 800 [μm]. e) Calculated time-intensity curves of the tubes corresponding to the 4 simulated datasets, the actual time-intensity curve of the tubes (Actual Curve) and the curve corresponding to the mean across the entire raw (not analyzed) images over time (Raw Data).

The IC images extracted using AC-ICA had complex values and thus each voxel is represented with a two dimensional vector (magnitude and phase) while each voxel in the images shown in Figure 4-3a-d is represented with a one dimensional value (image signal intensity). This conversion was required for visualization purposes and was performed by assigning negative sign to magnitude of the values of the voxels with $-\pi/2 \leq$ phase $< \pi/2$ and assigning positive sign to magnitude of the values of the voxel with phase $\geq \pi/2$ or phase $< -\pi/2$. This method of visualizing the images provides consistent results with the Mag-ICA analysis where we had both negative and positive signal intensity values.

For each in-plane resolution, 10 DCE-MRI data sets of the phantom were simulated with SNR=20 and the AC-ICA algorithm was applied to all datasets. Table 4-1 reports the root mean square error (RMSE) between the estimated time-intensity curves of the tubes obtained using AC-ICA algorithm and the actual curve for all 4 in-plane resolutions. Table 4-1 also reports the correlation coefficient between the estimated and actual time-intensity curves of the tubes for AC-ICA algorithm. These values are calculated using the results of applying Mag-ICA to the 10 different implementations of the phantom for each resolution (compare to Table 3-1 at page 55 which reported these results for Mag-ICA algorithm).

Table 4-1 The root mean square error (RMSE) and correlation coefficient between the estimated tubes' time-intensity curves and the actual curve for 4 resolutions in numerical phantom for AC-ICA algorithm. These values were calculated using the results of applying Mag-ICA to the 10 different implementations of the phantom for each resolution (these values were calculated after removing pre-contrast concentrations and normalizing the curves).

In-plane Resolution	150µm	300µm	600µm	800µm
	Root Mean Square Error (RMSE)			
AC- ICA	0.04± 0.01	0.04±0.01	0.07±0.01	0.08±0.01
	Correlation Coefficient			
AC-ICA	0.99±0.001	0.99±0.001	0.97±0.01	0.96±0.01

4.3.2 Physical Phantom

The AC-ICA algorithm was also applied to DCE-MRI images of the physical tissue-mimicking phantom. Similar to the simulation study, dimensionality reduction was performed first where eigenvalues that were larger that 0.1% of the largest eigenvalue were kept and the data was Whitened. The phantom data was reconstructed in 5 different in-plane resolutions and the AC-ICA algorithm was applied to all 5 datasets. Figure 4-4 shows the results of applying AC-ICA algorithm to the DCE-MRI data of the physical phantom (compare to Figure 3-4 at page 57 which showed these results for Mag-ICA algorithm). The IC images corresponding to the tubes' signal of the 5 datasets are shown in Figure 4-4a-e. The time-intensity curves of the 5 datasets as well as the actual time-intensity curve of the tubes that was measured at the inflow line of the phantom, the time-intensity curve at the outflow line and the raw data curve calculated by averaging the signal across the raw MRI images over time are shown in Figure 4-4f. The baseline values of the enhancement curves of all datasets were set to zero and they were normalized with respect to their maximum values.
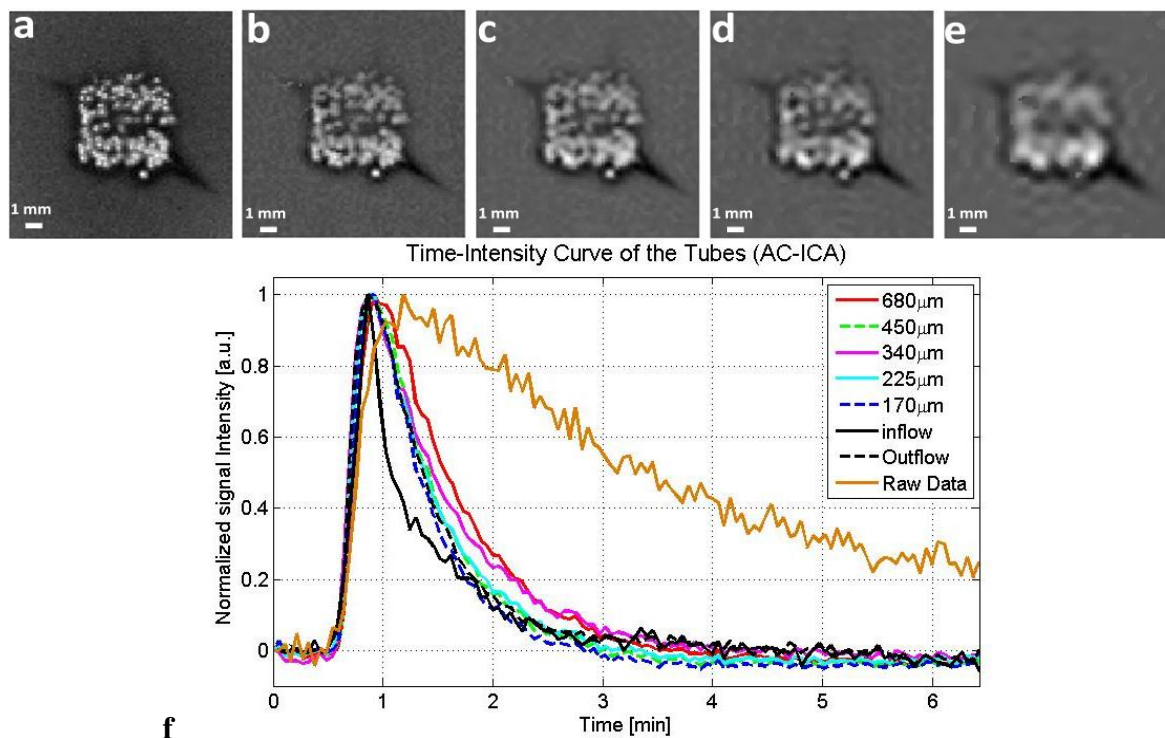
Figure 4-4 The separated tubes image and the intravascular time-intensity curve of the tubes calculated using AC-ICA for each of the five DCE-MRI datasets of the physical tissue-mimicking phantom. Tubes' images for datasets with in-plane resolutions of a) 170 [μm], b) 225 [μm], c) 340 [μm], d) 450 [μm], and e) 680 [μm]. e) Calculated time-intensity curves of the tubes corresponding to the 5 datasets, the actual time-intensity curve of the tubes (inflow line), the curve of the tubes at the outflow line, and the curve corresponding to mean across the raw (not analyzed) MR images over time (Raw Data).

Two physical phantoms were built and DCE-MRI imaging was performed on both phantoms to assess the reproducibility of the results for the intravascular time-intensity curve calculation algorithms. Table 4-2 reports the root mean square error (RMSE) between the estimated and the actual time-intensity curves of the tubes (inflow) for all 5 datasets of both phantoms. This table also reports the correlation coefficient between the estimated and actual time-intensity curves of the tubes for AC-ICA algorithm in all 5 in-plane resolutions (compare to Table 3-2 at page 58 which reported these results for Mag-ICA algorithm).

Table 4-2 The root mean square error (RMSE) and the correlation coefficient between the estimated and actual time-intensity curves of the tubes (inflow) for all 5 datasets of both physical phantoms using AC-ICA algorithm (RMSE and correlation coefficients are calculated after setting the baseline values of the curves to zero and normalizing them).

In-plane Resolution	170μm	225μm	340μm	450μm	680μm
	Root Mean Square Error (RMSE)				
AC- ICA	0.07±0.01	0.09±0.02	0.08±0.03	0.08±0.01	0.11±0.03
	Correlation Coefficient				
AC-ICA	0.97±0.004	0.96±0.02	0.97±0.01	0.97±0.02	0.95±0.03

4.4 Discussions

A fundamental step in PK modeling is determining the intravascular contrast agent concentration which is usually approximated using an arterial input function (AIF). In this thesis we developed two ICA-based methods for identifying and separating the intravascular component of the tissue of interest in DCE-MRI. The previous chapter presented the results of applying the Mag-ICA algorithm to DCE-MRI data. Although the output of MR imaging is complex-valued, only the magnitude of the data was used in Mag-ICA algorithm (as is common in most DCE-MRI studies) and the phase information was not utilized. This introduced a fundamental challenge in ICA analysis as the linear mixture assumption of ICA was violated. This problem was addressed by using short echo time (TE) which minimizes intra-voxel de-phasing. The Mag-ICA algorithm also used a fixed non-linearity function in its ICA implementation. Such a separation algorithm does not take into account the variability in

the distribution of tissue vasculature. The separated intravascular image and time-intensity curves were evaluated using actual time-intensity curves in numerical and physical phantoms as well as using intravascular contrast ultrasound measurements in *in vivo* animal models.

To address these shortcomings of Mag-ICA algorithm, an adaptive complex ICA (AC-ICA) algorithm was developed that used the complex-valued MRI data and also used an adaptive non-linearity function in its ICA implementation. The adaptive non-linearity function was determined by assuming the probability distribution of MRI data takes the form of a mixture of generalized Gaussian distributions (GGD) whose parameters were estimated using an expectation maximization (EM) approach at each iteration.

The AC-ICA algorithm was applied to the DCE-MRI data of the simulated and physical tissue-mimicking phantoms and the tubes' time-intensity signal was estimated. Comparing these results to the results that were presented in the previous chapter for Mag-ICA algorithm demonstrate the superior performance of the AC-ICA algorithm. Both physical and simulation data were reconstructed in different resolutions to assess the robustness of the algorithm and its capability in separating signal of the tubes in low resolution data that are more common in clinical practice.

Comparing the separation results of simulation study presented in Figure 4-3 and Table 4-1 for AC-ICA with those of Mag-ICA in Figure 3-2 and Table 3-1 both AC-ICA and Mag-ICA algorithms were capable of separating time-intensity curve of the tubes with high accuracy for high resolution data in both spatial and temporal domains. However, as the voxel size increased (lower resolution), the AC-ICA demonstrated higher accuracy and robustness compared to Mag-ICA in dealing with datasets with a wide range of in-plane resolutions. There were small differences between the time-intensity curves of the tubes calculated using AC-ICA for different resolutions while Mag-ICA curves changed significantly and its time-intensity curves were not good for the lower resolutions. Note that in lower resolutions although the tubes could not be visualized in the spatial domain, however; their time-intensity curves were calculated with good accuracy using AC-ICA algorithm.

Similar results were obtained in the DCE-MRI data of the physical phantom as shown in Figure 4-4, Figure 3-4 and also reported in Table 4-2 and Table 3-2. The tubes were separated accurately in both spatial and temporal domains for the high resolution data using both Mag-ICA and AC-ICA algorithms. As the pixel size increased, it became more difficult to visualize the tube in the IC images such that in the two lowest resolutions it was impossible

to see them separately from the leakage. However, the time-intensity curve of the tubes was estimated with high accuracy for all resolutions in AC-ICA algorithm. Similar to the simulation studies, the AC-ICA demonstrated better accuracy in dealing with lower resolution data and there were smaller differences between time-intensity curves of the tubes at varying resolutions compared to the Mag-ICA algorithm.

There was an aura in the physical phantom images outside of the tubes which was due to a fabrication artifact. A few of the tubes were broken during the phantom construction process and the contrast agent was capable of leaving these broken tubes more easily. The results show that this aura was smaller in the tubes image of the AC-ICA algorithm (particularly in the high-resolution images) compared to the Mag-ICA results which shows that AC-ICA is capable of separating the intravascular space more accurately. There are two reasons for superior performance of AC-ICA:

1-   The ICA non-linearity function was derived at every iteration to match the probability distribution of the tubes' signal

2-   Unlike the Mag-ICA algorithm, the linear mixture assumption of ICA was not violated in AC-ICA and thus intra-voxel de-phasing (spins inside each voxel are not necessarily in-phase) and partial volume effect did not play as significant role as they did in Mag-ICA.

Combination of both of the above mentioned changes led to better performance of the AC-ICA algorithm. However, the intra-voxel de-phasing was minimized in the Mag-ICA algorithm by using a short TE and thus, the use of the adaptive non-linearity function had the most significant effect in the results.

In this chapter and also chapter 3, the MR signal intensity was used to identify and separate the intravascular component and assess the performance of the AC-ICA and Mag-ICA algorithms. However, PK analysis requires the intravascular time-intensity signal to be converted into contrast agent concentration. As mentioned in chapter 3, this is not a trivial step as ICA suffers from an intrinsic arbitrary scaling problem and also since it is a data-driven algorithm it might split the intravascular component into several components. The steps required for generating a single intravascular signal from the potentially multiple intravascular ICs are explained in chapter 5, where the ICA-based VIF will be applied to

DCE-MRI sequences of prostate cancer patients. The steps required for conversion of this intravascular MR signal intensity to contrast agent concentration are provided in appendix III.

4.5 Summary

This chapter presented the AC-ICA algorithm and results of applying the AC-ICA algorithm to the numerical and physical tissue-mimicking phantoms and compared them to the separation results achieved by Mag-ICA algorithm (chapter 3). The results presented in these two chapters (chapter 3 and chapter 4) showed that although the tubes were not visible in the IC images of low resolution datasets (in both simulation and experiment), the intravascular time-intensity curves in low resolution datasets were very close to the high resolution ones particularly when using AC-ICA algorithm. This demonstrates that ICA-based calculation of the intravascular time-intensity curve has the potential to be used in clinical studies, where the resolution of DCE-MRI data is very low. The AC-ICA algorithm provided more accurate results compared to Mag-ICA, which suggests that complex-valued (magnitude and phase) DCE-MRI data should be used to calculate the intravascular time-intensity curve in the tumor. This could lead to more accurate PK analysis and better understanding of the tumor response to therapy.

Chapter 5 applies the VIF of the AC-ICA algorithm to DCE-MRI data of a cohort of 27 prostate cancer patients (28 datasets with one patient being imaged twice). The separation results presented so far were on the MRI signal intensity while PK analysis requires these results to be converted into contrast agent concentration. This step is explained in detail in the next chapter and appendix III, and the PK parameters achieved using the proposed VIF calculation algorithms will be compared to the PK parameters calculated using the contrast agent concentration over time in the femoral as the AIF.

Chapter 5

Prostate Cancer Assessment

The previous chapter introduced the AC-ICA algorithm for separating the intravascular component in DCE-MRI. It also presented the results of applying the AC-ICA algorithm to the numerical and physical tissue-mimicking phantoms and compared its separation result to those of the Mag-ICA algorithm (presented in chapter 3). Comparing the results of chapters 3 and 4 demonstrated that the AC-ICA algorithm provides a better separation of the intravascular component and hence is used in this chapter for PK analysis.

Chapter 5 presents the steps required for combining the intravascular ICs (in case more than one IC is identified as intravascular) to generate a single intravascular signal and converting this signal into contrast agent concentration to generate the VIF. Chapter 5 also applies the VIF separation algorithm to DCE-MR images of a cohort of 27 prostate cancer patients (28 datasets with one patient being imaged twice) and performs PK analysis on each dataset. These PK parameters are then compared to PK parameters calculated using the signal of a large artery (femoral artery) as the AIF. This chapter also explains the need for normalization of the VIF and AIF curves to enable comparison between the PK parameters of two methods. The final section of chapter 5 examines the performance of the VIF-based PK parameters when low temporal resolution DCE-MR images are acquired and compares them to AIF-based parameters.

5.1 Vascular Input Function

Identifying and separating the signal of the intravascular space and calculating the vascular input function (VIF) includes the following steps:

1-   Applying the ICA-based separation algorithms to the DCE-MRI data

2-   Converting the intravascular ICs into contrast agent concentration

3-   Normalizing the concentration-time curve to minimize errors due to manual ROI selection and enable comparison of the parameters of different methods.

Applying ICA-based algorithms to the DCE-MRI data and separating the intravascular component (step 1) was explained in the previous chapters and in this chapter steps 2 and 3 will be explained in detail.

5.1.1 Converting ICA-based VIF to Concentration

The intravascular image and its corresponding time-intensity curve that are calculated using ICA-based algorithms have to be converted into contrast agent concentration before being used in PK analysis. The steps required to convert DCE-MRI signal acquired by spoiled gradient recalled (SPGR) pulse sequence are explained in detail in appendix III. As explained in this appendix, in order to convert the signal intensity of a voxel at time $t = t_0$ into its contrast agent concentration, both the pre-contrast signal intensity and the MR signal intensity at $t = t_0$ are required. This section provides details of preparing the AC-ICA results for conversion into contrast agent concentration.

As ICA is a data-driven algorithm which does not make any assumption about the physiology of the data it is processing, some structures, e.g. intravascular space, might split into several ICs. These ICs have to be first combined to represent the entire intravascular signal. We can rewrite equation 4-1 in expanded form as follows:

$$
\begin{bmatrix} \mathbf{z}_0 \\ \vdots \\ \mathbf{z}_{N-1} \end{bmatrix} = \begin{bmatrix} \mathbf{a}_0, \dots, \mathbf{a}_{IV}{}^{(1)} \dots, \mathbf{a}_{IV}{}^{(K)}, \dots, \mathbf{a}_{M-1} \end{bmatrix} \begin{bmatrix} \mathbf{s}_0 \\ \vdots \\ \mathbf{s}_{IV}{}^{(1)} \\ \vdots \\ \mathbf{s}_{IV}{}^{(K)} \\ \vdots \\ \mathbf{s}_{M-1} \end{bmatrix} \tag{5-1}
$$

where $\mathbf{a}_i$ is a column of mixing matrix $\mathbf{A}$, and K is the number of ICs that are identified as intravascular. The time series data corresponding to the intravascular signal, $\mathbf{Z}_{IV}$, can be written as:

$$
\mathbf{Z}_{IV} = \begin{bmatrix} \mathbf{z}_{IV,0}, \mathbf{z}_{IV,2}, \dots, \mathbf{z}_{IV,N-1} \end{bmatrix}^{T} = \mathbf{a}_{IV}{}^{(1)}\mathbf{s}_{IV}{}^{(1)} + \dots + \mathbf{a}_{IV}{}^{(K)}\mathbf{s}_{IV}{}^{(K)} \tag{5-2}
$$

where $\mathbf{z}_{IV,t_0}$ is the intravascular portion of the DCE-MRI dataset at time t_0 ($t = t_0$). The change in the intravascular signal due to contrast agent arrival and passage through the intravascular space between $t = 0$ and $t = t_0$ is:

$$\Delta\mathbf{z}_{IV,t_0} = \mathbf{z}_{IV,t_0} - \mathbf{z}_{IV,0} \tag{5-3}$$

by adding $\Delta\mathbf{z}_{IV,t_0}$ to the DCE-MRI image corresponding to $t = 0$ (which is $\mathbf{z}_0$) we could generate a DCE-MRI time-series data in which the only enhancement is due to the contrast agent arrival and passage through the intravascular space. The signal intensity is the magnitude of the complex-valued MRI signal and thus we have:

$$\mathbf{SI}_{IV}(0) = |\mathbf{z}_0|$$

$$\mathbf{SI}_{IV}(t_0) = \left|\mathbf{z}_0 + \Delta\mathbf{z}_{IV,t_0}\right| \tag{5-4}$$

Once $\mathbf{SI}_{IV}(0)$ and $\mathbf{SI}_{IV}(t_0)$ are calculated, the intravascular concentration is calculated as explained in appendix III.

5.1.2 Normalization of VIF

Most studies analyze the relative values of PK parameters (particularly K^{trans}), which is useful but limits the application of PK analysis. Absolute values of the PK parameters enable better understanding of treatment response or monitoring the progression of the disease, e.g. in active surveillance patients. There might also be a relationship between tumor grade and different PK parameters which cannot be studied in a patient population if the absolute values of parameters are not known. However, due to the arbitrary scaling of the VIF (or AIF) between subjects, absolute values cannot be obtained. The scaling of the VIF (or AIF) varies depending on the manual ROI that is drawn around a large artery or the ROI that is being used for VIF (or AIF) estimation. It is common to normalize the VIF (or AIF) by dividing it by the number of voxels in the ROI which is operator-dependant and varies between measurements. For instance if the manually identified ROI is close to the vessel wall (large partial volume effect) in one subject and close to the center of the artery (smaller partial volume effect) in another patient, the AIFs would have different scaling which introduces variation in the calculated PK parameters. Such normalization becomes more problematic when VIFs are being used as the region used for ICA analysis may vary significantly.

Although it is not practical to calculate the absolute scaling of the VIF (or AIF), if they were scaled similarly, the absolute values of their corresponding PK parameters could be compared between subjects. We propose normalizing the VIF (or AIF) with respect to their area under the curve (AUC) as the total blood that passes through the tissue for a specific imaging interval (between the arrival of the contrast agent and the time point of the last frame), is independent of AIF or VIF that is being used. Appendix IV shows that if two VIFs satisfy the model equations for a specific tissue type, their areas under the curve (AUC) have to be equal. Such normalization in addition to allowing comparison between AIF-based and VIF-based PK parameters, provides more consistent PK results inter-subject if the dose per kilogram-of-body-weight of injected contrast agent is kept constant between patients.

5.2 VIF calculation: Numerical Phantom

The AC-ICA algorithm was applied to the DCE-MR images of the numerical phantom and the intravascular ICs were identified heuristically in chapter 4. These MR images were then converted into contrast agent concentration using the standard approach for SPGR images explained in section 5.1 and appendix III, and the results are shown in Figure 5-1 for different resolutions. Figure 5-1a shows the VIF curves calculated for each resolution, averaged over 10 different simulated datasets for that resolution. As can be seen in this figure the amplitude of the curves change at different resolutions and there is underestimation of the contrast agent concentration for low resolution datasets (due to partial volume effect). This figure also shows underestimation of the VIF curve for the highest resolution dataset which is probably due to the fact that AC-ICA was capable of separating the tube walls from the center of the tubes and only the component corresponding to the center of the tubes was used as the VIF.
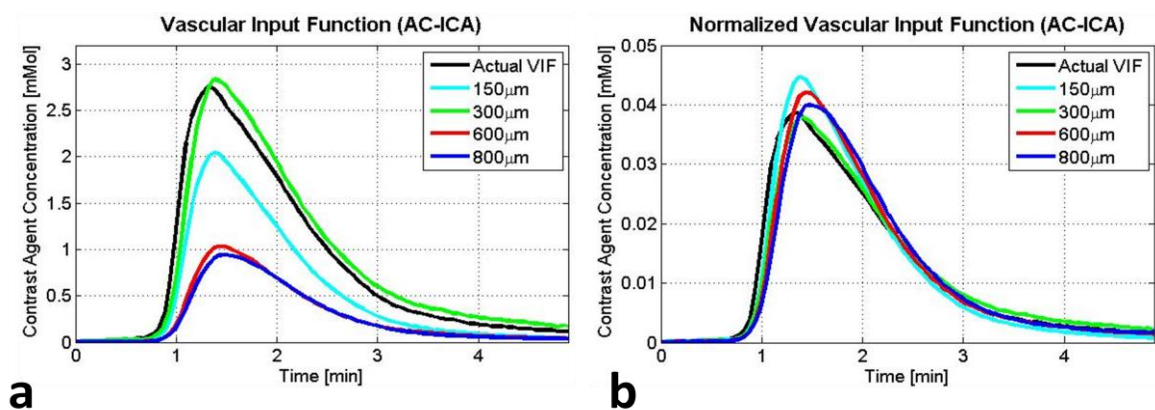
Figure 5-1 a) The VIF curves (contrast agent concentration in tubes) for the simulated DCE-MRI dataset with the 4 different resolutions (each curve is the average of VIF calculation for 10 simulated phantoms), b) the normalized VIF curves calculated for numerical phantom at different resolutions.

As can be seen in this figure, there is high variance between curves and partial volume effect is being handled differently among these datasets as the in-plane resolution changes, which makes them difficult to be used as the VIF in subsequent PK analyses. In order to address this problem a normalization procedure was introduced in previous section in which the VIF curve was normalized with respect to its area under the curve (AUC). The VIF curves (shown in Figure 5-1a) after applying the normalization step are shown in Figure 5-1b. As can be seen the average VIF curves for each resolution after normalization have the same amplitude and are very similar (Figure 5-1b). This demonstrates the reproducibility of the calculated VIF (normalized) in different resolutions particularly in low resolution datasets that are commonly encountered in clinical studies.

5.3 VIF calculation: Prostate

The field of view (FOV) in prostate DCE-MRI contains several structures (e.g. prostate, rectum, bladder, femoral and iliac arteries, etc.) and each structure has its own bolus passage profile (different arrival times, different times to peak, etc.). Thus, applying ICA to the full DCE-MRI field of view separates these structures and their corresponding vascular input function. Such a separation results in an IC corresponding to the VIF of the prostate tissue, an IC corresponding to the AIF measured at the arteries and several other ICs corresponding to other structures with significant vascular signal. Figure 5-2 shows the results of applying AC-ICA to a sample slice of the DCE-MRI of one of the prostate cancer patients. The figure shows the full DCE-MRI field of view, and the ICs corresponding to the arteries and prostate gland separated using AC-ICA algorithm. Figure 5-2d shows the contrast agent concentration over time for the femoral artery (shown with blue arrow) using the AC-ICA results and using manual AIF calculation. In order to generate these curves an ROI was first drawn around the femoral artery and was used in calculating both curves. For manual AIF calculation the full DCE-MRI of the prostate was first converted into contrast agent concentration and then the concentration of the ROI over time was calculated. For the ICA-based AIF, the AC-ICA algorithm was first applied to the full field of view of prostate DCE-MRI (IC image of arteries is shown Figure 5-2b). Then, the signal enhancement of the IC corresponding to the arteries was converted into contrast agent concentration and the concentration of the femoral artery ROI was calculated over time and is shown in Figure 5-2d. As expected, in presence of an artery the AC-ICA algorithm provided an AIF curve very close to the one that would be measured using manual techniques that are currently used (this example was given to illustrate the performance of the proposed algorithm when there is an artery in FOV).
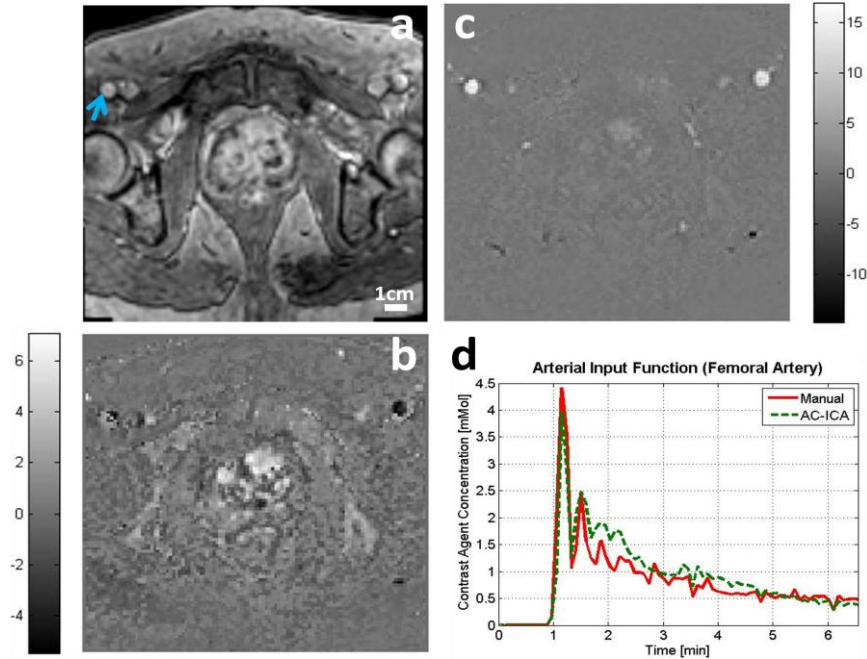
Figure 5-2 a) The full DCE-MRI field of view for a sample dataset. The independent components corresponding to b) the prostate vasculature, and c) the major arteries, identified by the AC-ICA algorithm (the color bars in b and c show the signal intensity of the separated IC and have arbitrary units). d) The AIF calculated using the AC-ICA results as well as manual AIF measured at the femoral artery. For manual AIF calculation the full DCE-MRI data was first converted into contrast agent concentration and then the concentration of the ROI over time was calculated. For the ICA-based AIF, the AC-ICA algorithm was first applied to the full field of view of prostate DCE-MRI. Then, the signal enhancement of the IC corresponding to the arteries was converted into contrast agent concentration and the concentration of the femoral artery ROI was calculated over time.

However, using the full FOV for AC-ICA is time consuming and also affects the prostate vasculature pdf estimation as there is a large number of voxels with zero or near zero concentrations in its IC image. Using such a large FOV might affect ICA separation performance as the averaging steps are on a very large FOV and thus small changes in the signal might be ignored. In order to achieve more accurate results and fast implementation a rectangular region of interest was selected around the prostate tissue and AC-ICA was applied to this region rather than the entire prostate gland (yellow box in Figure 5-3a).

Each prostate DCE-MRI dataset contained 20 slices. The slices in which the prostate was visible were first identified and a rectangular region of interest was selected around the prostate gland. The AC-ICA algorithm was then applied to each individual slice and the intravascular component was separated. The separated intravascular component for a sample prostate dataset in spatial and temporal domains is shown in Figure 5-3b-c

88
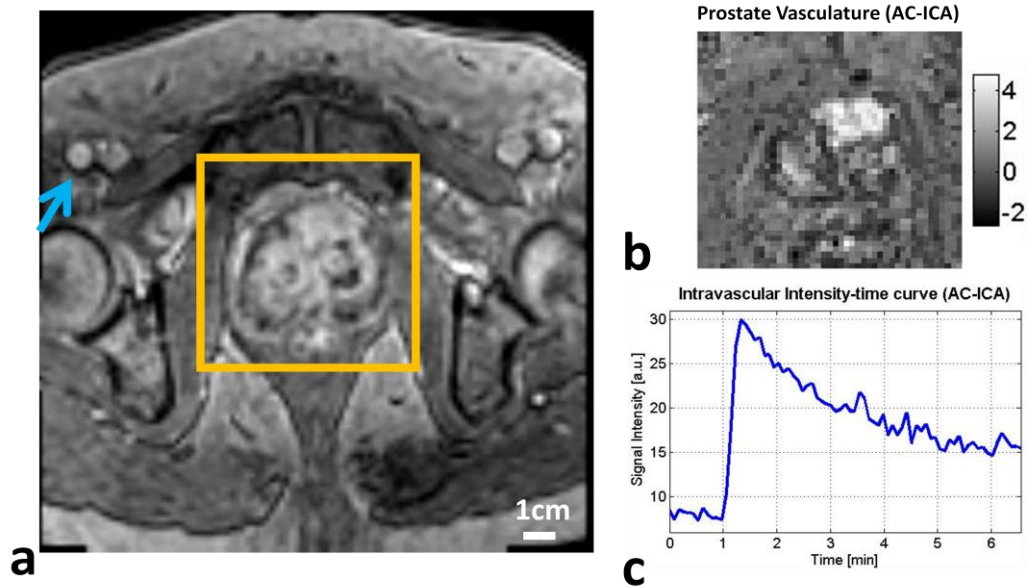
Figure 5-3 a) The full DCE-MRI field of view for a sample dataset. The independent component corresponding to the prostate vasculature separated by the AC-ICA algorithm in b) spatial domain (color-bar shows the average signal intensity of the separated IC spatially which has an arbitrary unit due to scaling ambiguity of ICA), and c) temporal domain.

Once the intravascular component was identified and separated, the signal intensity in each voxel of the intravascular DCE-MRI sequence (generated by removing the contrast agent enhancement in the extravascular space), was converted into contrast agent concentration. Once each intravascular frame was converted into contrast agent concentration it was averaged over the entire image (its total contrast agent concentration was divided by the number of its voxels) to generate the VIF curve. The results of this conversion (for the slice shown in Figure 5-3) in temporal domain (representing the VIF curve) and in spatial domain (representing the prostate vasculature) are shown in Figure 5-4.
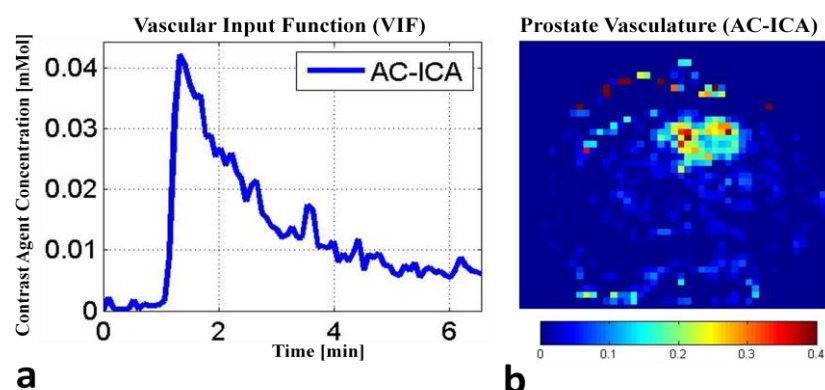
Figure 5-4 a) The VIF curve generated by averaging the contrast agent concentration of each frame in the intravascular space, b) the intravascular space in spatial domain showing the intravascular contrast agent concentration in every voxel of the prostate tissue (color-bar shows the fraction of each voxel that is intravascular).

89

The VIF curves for 6 sample patients (one slice per patient) are shown in Figure 5-5 (first column). The scale of such a VIF curve depends on the size of the ROI that was initially selected for ICA analysis and thus is operator-dependent. Moreover, the region that the prostate occupies in each slice is highly variable and thus the size of the ICA region can change significantly between slices and also between different subjects. These issues make the calculated PK parameters highly dependent on the manually selected ROI.

As explained in the normalization section 5.1, if two VIFs satisfy the governing equations of the two-compartment Tofts-Kety model, their AUC have to be equal. In order to resolve the issue of VIF dependence on the ROI and also the problems that were explained in the previous section (section 5.2) which demonstrated the dependence of the VIF on the imaging resolution, the VIF was normalized with its AUC as shown in Figure 5-5 (third column).

In the prostate DCE-MRI study we also measured an AIF for each dataset by selecting a region close to the center of the femoral artery that was visible in the images (blue arrow in Figure 5-3a) and converted its signal intensity into contrast agent concentration over time (second column in Figure 5-5). The AIF was measured on the middle slice of the 3D MRI volume to minimize the inflow effects. The effect of the manually selected ROI in artery is not as significant as the ICA-based VIFs. However, the voxels that were closer to the artery wall had lower signal intensity (due to partial volume effect) compared to the voxels at the center. Thus, if the ROI in the artery was selected close to the vessel wall, its AIF would have lower amplitude compared to the AIF measured using a ROI close to the center of the vessel. Thus, we normalized the AIF with respect to its AUC (third column in Figure 5-5). Such normalization of the AIF and VIF curves, in addition to addressing the above mentioned problems of each method, enabled comparing the PK parameters obtained using AIF with the parameters obtained using VIF.

The rationale behind comparing the PK parameters calculated using VIF and AIF was that both curves were assumed to satisfy the governing equation of the two-compartmental exchange model (Tofts-Kety models). Thus, as shown in normalization section, these curves had to have equal AUC and the differences in their PK parameters (Results section) arised from their error in estimating the actual VIF of each voxel. Note that the PK parameters of the two curves (AIF and VIF) could not be compared before normalization as the AUC of VIFs that are shown in first column of Figure 5-5 were much smaller than the AUC of the AIFs shown in second column of Figure 5-5 and thus their PK parameters had different

scaling. Even while comparing the PK parameters calculated for the same VIF (or VIF) calculation method, the PK parameters of different patients had larger variation if these curves were not normalized as reported in Table 5-1 and Table 5-3.
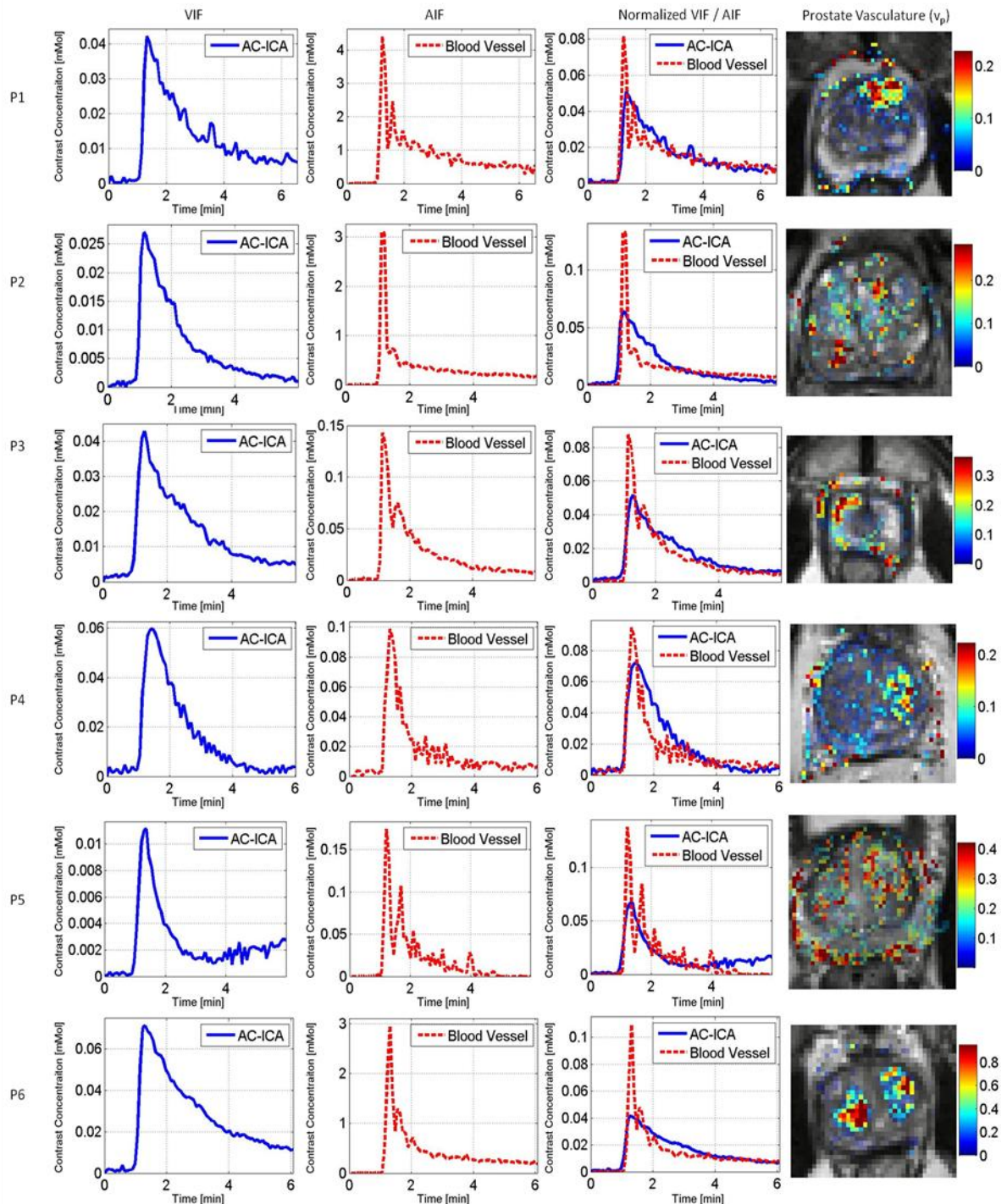
Figure 5-5 The VIF (first column) and AIF (second column) before normalization for a sample slice of 6 patients. The corresponding normalized VIF and normalized AIF (third column) and the vascular map corresponding of the VIF curves (fourth column).

5.4 PK analysis results

The Tofts-Kety model and the extended Tofts-Kety model are the most commonly used PK models in tumor characterization [76]–[80] and thus in this thesis these two models were used. As mentioned in chapter 1, the governing equations of the Tofts-Kety model which is the weakly vascularized limit of a two compartment exchange model are:

$$c_t(t) = v_e c_e(t)$$

$$v_e \frac{dc_e}{dt}(t) = K^{trans}\big(c_a(t) - c_e(t)\big)$$

(5-5)

and the governing equations of the extended Tofts-Kety model which is the highly perfused limit of the two compartment exchange model are:

$$c_t(t) = v_p c_p(t) + v_e c_e(t)$$

$$v_e \frac{dc_e}{dt}(t) = K^{trans}\big(c_a(t) - c_e(t)\big)$$

(5-6)

To solve these equations and calculate the PK parameters, the term $c_t(t)$ which is the tissue concentration was available from the DCE-MR images of the tissue and the term $c_p(t)$ was provided using a VIF (or AIF) calculation method. In extended Tofts-Kety model it is assumed the plasma concentration (c_p) is equal to the arterial concentration (c_a) as it is entering the tissue ($c_p = c_a$). Pharmacokinetic parameters were calculated for each voxel of the prostate gland in all patients, via solving the Tofts-Kety model equations and extended Tofts-Kety model equations using both the AC-ICA based VIF and AIF from the femoral artery. The analysis for extended Tofts-Kety model was performed in two different methods:

1- Using the prostate vasculature map that was estimated by AC-ICA algorithm as the v_p parameter and subtracting the $v_p c_p(t)$ term from the DCE-MRI data and then using the Tofts-Kety model and the AC-ICA based VIF to calculate the remaining two parameters (K^{trans} and v_e).

2- Using the ICA-based VIF and solving the model parameters for all 3 model parameters (K^{trans}, v_e and, v_p).

5.4.1 Normal Peripheral Zone Tissue

In order to assess the performance using VIF calculated using the AC-ICA algorithm in PK analysis, an ROI was identified on the normal peripheral zone (PZ) tissue of the prostate gland. A normal PZ tissue appears as a high intensity region on the peripheral zone of the prostate (Figure 5-6a) and was identified using the T_2-weighted images of the prostate (in cases such a tissue could be identified). PK parameters reflect the intrinsic characteristics of the tissue (permeability and perfusion) and thus, should have the same values for normal PZ tissue in different patients, and the smaller the variations of the PK parameters for this tissue type, the better the performance of the PK analysis method. The PK parameters of the normal PZ tissue obtained using the VIF were compared to the PK parameters obtained using the AIF between patients to assess the performance of the method in 28 DCE-MRI datasets of prostate cancer patients.
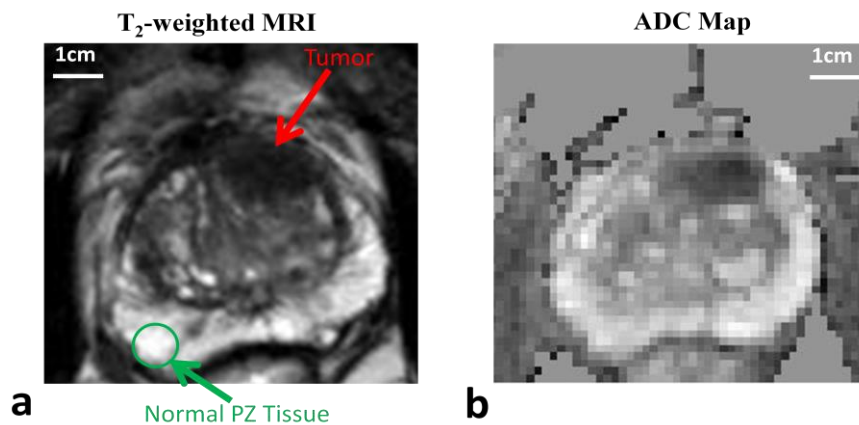
Figure 5-6 a) The T_2-weighted image of the sample prostate that was shown in Figure 5-3 where the tumor in the central gland is visible as a hypo-intense region (show by the red arrow). An ROI in the normal PZ tissue is also shown in green (hyper-intense region in PZ). b) ADC map of the same slice showing the tumor in central zone as a hypo-intense region.

5.4.2 Tofts-Kety Model Results

The ICA-based VIF and AIF from femoral artery were first used in Tofts-Kety model which has two model parameters (K^{trans} and v_e) and ignores the contribution of the vascular compartment (v_p) in tissue concentration. The two model parameters were calculated for every voxel in the prostate region for all DCE-MRI datasets. For each 3D DCE-MRI dataset the analysis was performed on the slices that were identified as having the tumor or a suspicious lesion. Figure 5-7 shows the K^{trans} map calculated using the VIF and the AIF for the 6 patients whose VIFs were shown in Figure 5-5. As can be seen in this figure, in both VIF-based and AIF-based K^{trans} maps, the voxels of the normal PZ tissue have small values.

In addition, in both methods the tumor or suspicious lesion is identifiable and its voxels have high K^{trans} values. Thus, the performance of the methods in detecting the suspicious region is similar. This figure also shows the T_2-weighted MR image and ADC map of the prostate slice to be used for tumor and normal PZ tissue detection.
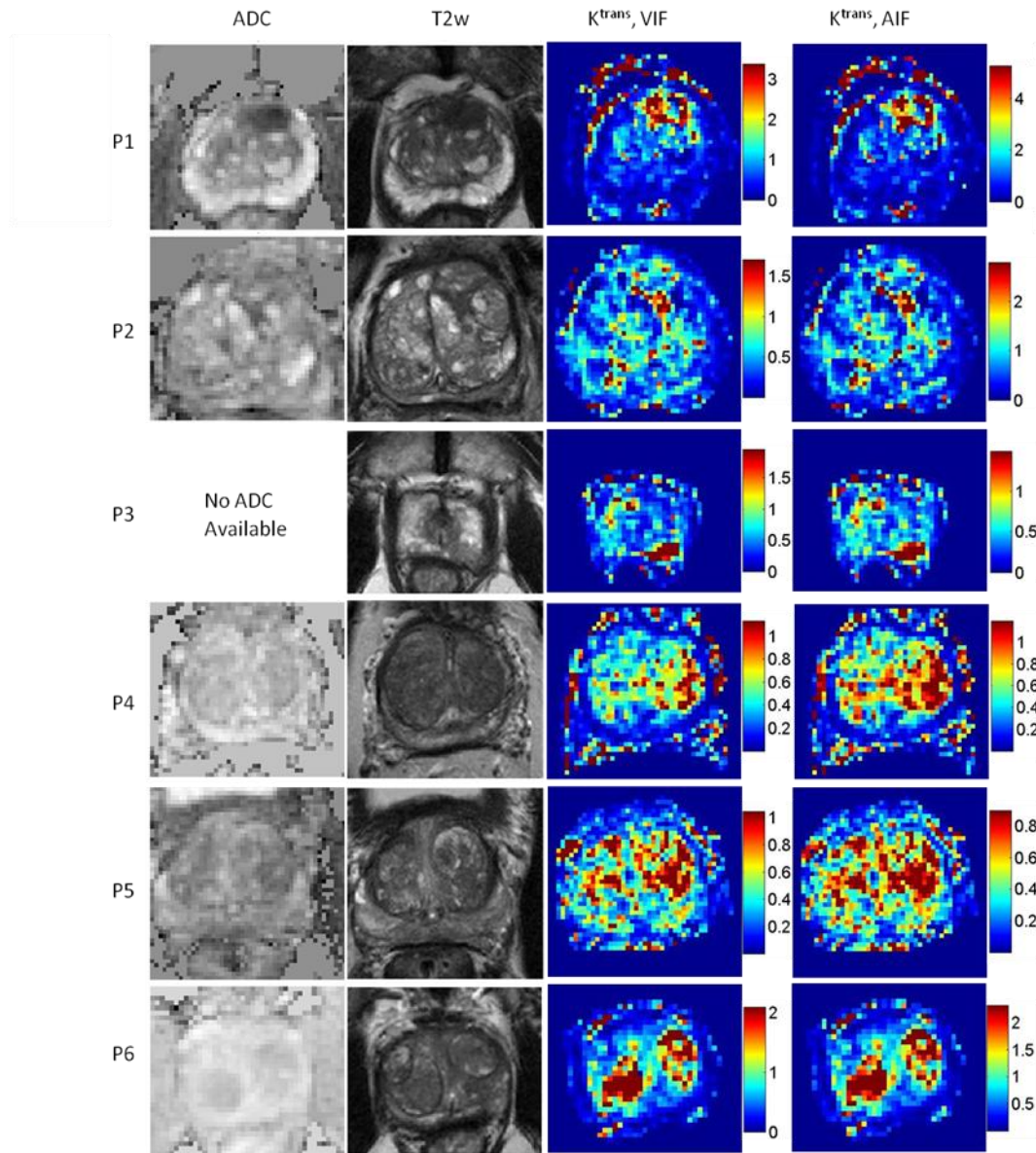
Figure 5-7 This figure shows the ADC map (first column), and T_2-weighted MR image of the slices that were shown in Figure 5-5 which were used for tumor detection. The corresponding K^{trans} maps calculated for Tofts-Kety model using the normalized VIF (third column) and normalized AIF (fourth column) are also shown.

The K^{trans} value of the normal PZ tissue is a characteristic of this tissue type and has to have the same value in different patients, independent of the analysis technique. The variations in the K^{trans} values reported for this tissue in different studies might be due to errors in modeling and analysis as well as errors in the AIF used for PK analysis. Thus, the method

that provides a smaller variation in the value of this parameter is considered to be performing better. We selected an ROI on the normal PZ tissue of the prostate in all patients where such a region was visible. The number of normal PZ voxels in each patient varied from 20 to 300 voxels. To avoid the bias from the patients with larger number of voxels in summary statistic and also considering that the pooled distribution of all PZ voxels was positively skewed (was not Gaussian), the means of the K^{trans} value for each patient were used to assess the variations. Using the mean value, each patient was represented with one value in the distribution and according to central limit theorem their distribution would be Gaussian (distribution of the sample means is Gaussian). The mean and standard deviation of these values were then calculated and reported in Table 5-1 using AIF- and VIF-based methods.

The table also reports the mean and standard deviation of the K^{trans} value for normal PZ tissue using AIF and VIF without normalization. These results show that normalizing the curves provides smaller variation in the K^{trans} value of the normal PZ tissue. These values were calculated for the entire patient population with normal PZ tissue which included 20 datasets (in 10 patients there was no visible normal PZ tissue).

Table 5-1 The mean and standard deviation of the K^{trans} value calculated from the distribution of the mean values for each patients for normal PZ tissue(the mean value for each patient was calculated by averaging the K^{trans} values of all normal PZ voxels in that patient). The K^{trans} values were calculated for Tofts-Kety model using VIF (normalized and not normalized) and AIF (normalized and not normalized) for normal PZ tissue (for 20 patients).

Method	Tissue Type	VIF (AC-ICA) [min^{-1}]	AIF (femoral artery) [min^{-1}]
With Normalization	Normal PZ	**0.26** ±0.07	**0.33** ±0.19
Without Normalization	Normal PZ	**1.28**±0.58	**0.35**±0.42

Figure 5-8a presents the box-plot of the distribution of K^{trans} values for the normal PZ region that was identified for each patient. The box-plot shows the median (horizontal line) and the 25 percentile to 75 percentile range (box) for all slices in each patient in which a normal PZ region was identified (for both the VIF-based and AIF-based K^{trans} maps). As can be seen in this figure the K^{trans} maps calculated using the AC-ICA based VIF provided smaller

variation in the K^{trans} values of the normal PZ tissue compared to using the AIF. Figure 5-8b shows the box-plot of the K^{trans} parameter for the tumor or suspicious region for the VIF and AIF-based methods for each patient (the values of all slices containing tumor were considered in the plots). Comparing these box-plots with those showing the K^{trans} values for normal PZ tissue (note the difference in the scales used in these plot which are chosen such that each plot shows the variations of K^{trans} parameters for its corresponding tissue type) shows there is clear separation between the normal and tumor tissues.
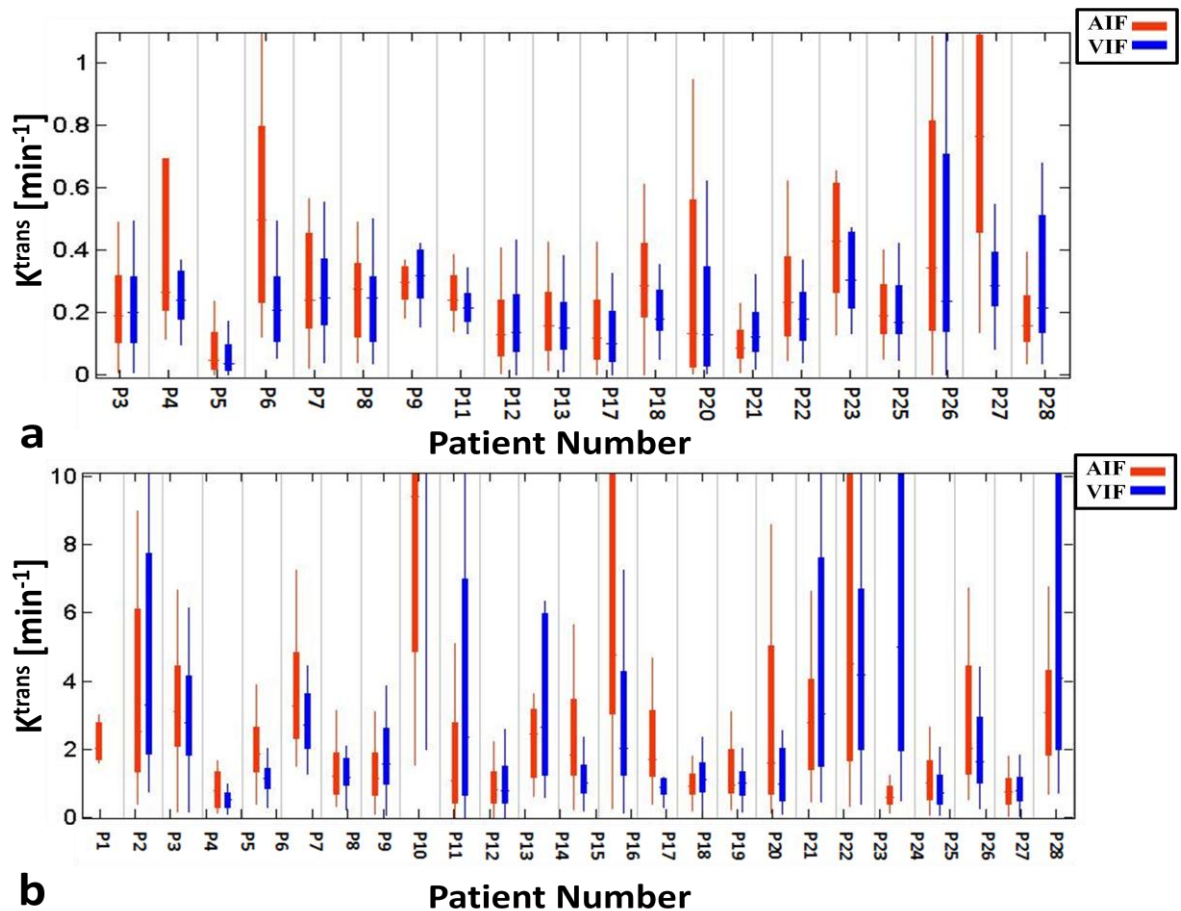
Figure 5-8 Box-plot of the K^{trans} value distribution for Tofts-Kety model. The box-plot shows the median (horizontal line) and the 25 percentile to 75 percentile range (box) for the VIF-based and AIF-based K^{trans} maps for a) normal PZ region (in patients that a normal PZ region was identified), and b) tumor or suspicious region for all slices in each patient.

Table 5-2 reports the median and 25 percentile and 75 percentile range for the normal PZ tissue and the tumor or suspicious regions that were identified in prostate for all patients. The mean and standard deviation was not used here as both distributions were positively skewed. These ranges show that both methods provided a clear separation between the normal PZ and tumor region when the VIF (or AIF) curves were normalized. However, there was large

96

overlap between their distributions without normalization. These values will be compared to several values reported in the literature in the next section.

Table 5-2 The median and inter-quartile ranges of the K^{trans} value calculated using pooled distribution (using all patients) of all voxels in normal PZ and Tumor regions (both distributions were positively skewed). The K^{trans} values were calculated for Tofts-Kety model using VIF (normalized and not normalized) and AIF (normalized and not normalized) for the normal PZ tissue (for 20 patients) and tumor or suspicious tissue (for 28 datasets).

Method	Tissue Type	VIF (AC-ICA) [min^{-1}]	AIF (femoral artery) [min^{-1}]
With Normalization	Normal PZ	**0.16** [0.07 0.27]	**0.16** [0.07 0.32]
	Tumor	**1.25** [0.82 2.31]	**1.69** [0.95 3.24]
Without Normalization	Normal PZ	**0.60** [0.25 1.48]	**0.07** [0.03 0.24]
	Tumor	**4.81** [2.32 9.18]	**0.48** [0.22 1.41]

5.4.3 Extended Tofts-Kety Model

The extended Tofts-Kety model that has three parameters (K^{trans}, v_p and v_e) was also used for calculating the PK parameters using both the VIF and the AIF. The parameter calculation using AIF was performed similar to the Tofts-Kety model analysis by fitting the contrast agent concentration curve of the tissue to the model equations and solving for the three model parameters. The VIF-based parameters were calculated with two different methods:

1- Using the ICA-derived vascular map as the v_p parameter and subtracting the $v_p c_p(t)$ term from the contrast agent concentration of the tissue and then fitting this new tissue concentration curve to the Tofts-Kety model equations and calculating the remaining two PK parameters (K^{trans} and v_e) . This method is called **method1** or **m1** in the tables and figures of this chapter.

2- Fitting the tissue concentration curve to the extended Tofts-Kety model equations and calculating the three model parameters. This method is called **method2** or **m2** in the tables and figures of this chapter.

97

Figure 5-9 shows the K^{trans} map calculated using the VIF (both methods) and the AIF for the patients that were shown in Figure 5-7. As can be seen in these figures, similar to the Tofts-Kety model, the VIF-based and AIF-based K^{trans} maps of the normal PZ tissue had small values and the tumor or suspicious lesions had large values. Thus, the performances of the methods in detecting the suspicious region were similar.
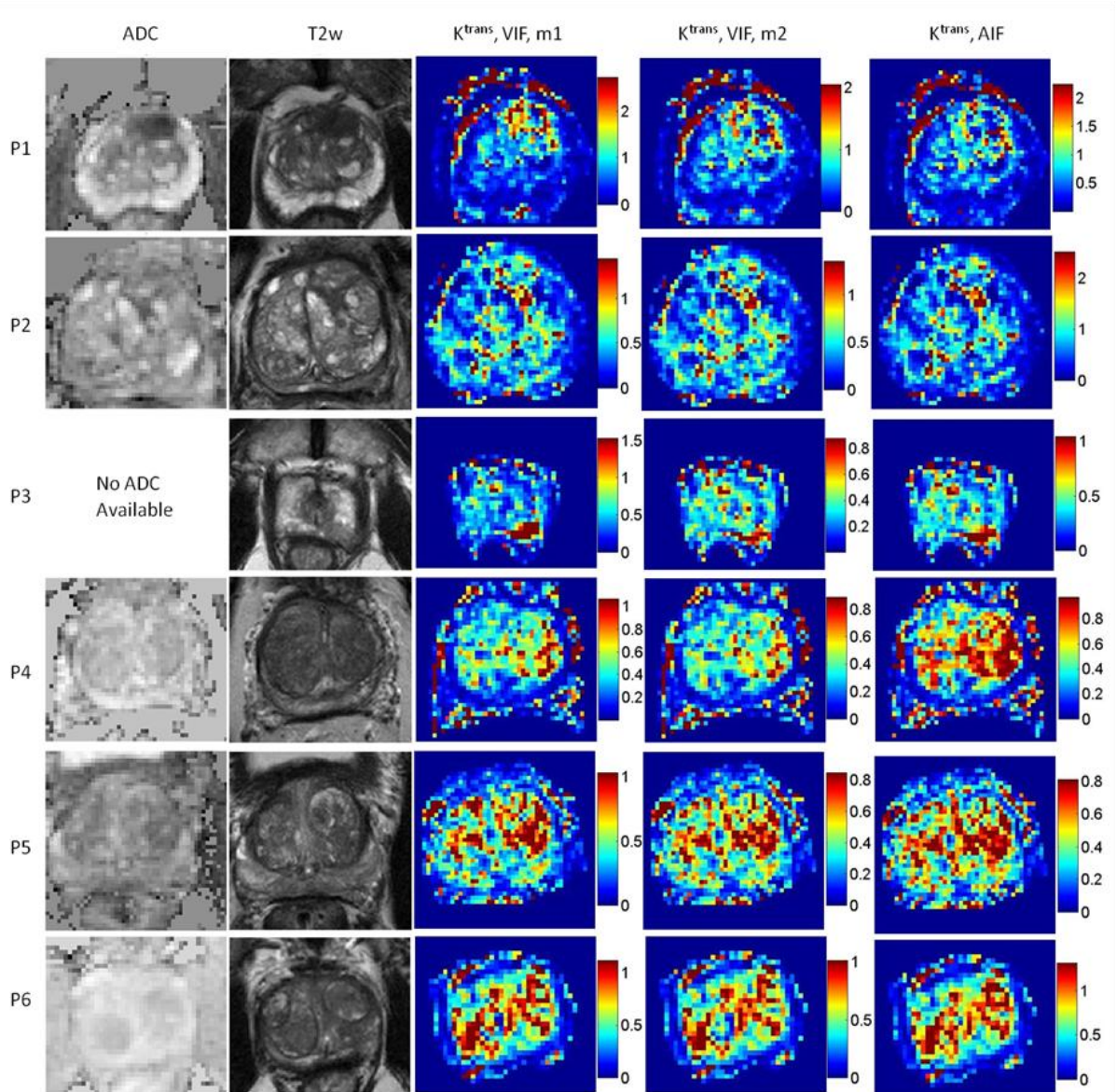
Figure 5-9 The ADC map (first column), and T_2-weighted MR image of the slices that were shown in Figure 5-5 which were used for tumor detection. The corresponding K^{trans} maps calculated for extended Tofts-Kety model using the normalized VIF and using ICA-derived v_p map (third column), the normalized VIF and fitting for all 3 PK parameters of extended Tofts-Kety model (fourth column), and normalized AIF (fifth column).

The v_p maps calculated for each method (three parameter fitting with VIF, v_p from AC-ICA and two parameter fitting with VIF, and three parameter fitting with AIF) are shown in Figure

5-10 for the 6 sample datasets. The similarity between the v_p map calculated directly from ICA and the v_p map that resulted from curve fitting in PK analysis proves that:

1-   The component that was separated by ICA and was considered as the intravascular component is actually the intravascular component

2-   The v_p map can be directly obtained using AC-ICA and no PK modeling is required.

Moreover, having the v_p map before PK analysis makes the curve fitting simpler and the system of equations more stable.
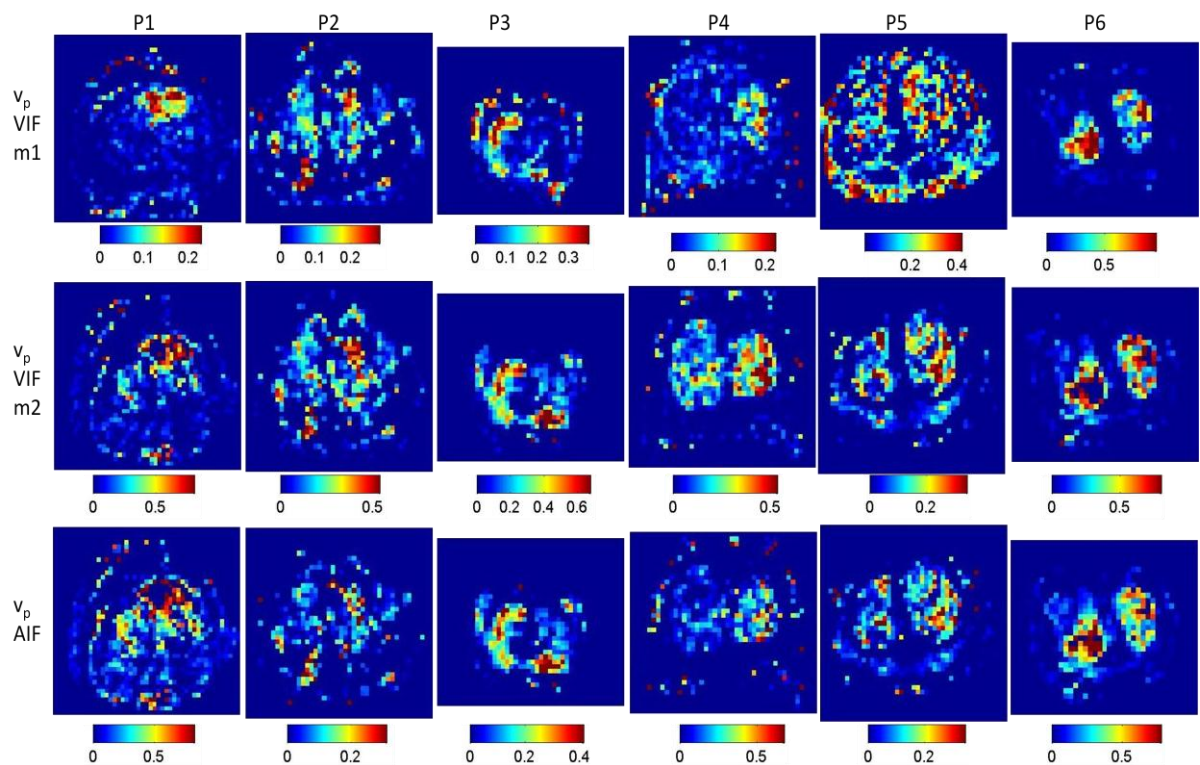
Figure 5-10 The v_p maps for the 6 sample patients shown in Figure 5-5, calculated for extended Tofts-Kety model using the normalized VIF and using ICA-derived vascular map as v_p (first row), the normalized VIF and fitting for all 3 PK parameters of extended Tofts-Kety model (second row), and normalized AIF (third row).

Similar to the Tofts-Kety model section (Figure 5-8 and Table 5-1), the mean and standard deviation of the K^{trans} values for normal PZ tissue (distribution of the mean values), using the extended Tofts-Kety model, are reported in Table 5-3 for all three PK analysis methods. Similar to Figure 5-8 and Table 5-1, these values were calculated for the entire patient population with normal PZ tissue (20 datasets). This table also reports the K^{trans} value for normal PZ tissue using the VIF (both method) and AIF without normalization which shows that normalization provides a smaller variation in the K^{trans} value of the normal PZ tissue.

Table 5-3 The mean and standard deviation of the K^{trans} value calculated from the distribution of the mean values for each patients for normal PZ regions (the mean value for each patient was calculated by averaging K^{trans} values of all normal PZ tissue voxels in that patient). The K^{trans} values were calculated for extended Tofts-Kety model using VIF (normalized and not normalized) and AIF (normalized and not normalized) for the normal PZ tissue (for 20 patients).

Method	Tissue Type	VIF (AC-ICA) Method 1 [min^{-1}]	VIF (AC-ICA) Method 2 [min^{-1}]	AIF (femoral artery) [min^{-1}]
With Normalization	Normal PZ	0.21±0.05	0.23±0.06	0.26±0.11
Without Normalization	Normal PZ	1.09±0.53	1.19±0.55	0.29±0.34

Figure 5-11a presents the box-plot of the K^{trans} values for the normal PZ region that was identified for each patient. The box-plot shows the median (horizontal line) and the 25 percentile to 75 percentile range (box) for all the slices in each patient that a normal PZ region was identified (for the two VIF-based and the AIF-based K^{trans} maps). As can be seen in this figure, the K^{trans} maps that were calculated using the VIF resulted in smaller variation in the K^{trans} values of the normal PZ tissue compared to the maps calculated using the AIF. Comparing the results of the two VIF-based methods shows that their performances in calculating the K^{trans} value of the normal PZ tissue were similar. Figure 5-11b show the box-plot of the K^{trans} parameter for the tumor or suspicious region for the two methods based on AC-ICA and the AIF-based method for each patient (the values of all slices that contained the tumor were considered in generating these plots). Comparing these box-plots with the box-plots showing the distribution of the K^{trans} value for normal PZ tissue shows that there is a clear separation between the two tissues (note the differences in the scales of these plots).

Table 5-4 reports the median and inter-quartile range of the K^{trans} obtained for the tumor and normal PZ tissues for the AC-ICA based methods as well as the AIF-based PK parameters for extended Tofts-Kety model (both with and without normalization). It also reports a few of the K^{trans} values that are reported in the literature and shows that the AC-ICA based methods provide a better separation of the normal PZ and tumor tissues.

Table 5-4 The median and inter-quartile ranges of the K^{trans} value calculated using pooled distribution (using all patients) of all voxels in normal PZ and tumor regions (both distributions were positively skewed). The K^{trans} values were calculated for extended Tofts-Kety model using VIF (normalized and not normalized) and AIF (normalized and not normalized) for the normal PZ tissue (for 20 patients) and tumor/suspicious tissue (for 27 patients). The table also reports several prostate K^{trans} values reported in the literature.

| Method	Tissue Type	VIF (AC-ICA) Method 1 [min^{-1}]	VIF (AC-ICA) Method 2 [min^{-1}]	AIF (femoral artery) [min^{-1}]
With Normalization	Normal PZ	**0.13** [0.07 0.22]	**0.14** [0.07 0.25]	**0.15** [0.07 0.28]
	Tumor	**0.59** [0.40 0.88]	**0.97** [0.64 1.51]	**0.97** [0.61 1.47]
Without Normalization	Normal PZ	**0.51** [0.22 1.29]	**0.56** [0.23 1.36]	**0.07** [0.02 0.20]
	Tumor	**2.29** [1.01 4.28]	**3.30** [1.44 6.14]	**0.31** [0.15 0.78]
Moradi [160]	Normal PZ	-	-	**0.07**±0.047
	Tumor	-	-	**0.148**±0.071
Langer [161]	Normal PZ	-	-	**0.29** [0.09 0.87]
	Tumor	-	-	**0.36** [0.16 1.28]
Ocak [162]	Normal PZ	-	-	**0.23**±0.25
	Tumor	-	-	**0.47**±0.57
Korporral [163]	Normal PZ	-	-	**0.10** [0.04 0.21]
	Tumor	-	-	**0.44** [0.25 0.75]
Li [164]	Normal PZ	-	-	**0.09**±0.07
	Tumor	-	-	**0.32**±0.23
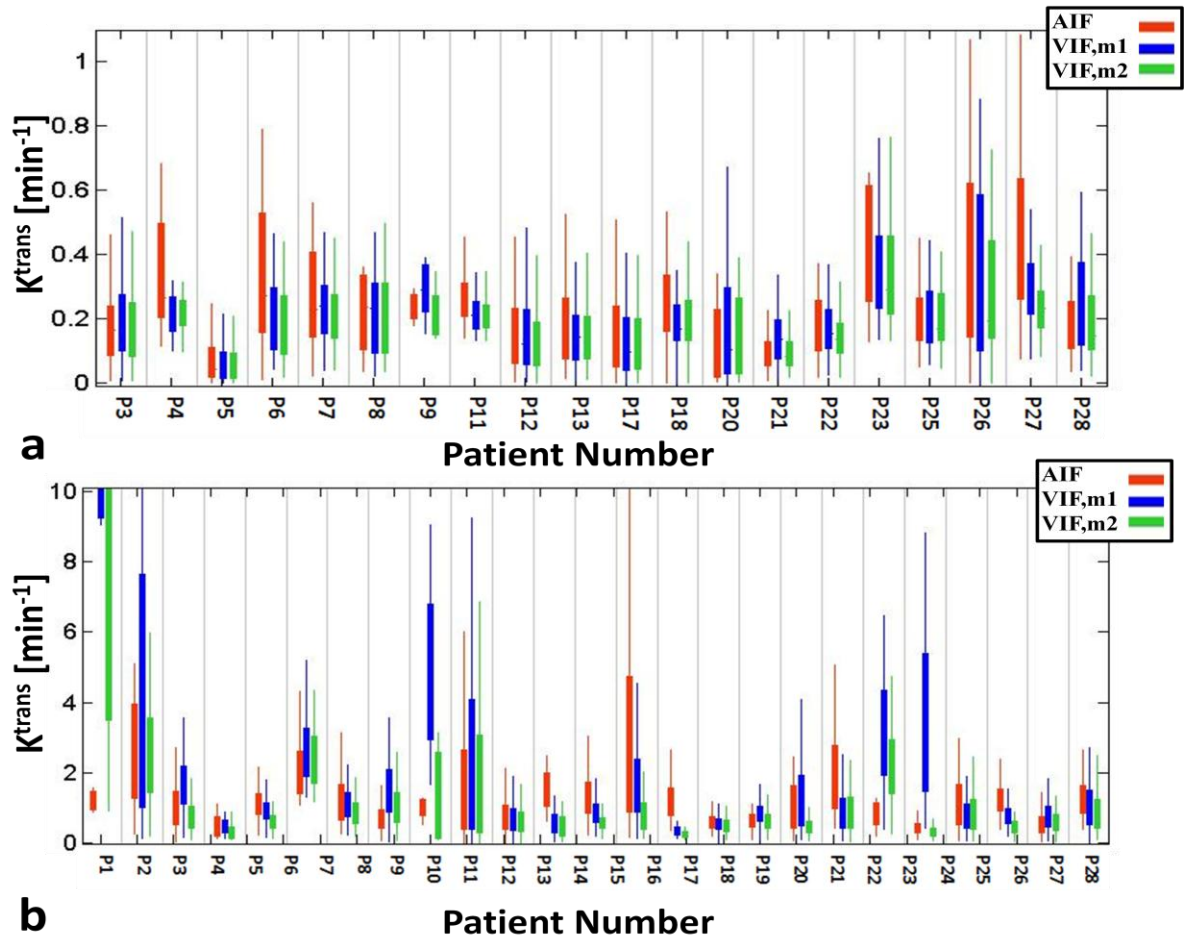
Figure 5-11 Box-plot of the K^{trans} value distribution for extended Tofts-Kety model. The box-plot shows the median (horizontal line), and the 25 percentile to 75 percentile range (box) for the VIF-based K^{trans} maps using extended Tofts-Kety model for both methods (using ICA-derived vascular map as v_p, and using ICA-derived VIF and curve fitting for all 3 parameters) and, AIF-based K^{trans} maps for a) normal PZ region (in patients that a normal PZ region was identified), and b) tumor or suspicious region for all slices in each patient.

5.5 Temporal resolution

The effects of decreasing the temporal resolution on the PK parameters of each method are studied in this section. AIF-based methods are very sensitive to temporal resolution since a low temporal resolution DCE-MRI dataset might not capture the full temporal profile of the AIF in a blood vessel. In humans the difference between the peak for first pass of the contrast agent and the peak of its recirculation is about 0.5 [min]. Thus, a very high temporal resolution is required to measure the AIF accurately. However in the ICA-based methods, since the VIF is being calculated in the tissue of interest (which does not have a large artery), the contrast agent is dispersed and has a wider profile (as it arrives in the tissue through several paths and blood flow is slower in smaller vessels). Thus, decreasing the temporal resolution in VIF-based analyses should not have as significant effect as it has on the AIF

based methods. Being able to decrease the temporal resolution enables acquiring images with high spatial resolution which further improves accuracy of VIF calculation and PK analysis.

Figure 5-12 shows the K^{trans} maps for 3 sample patients corresponding to high and low temporal resolution datasets for the Tofts-Kety model (using the AIF-based and VIF-based methods), and the extended Tofts-Kety model (using the AIF-based and two VIF-based methods). For high temporal resolution data, the entire DCE-MRI data having all time points was used. The low resolution data was generated by removing every other frame in the datasets which reduced the temporal resolution to its half without any effect on the spatial resolution. The subtraction images generated by subtracting the K^{trans} map of the low temporal resolution dataset from that of the high temporal resolution dataset and computing the absolute of their difference are also shown in Figure 5-12. The model used here is not a realistic approximation to the DCE-MRI data with low temporal resolution. However, it is used as an initial attempt to assess the effects of changing temporal resolution on PK parameters. We expect to obtain similar results in realistic cases of decreasing temporal resolution which require additional data acquisition that was not performed in this thesis.
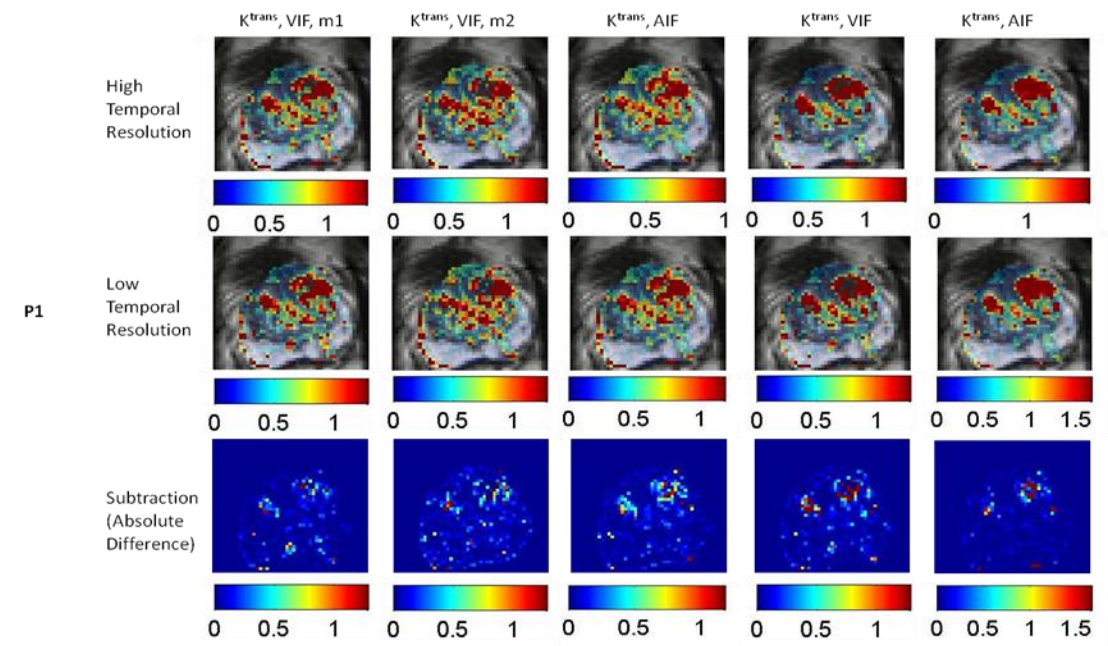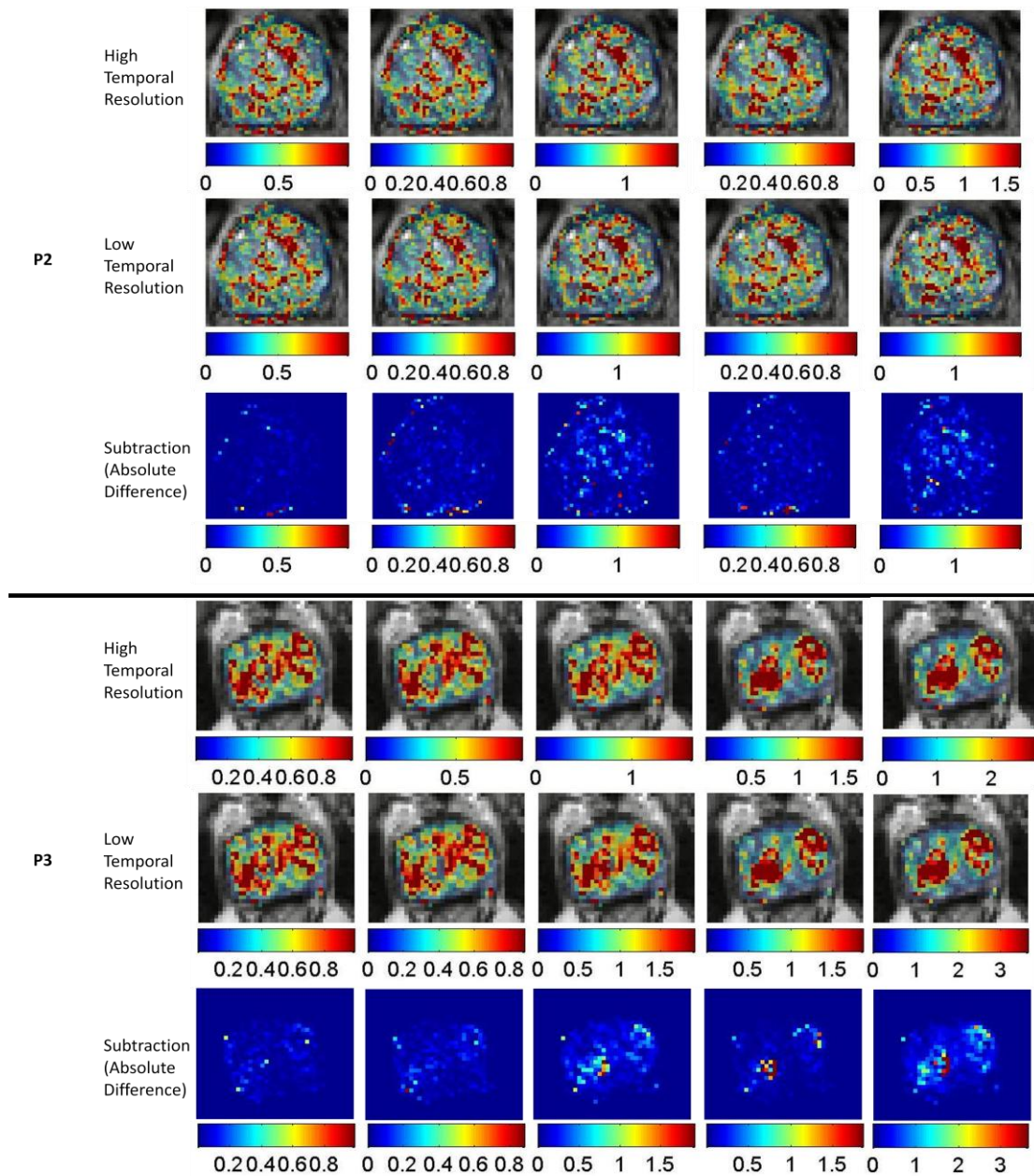
Figure 5-12 The K^{trans} map of 3 sample prostate datasets. For each patient the first row shows the K^{trans} map of high temporal resolution data, the second row shows the K^{trans} map of low temporal resolution data, and the third row show the absolute difference between the high temporal resolution and low temporal resolution K^{trans} maps. The K^{trans} maps and difference maps were calculated for the extended Tofts-Kety model using: the VIF using the ICA-derived vascular map as v_p (first column), the VIF and curve fitting for all 3 model parameters (second column), and the AIF (third column). The maps were also calculated for Tofts-Kety model using: the VIF (fourth column) and the AIF (fifth column).

Table 5-5 reports the percentage difference between the high and low resolution K^{trans} maps for 8 sample datasets (including the 3 datasets that were shown in Figure 5-5) for the entire prostate region and the tumor region. It can be seen in Table 5-5 and Figure 5-12 (particularly in the subtraction images) that the VIF based methods were more robust to decreasing the

temporal resolution and resulted in significantly smaller changes in the PK parameters. Moreover, the largest changes in the AIF based methods occurred in the tumor region (which is the primary target in PK analysis), while the VIF based images result in smaller change in the K^{trans} values of the tumor region compared to the entire prostate.

Table 5-5 The percentage change (mean and standard deviation) in K^{trans} parameter due to decreasing temporal resolution by factor of 2, for the tumor and entire prostate gland (calculated for 8 prostate cancer patients). The differences were calculated for extended Tofts-Kety model using AIF and the two VIF-based methods as well as for Tofts-Kety model using both AIF and VIF.

Patient	ROI	Extended Tofts-Kety Model (%)			Tofts-Kety Model (%)	
		VIF (AC-ICA) Method 1	VIF (AC-ICA) Method 2	AIF (femoral artery)	VIF (AC-ICA)	AIF (femoral artery)
P1	Tumor	10±14	13±20	22±41	18±37	16±34
	Prostate	7±13	15±24	16±54	12±22	12±19
P2	Tumor	4±4	6±7	10±7	5±5	18±19
	Prostate	5±7	8±13	12±7	7±10	13±16
P3	Tumor	5±6	11±22	30±34	11±25	6±6
	Prostate	6±10	10±16	24±22	9±16	10±13
P4	Tumor	7±7	12±15	21±26	11±17	27±59
	Prostate	9±13	15±22	20±26	13±19	26±60
P5	Tumor	7±5	8±7	22±27	7±7	14±17
	Prostate	8±11	12±16	19±25	11±14	14±44
P6	Tumor	7±8	13±17	21±25	10±12	11±10
	Prostate	7±11	11±16	13±19	9±13	11±14
P7	Tumor	7±12	14±23	21±30	12±19	15±14
	Prostate	8±11	10±16	14±22	9±16	14±38
P8	Tumor	5±7	14±21	14±17	11±12	21±25
	Prostate	5±9	12±20	14±18	8±10	13±17

5.6 Discussions

This chapter presented the results of applying the proposed VIF calculation algorithm (AC-ICA) to PK analysis of prostate tissue and compared its results to the commonly used AIF-based method. A normalization step was also introduced in this chapter that normalized the VIF (or AIF) curves with respect to their area under the curve (AUC). It was shown in the normalization section and appendix IV that if two VIFs (or AIFs) satisfied the Tofts-Kety model equations for a specific tissue type (e.g. normal PZ tissue), their AUC are equal. In addition to enabling comparison between the K^{trans} values of VIF-based and AIF-based PK analyses, the normalization also resulted in more consistent K^{trans} value for the normal PZ tissue (as reported in Table 5-1 and Table 5-3). It also provided better separation of the K^{trans} values of normal PZ tissue and tumor tissue as reported in Table 5-2 and Table 5-4 (the inter-quartile ranges were better separated).

The K^{trans} value is a characteristic of the tissue, as it represents its vascular permeability and perfusion, and should be the same regardless of the VIF (or AIF) calculation method being used. Thus, both AIF-based and VIF-based methods should result in similar K^{trans} values for the normal PZ tissue, and the method that results in smaller variation in the K^{trans} value of the normal PZ tissue in different subjects has better performance. Table 5-1 and Table 5-3 show that after normalization the mean K^{trans} value of the AIF-based and VIF-based methods (in Tofts-Kety and extended Tofts-Kety models) were close to each other which shows both methods were calculating the same value for the normal PZ tissue (these mean values corresponded to two different samples of the same population as assessed by ANOVA analysis). However, the VIF-based methods provided smaller variation (smaller standard deviation) compared to the AIF-based method and thus, was working better in both Tofts-Kety and extended Tofts-Kety models.

There was not a significant difference between the K^{trans} values calculated by the two VIF-based methods in extended Tofts-Kety model which only differed in the calculation of the v_p map. Moreover, comparing the v_p maps (Figure 5-10) calculated in the extended Tofts-Kety model by the AIF-based and VIF-based (method 2) analyses with the v_p map that was obtained from the AC-ICA algorithm (method 1 in VIF-based extended Tofts-Kety model), there were not significant differences between these maps. These results showed that the vascular map obtained by AC-ICA algorithm represented the intravascular space of the prostate tissue. Thus, the vascular map of the tissue that could be useful, for instance in

assessing tumor response to anti-angiogenic therapies, can be calculated using AC-ICA algorithm without the need for modeling or even converting the MR signal intensity into contrast agent concentration which are time consuming steps and are prone to error.

There was clear separation between the K^{trans} value of normal PZ tissue and the tumor tissue as reported in Table 5-2 and Table 5-4 and also shown in Figure 5-8 and Figure 5-11. Comparing these results to the results that have been previously reported in the literature on the normal PZ tissue and tumor K^{trans} distributions; the results reported here using both normalized VIF and normalized AIF provided better separation of the two tissues which demonstrates the better performance of our method. Moreover, comparing the results obtained using the normalized AIF compared to the PK parameters using AIF without normalization and the values that were reported in literature, normalization of the AIF with respect to its AUC resulted in better separation between the normal PZ and tumor tissues.

However, no specific trend in the K^{trans} values or correlation between the K^{trans} values and the Gleason score were observed in these datasets. One potential reason for this would be the presence of several tumor types (different in both tumor location and Gleason score) in the datasets and not having a large number of datasets with a specific tumor type. Further study and a larger patient population would be required to study such correlations.

Finally, we studied the effects of changing the temporal resolution on the performance of the proposed VIF-based PK parameters and compared them to the results of AIF-based methods. It has been reported in the literature that if an AIF derived from a high temporal resolution dataset is used and the temporal-resolution of the tissue curve is reduced by a factor of 3, the change in the PK parameters is only about 4% [165]. However, measuring the AIF from a low temporal resolution dataset has significant effect on the PK parameters since the AIF has a narrow FWHM (full width at half maximum) having only a few data points in the main (first pass) part of the curve, and thus under-sampling may result in large changes in the AIF. AIF is also sensitive to in-flow effects and saturation of MR signal due to high contrast agent concentration in the artery. VIF on the other hand is calculated in the tissue which has significantly lower concentration and thus signal saturation is not an issue, and there is significantly lower blood flow and thus in-flow effects are smaller. Furthermore, the contrast agent bolus gets dispersed and has a wider FWHM consisting of larger number of time points in its main region as it travels from the artery into the tissue through several paths and it is being measured in smaller blood vessels with low blood flow.

107

Consequently, decreasing the temporal resolution in VIF-based analyses should result in smaller change in the PK parameters compared to AIF-based analyses. The results shown in Figure 5-12 and reported in Table 5-5 show that decreasing the temporal resolution to its half (removing every other frame in DCE-MRI dataset), resulted in much smaller change in PK parameters of VIF-based method compared to AIF-based parameters. On average the percentage changes in VIF-based methods were about 3 times smaller than the AIF-based method. In addition, the AIF-based method resulted in a higher change in PK parameters in the tumor region compared to the entire prostate while the VIF-based method resulted in similar changes in both regions. This could be attributed to the fact that VIF was calculated locally and was biased towards the more vascular regions of the prostate region (which is the tumor region), and thus should provide better estimate to the intravascular signal of these regions.

The main advantage of being able to decrease the temporal resolution without losing much accuracy in PK analysis is that it enables acquiring data with higher spatial resolution. Having higher spatial resolution, in addition to decreasing partial volume effect and increasing the accuracy of PK analysis, increases the accuracy of the VIF calculation algorithm as the intravascular and extravascular spaces are better separated (the effects of different spatial resolutions were shown in the previous chapters using numerical and physical tissue-mimicking phantoms). In this thesis we only assessed the changes in the prostate PK parameters as the temporal resolution was reduced. Assessing the effects of the higher spatial resolution, which is made possible by decreasing the temporal resolution, on the PK parameters and the VIF curves requires additional data acquisition and was not performed here.

5.7 Summary

In this chapter the steps required for converting the AC-ICA results, which is in MR signal intensity, into VIF curves, which is in contrast agent concentration, were explained. A normalization step was also introduced and explained using both numerical phantom and prostate tissues. The performance of the proposed VIF on PK analysis of DCE-MR images of a cohort of 27 prostate cancer patients (28 datasets) was also assessed and compared to a commonly used AIF-based PK analysis. It was shown that the VIF-based method was capable of providing more consistent (smaller variation) PK parameters for the normal PZ tissue in both Tofts-Kety and extended Tofts-Kety models. There was better separation of the

K^{trans} values of normal PZ tissue and tumor using the normalized VIF-based method compared to several previous studies. Finally, the effects of reducing the temporal resolution on the PK parameters was studied and it was shown that the proposed VIF-based method (compared to AIF-based methods) was less sensitive to decreasing temporal resolution which enables acquiring images with higher spatial and lower temporal resolutions. These results show that the proposed algorithm could replace AIF-based analyses and is capable of providing better or equivalent results. The algorithm could also be used for PK analysis in cases an AIF cannot be measured such as small animal studies (where it is difficult to find an artery or very high temporal resolution is required for AIF measurement).

The next chapter presents the summary and conclusions of this thesis and details the advantages and disadvantages of the proposed method. It will also present the future directions that could be followed to analyze and validate the aspects of the proposed VIF calculation algorithm and its corresponding PK analysis that were not addressed in thesis and also its potential applications.

Chapter 6

Conclusions and Future Directions

The proposed ICA-based VIF calculation algorithm (AC-ICA) was applied to DCE-MR images of prostate cancer patients and PK analysis was performed in the previous chapter. The performance of the algorithm was evaluated via comparing its results to the PK parameters calculated using contrast enhancement in the femoral artery as the AIF. It was shown that the proposed VIF could be used for PK analysis and resulted in acceptable PK parameters. Moreover, the VIF-based analysis provided more consistent values for normal PZ tissue which showed it has a better performance compared to AIF-based analysis. These results showed that the VIF-based analysis, in addition to enabling PK analysis when there is no AIF to be used (e.g. in animal studies), could replace AIF-based methods and provides better or equivalent results even in cases an AIF can be measured.

This chapter provides a summary of the work that was presented throughout the thesis and presents the concluding remarks. It will also discuss the future directions that need to be followed in order to fully characterize and evaluate the proposed algorithm and its potential applications.

6.1 Motivation

As our understanding of cancer biology increases and treatment options improve, personalized therapy becomes more feasible. These therapies are very specific and usually expensive, thus selecting the patients that would benefit from them and also assessment of their therapeutic response is important. Currently, the main approach used for assessing therapeutic response is tumor size measurement which might not necessarily represent the actual response, e.g. in anti-angiogenic therapies. Thus, there is increasing interest in developing novel metrics using functional imaging techniques and the focus of this thesis was on quantification of dynamic contrast enhanced MR images of tumor tissues.

DCE-MR imaging combined with pharmacokinetic (PK) analysis of a tumor provides quantitative information about tumor perfusion and vascular permeability. Such information

has been found to be related to prognostic factors such as tumor grade and thus, its role in assessing anti-angiogenic and anti-vascular therapies is increasing. Most PK models require measurement of the contrast agent concentration in the vasculature as an input. However, this vascular input function (VIF) is inseparable from the signal in the extravascular extracellular space (EES). Hence, it is approximated outside of the tissue of interest, e.g. in an adjacent artery, in a reference tissue (muscle), or using a population-averaged signal. The main objective of this thesis was to develop and evaluate a novel algorithm for calculating the local VIF at the tissue of interest and separating it from the signal of the EES. Such a VIF has the potential to increase accuracy of PK analysis and also could be used when an artery for AIF measurement is not available or other AIF approximation techniques cannot be used.

6.2 Mag-ICA algorithm

The first objective of this thesis was assessing the feasibility of using data-driven techniques, in particular independent component analysis (ICA), for calculating a local VIF by separating the contrast agent concentration in the vascular space of the tissue from its EES concentration.

In order to achieve this goal the Mag-ICA algorithm was developed (chapter 3) that applied an ICA algorithm to the magnitude of the DCE-MRI signal, with the third moment as its non-linearity function. This chapter showed that ICA was capable of performing such a separation and the performance of the algorithm was evaluated using numerical and physical tissue-mimicking phantom as well as *in vivo* VX2 tumors in thigh muscle of rabbits.

In the numerical study the actual intravascular signal (which was known from our simulations), and in the physical phantom study the signal in the in-flow line was used to assess the performance of the algorithm. In the *in vivo* study, the spatial distribution of the separated intravascular component was compared to the *in vivo* contrast enhanced ultrasound (CE-US) images of the tumor. US contrast agent, i.e. microbubbles, stay intravascular and thus, their signal represent the actual intravascular space and was used to evaluate the separated intravascular signal spatially. The temporal enhancement curve of the intravascular signal was evaluated using the signal of an artery that was close to the tumor.

These results showed the feasibility of using ICA for local VIF calculation. However, there were several issues with using the Mag-ICA algorithm as follows:

1-   Using the magnitude of MR signal violates the linear mixture assumption of ICA

2-   Using a fixed non-linearity function in ICA disregards the variability between the vasculature of different tumors.

Thus, a more sophisticated ICA-based separation algorithm (AC-ICA) was developed and was evaluated in chapter 4.

6.3 AC-ICA algorithm

An adaptive complex independent component analysis (AC-ICA) algorithm was developed in chapter 4 to address the issues of Mag-ICA algorithm. This algorithm used the complex-valued MR signal to satisfy the linear mixture assumption of ICA. It also estimated the spatial distribution of the tumor vasculature at every iteration of the ICA algorithm and derived the ICA non-linearity function from the estimated distribution. The distribution of the tumor vasculature was estimated using a linear combination of 3 to 5 generalized Gaussian distributions (GGD). The shape parameters of these GGDs were calculated at each iteration through an expectation maximization framework and the GGD with highest membership probability was used to derive the ICA non-linearity.

The performance of this algorithm was evaluated using numerical and physical tissue-mimicking phantoms. It was demonstrated in chapter 4 that, compared to Mag-ICA, the AC-ICA algorithm performed better in separating the intravascular space, and generated reproducible results, particularly when dealing with low resolution DCE-MRI datasets.

The separated intravascular signal had to be converted into contrast agent concentration to be used in pharmacokinetic (PK) analysis which was presented in chapter 5 along with the results of using the proposed VIF in PK analysis of a cohort of 28 DCE-MRI datasets of prostate cancer patients.

6.4 Pharmacokinetic analysis

The shape of the time-intensity curves of the intravascular space, calculated using the AC-ICA algorithm, were similar for datasets with different resolutions (as shown in chapter 4). However, when these signals were converted into contrast agent concentration, we observed arbitrary scaling of these curves (shown in chapter 5). A normalization step was introduced in this chapter that normalized the VIF curves with respect to their area under the curve (AUC). This normalization step, in addition to resolving the scaling issue, resulted in

more consistent K^{trans} values and also enabled comparison of AIF-based and VIF-based PK parameters.

The AC-ICA algorithm was applied to DCE-MR images of 27 prostate cancer patients (28 datasets with one patient being imaged twice) and PK analysis was performed using both Tofts-Kety and extended Tofts-Kety models. The PK analysis using extended Tofts-Kety model was performed using two methods:

1-   Method 1 (**m1**): the vascular map from AC-ICA was used as the v_p map, and the $v_p c_p(t)$ term was subtracted from the DCE data. The Tofts-Kety model was then used to calculate the remaining two model parameters

2-   Method 2 (**m2**): all three parameters of the extended Tofts-Kety model were calculated directly by curve fitting using the VIF and tissue curves.

A large artery was also visible in the field of view of the prostate MR images. The concentration-time curve of this artery (Femoral artery) was measured and PK analysis was performed using this AIF signal for both Tofts-Kety model and extended Tofts-Kety model. The results were compared to the results of VIF-based analyses.

Chapter 5 showed that both AIF-based and VIF-based PK analyses resulted in the same average K^{trans} value for normal peripheral zone (PZ) tissue calculated by averaging this parameter across all the datasets that such a tissue was present (20 datasets). It also showed that the VIF-based methods resulted in smaller variation (the variation of VIF-based methods were approximately half of AIF-based methods) in this parameter indicating the better performance of the VIF-based methods (Table 5-1 and Table 5-3). It was also shown that the K^{trans} values that were calculated after normalizing the VIF (or AIF) curves resulted in better separation between the normal PZ tissue and tumor tissue compared to not-normalized curves and also compared to values reported in the literature (Table 5-2 and Table 5-4).

The similarity between the v_p maps calculated using extended Tofts-Kety model and also the v_p map derived directly from AC-ICA, as well as the similarity between the parameters that were reported for the two VIF-based methods showed that the ICA-derived v_p map represented the actual vascular map. Thus, there is no need for modeling to calculate this map which is used in cancer studies as it could be derived from AC-ICA algorithm.

Finally, the effects of decreasing temporal resolution were studied on the performance of both AIF-based and VIF-based methods. The local VIF has a much wider temporal distribution compared to AIF and thus, it was expected to be less sensitive to missing a few frames in its main (FWHM) portion. The VIF is also less sensitive to in-flow effects as it is measured in smaller vessels where the blood flow is slower and also does not suffer from saturation of MR signal due to low contrast agent concentration in every tissue voxel.

The results showed that the VIF-based methods were less sensitive to decreasing the temporal resolution of DCE-MRI data. Thus, it is possible to acquire data with lower temporal resolution and increase the spatial resolution. Increasing the spatial resolution in addition to improving the PK analysis results, improves the accuracy of the AC-ICA algorithm, which could also add to the accuracy of PK parameters.

6.5 Future Directions

This thesis presented a local VIF calculation algorithm and assessed several aspects of it for PK analysis. However, there exist several aspects of the proposed VIF that need to be studied before it could be used in clinical settings or could replace AIF-based analysis. A number of these future directions are given in this section.

6.5.1 Tumor PK assessment

In chapter 5 we studied the performance of the proposed VIF-based analysis on normal PZ tissue in prostate and compared it to the AIF-based PK analysis. However, we were unable to study its performance on tumor tissues using our datasets. Our patient population included different tumor types and tumor locations such that there was not a specific tumor type and location with large enough number of subjects to study the effects of VIF. As the main goal of PK analysis is to study tumors, it is important to conduct numerical and physical tissue-mimicking phantom studies that model prostate tissue and prostate tumor, as well as clinical studies having a larger number of patients with the same tumor type to assess the effects of VIF on PK parameters of the tumor. It is also important to correlate these findings with histology as the ground truth which was not available in our study.

6.5.2 Reproducibility study

Given that the largest differences between the PK parameters of VIF-based and AIF-based studies were in the tumor area, it is important to study the accuracy and reproducibility of

these parameters in the tumor region. Since the VIF is calculated locally and considering the fact that it is biased towards the vascular enhancement of the highly vascular regions in the tissue (which is usually the tumor tissue), it has smaller difference with the actual vascular enhancement of the tumor compared to AIF. Thus, VIF-based PK parameters should be more accurate in tumor region compared to AIF-based parameters. Performing such studies requires more datasets with imaging a patient in several visits which was not possible with our current dataset.

6.5.3 Active surveillance

A major application of PK analysis is in active surveillance studies where the prostate tumor is not treated until it reaches a stage that is life-threatening or would have a significant impact on patient life. The tumor is routinely monitored and its stage is assessed using imaging and biopsy in these studies. Absolute values of PK parameters would be very useful if these parameters could be calculated accurately and such that it could be compared between visits of the patient. Having a local VIF has the potential to be less operator-dependent and might provide more reliable information about the tumor.

6.5.4 Machine learning

Multi-parametric MR imaging of prostate cancer combines the information obtained from several functional and anatomical MR images of the tissue to detect and diagnose the tumor. Recently, machine learning and classification algorithms have been used to obtain maximal information about the tumor which has resulted in very high specificity and sensitivity compared to any single imaging method. Thus, it is important to investigate the effects of using the VIF-based PK parameters in such algorithms and assess their performance, and compare them to the performance of the existing analysis methods in prostate and other organs.

Additionally, we introduced a heuristic criterion for selecting the intravascular components after applying ICA to the data. This step prevented the algorithm from being fully automatic, and also required examining a few datasets to find the time point that the intravascular signal enhancement dropped to 60% of its peak (3 [min] for phantoms and 4.5 [min] for *in vivo* studies). These parameters can be calculated using machine learning algorithm where for each tissue type a number of datasets are used for training and learning the selection criterion, and then used for any new dataset.

6.5.5 Animal studies

A major application of the proposed VIF calculation is in animal tumor studies where a large artery is difficult to find or a very high temporal resolution imaging is needed to capture the first pass of contrast agent bolus (particularly in small animals such as rats). The proposed algorithm could also be used in PK analysis of the organs such as breast in which an artery is not usually available.

6.5.6 Impacts of different spatial and temporal resolutions

In chapter 5 we showed that VIF-based PK analysis is less sensitive to decreasing temporal resolution. This enables acquiring MRI data with higher spatial resolution which should provide more accurate PK parameters, and also more accurate VIF curve as the intravascular and extravascular spaces are better separated. Moreover, it is important to assess the lowest temporal resolution that could be used and still be able to calculate the VIF using ICA and also obtain accurate PK parameters. These effects could be studies using numerical models of the tumor and also conducting clinical studies with higher spatial resolutions.

6.5.7 Adaptive Mag-ICA

In chapter 4 we demonstrated that Mag-ICA was capable of separating the intravascular space but the accuracy of separation was much higher using AC-ICA. One of the shortcomings of Mag-ICA algorithm (compared to AC-ICA algorithm) was using the magnitude of DCE-MRI data which violates the linear mixing assumption in ICA. This effect was minimized by using a short echo time (TE) which reduces the intra-voxel de-phasing and consequently the effects of violating the linear mixture assumption. However, the main difference between the two algorithms was the use of a flexible non-linearity function in the ICA implementation of AC-ICA algorithm. Using a flexible non-linearity function in the Mag-ICA algorithm might improve its results and make it applicable to low resolution clinical datasets. This is an important future direction as most of the currently available DCE-MRI datasets do not have the phase information and thus the AC-ICA algorithm cannot be applied to them. Adapting the algorithm to work with magnitude of MRI data enables the large number of datasets that are already available in clinics to be analyzed, which could answer many of the above mentioned research questions. A good candidate for the adaptive non-linearity function for Mag-ICA is the Rician distribution which has a proper shape for VIF estimation and has several shape parameters that could be used for adapting it to the distribution of the desired MRI signal distribution. Note that keeping the phase information

does not add any extra steps to the acquisition process however such information has to be saved at the time of imaging and cannot be retrieved afterwards.

6.6 Conclusions

Pharmacokinetic modeling of tumor tissue provides information about its perfusion and vascular permeability that can be used for cancer detection and diagnosis. PK analysis requires measuring the intravascular contrast agent concentration which is not possible using the current analysis techniques. Thus, this signal is approximated in a large artery using an AIF. However, using an AIF in addition to requiring a high temporal resolution DCE-MRI data, might lead to error in the calculated PK parameters. Calculating the intravascular contrast agent concentration at the tissue of interest has the potential to improve PK analysis results. This thesis proposed two data-driven techniques based on independent component analysis (ICA) to separate the intravascular contrast agent concentration and calculate the vascular input function (VIF) to be used in PK analysis.

The performances of these two algorithms (Mag-ICA and AC-ICA) were evaluated using numerical and physical phantoms. They were also evaluated using VX2 tumor in rabbits (for Mag-ICA) and prostate cancer (for AC-ICA). The results showed that both algorithms were capable of separating the intravascular signal, however the AC-ICA algorithm provided more accurate VIF curves and was used in subsequent PK analyses.

PK analysis of the prostate DCE-MRI using AC-ICA algorithm resulted in similar results to the PK analysis using the signal of the Femoral artery as the AIF, which shows the VIF could be used in cases an AIF cannot be measured (e.g. small animal studies). Moreover, the VIF-based PK parameters resulted in smaller variation in the normal PZ tissue showing its better performance. Finally, the sensitivity of the VIF-based and AIF-based PK analyses to decreasing temporal resolution was studied, where VIF-based parameters showed smaller sensitivity to this parameter which enables imaging with higher spatial resolution to improve PK analysis results.

References

[1] W. A. Weber, "Assessing tumor response to therapy.," *J. Nucl. Med.*, vol. 50, no. SUPPL. 1, p. 1S–10S, May 2009.

[2] C. H. Lee, L. Braga, R. O. P. de Campos, and R. C. Semelka, "Hepatic tumor response evaluation by MRI.," *NMR Biomed.*, vol. 24, no. 6, pp. 721–33, Jul. 2011.

[3] H. Lilja, D. Ulmert, and A. J. Vickers, "Prostate-specific antigen and prostate cancer: Prediction, detection and monitoring," *Nat. Rev. Cancer*, vol. 8, no. 4, pp. 268–278, 2008.

[4] I. Jacobs, D. Oram, J. Fairbanks, J. Turner, C. Frost, and J. G. Grudzinskas, "A risk of malignancy index incorporating CA 125, ultrasound and menopausal status for the accurate preoperative diagnosis of ovarian cancer," *Br. J. Obstet. Gynaecol.*, vol. 97, no. 10, pp. 922–929, 1990.

[5] E. L. Mazzaferri, R. J. Robbins, C. A. Spencer, L. E. Braverman, F. Pacini, L. Wartofsky, B. R. Haugen, S. I. Sherman, D. S. Cooper, G. D. Braunstein, S. Lee, T. F. Davies, B. M. Arafah, P. W. Ladenson, and A. Pinchera, "A consensus report of the role of serum thyroglobulin as a monitoring method for low-risk patients with papillary thyroid carcinoma," *J. Clin. Endocrinol. Metab.*, vol. 88, no. 4, pp. 1433–1441, 2003.

[6] L. C. Michaelis and M. J. Ratain, "Measuring response in a post-RECIST world: from black and white to shades of grey.," *Nat. Rev. Cancer*, vol. 6, no. 5, pp. 409–14, May 2006.

[7] A. B. Miller, B. Hoogstraten, M. Staquet, and A. Winkler, "Reporting results of cancer treatment," *Cancer*, vol. 47, no. 1, pp. 207–214, 1981.

[8] A. Forner, C. Ayuso, M. Varela, J. Rimola, A. J. Hessheimer, C. R. De Lope, M. Reig, L. Bianchi, J. M. Llovet, and J. Bruix, "Evaluation of tumor response after locoregional therapies in hepatocellular carcinoma: Are response evaluation criteria in solid tumors reliable?," *Cancer*, vol. 115, no. 3, pp. 616–623, 2009.

[9] M. Hutchings and S. F. Barrington, "PET/CT for therapy response assessment in lymphoma," *J. Nucl. Med.*, vol. 50, no. SUPPL. 1, p. 21S–30S, 2009.

[10] H. Choi, H.-J. Yoon, T. S. Kim, J. H. Oh, D. Y. Kim, and S.-K. Kim, "Voxel-based dual-time 18F-FDG parametric imaging for rectal cancer: Differentiation of residual tumor from postchemoradiotherapy changes," *Nucl. Med. Commun.*, vol. 34, no. 12, pp. 1166–1173, 2013.

[11] S. Saracchini, L. Foltran, F. Tuccia, A. Bassini, S. Sulfaro, E. Micheli, A. Del Conte, M. Bertola, M. Gion, M. Lorenzon, and S. Tumolo, "Phase II study of liposome-encapsulated doxorubicin plus cyclophosphamide, followed by sequential trastuzumab

plus docetaxel as primary systemic therapy for breast cancer patients withHER2 overexpression or amplification," *Breast*, vol. 22, no. 6, pp. 1101–1107, 2013.

[12]   M. Van Kruchten, G. A. P. Hospers, A. W. J. M. Glaudemans, H. Hollema, H. J. G. Arts, and A. K. L. Reyners, "Positron emission tomography imaging of oestrogen receptor-expression in endometrial stromal sarcoma supports oestrogen receptor-targeted therapy: Case report and review of the literature," *Eur. J. Cancer*, vol. 49, no. 18, pp. 3850–3855, 2013.

[13]   M. Muzi, F. O'Sullivan, D. a Mankoff, R. K. Doot, L. a Pierce, B. F. Kurland, H. M. Linden, and P. E. Kinahan, "Quantitative assessment of dynamic PET imaging data in cancer imaging.," *Magn. Reson. Imaging*, vol. 30, no. 9, pp. 1203–15, Nov. 2012.

[14]   J. M. Hudson, R. Williams, R. Karshafian, L. Milot, M. Atri, P. N. Burns, and G. A. Bjarnason, "Quantifying vascular heterogeneity using microbubble disruption-replenishment kinetics in patients with renal cell cancer," *Investigative Radiology*. 2013.

[15]   J. H. Naish, D. M. McGrath, L. J. Bains, K. Passera, C. Roberts, Y. Watson, S. Cheung, M. B. Taylor, J. P. Logue, D. L. Buckley, J. Tessier, H. Young, J. C. Waterton, and G. J. M. Parker, "Comparison of dynamic contrast-enhanced MRI and dynamic contrast-enhanced CT biomarkers in bladder cancer," *Magn. Reson. Med.*, vol. 66, no. 1, pp. 219–226, 2011.

[16]   D. A. Hamstra, A. Rehemtulla, and B. D. Ross, "Diffusion magnetic resonance imaging: A biomarker for treatment response in oncology," *J. Clin. Oncol.*, vol. 25, no. 26, pp. 4104–4109, 2007.

[17]   J. J. Smith, A. G. Sorensen, and J. H. Thrall, "Biomarkers in imaging: Realizing radiology's future," *Radiology*, vol. 227, no. 3, pp. 633–638, 2003.

[18]   N. Hylton, "Dynamic contrast-enhanced magnetic resonance imaging as an imaging biomarker," *J. Clin. Oncol.*, vol. 24, no. 20, pp. 3293–3298, 2006.

[19]   National Cancer Institute, "Defining Cancer." [Online]. Available: http://www.cancer.gov/cancertopics/cancerlibrary/what-is-cancer. [Accessed: 06-Aug-2013].

[20]   D. Hanahan, R. A. Weinberg, and S. Francisco, "The Hallmarks of Cancer Review University of California at San Francisco," vol. 100, pp. 57–70, 2000.

[21]   D. Hanahan and R. a Weinberg, "Hallmarks of cancer: the next generation.," *Cell*, vol. 144, no. 5, pp. 646–74, Mar. 2011.

[22]   National Cancer Institute, "Tumor Microenvironment." [Online]. Available: http://www.cancer.gov/dictionary?cdrid=561725.

[23]   National Cancer Institute, "NCI Dictionary of Cancer Terms: Biomarker." [Online]. Available: http://www.cancer.gov/dictionary/?CdrID=45618. [Accessed: 06-Aug-2013].

[24]   A. Mishra and M. Verma, "Cancer Biomarkers: Are We Ready for the Prime Time?," *Cancers (Basel).*, vol. 2, no. 1, pp. 190–208, Mar. 2010.

[25]   R. F. Tuma, W. N. Duran, and K. Jey, Eds., *Microcirculation*, 2nd ed. Academic Press, 2011, p. 1000.

[26]   P. Carmeliet and R. K. Jain, "Molecular mechanisms and clinical applications of angiogenesis," *Nature*, vol. 473, no. 7347. pp. 298–307, 2011.

[27]   R. K. Jain, "Determinants of tumor blood flow: A review," *Cancer Research*, vol. 48, no. 10. pp. 2641–2658, 1988.

[28]   J. Folkman, "Tumor angiogenesis: therapeutic implications.," *New England Journal of Medicine*, vol. 285, no. 21. pp. 1182–1186, 1971.

[29]   P. M. Gullino, "Angiogenesis and oncogenesis," *Journal of the National Cancer Institute*, vol. 61, no. 3. pp. 639–643, 1978.

[30]   A. M. Jubb, H. I. Hurwitz, W. Bai, E. B. Holmgren, P. Tobin, A. S. Guerrero, F. Kabbinavar, S. N. Holden, W. F. Novotny, G. D. Frantz, K. J. Hillan, and H. Koeppen, "Impact of vascular endothelial growth factor-A expression, thrombospondin-2 expression, and microvessel density on the treatment effect of bevacizumab in metastatic colorectal cancer," *Journal of Clinical Oncology*, vol. 24, no. 2. pp. 217–227, 2006.

[31]   R. Mazzieri, F. Pucci, D. Moi, E. Zonari, A. Ranghetti, A. Berti, L. Politi, B. Gentner, J. Brown, L. Naldini, and M. De Palma, "Targeting the ANG2/TIE2 Axis Inhibits Tumor Growth and Metastasis by Impairing Angiogenesis and Disabling Rebounds of Proangiogenic Myeloid Cells," *Cancer Cell*, vol. 19, no. 4. pp. 512–526, 2011.

[32]   G. L. Semenza, "HIF-1: upstream and downstream of cancer metabolism," *Current Opinion in Genetics and Development*, vol. 20, no. 1. pp. 51–56, 2010.

[33]   N. Ferrara, "Vascular endothelial growth factor," *Arteriosclerosis, Thrombosis, and Vascular Biology*, vol. 29, no. 6. pp. 789–791, 2009.

[34]   R. Virmani, F. D. Kolodgie, A. P. Burke, A. V Finn, H. K. Gold, T. N. Tulenko, S. P. Wrenn, and J. Narula, "Atherosclerotic plaque progression and vulnerability to rupture: Angiogenesis as a source of intraplaque hemorrhage," *Arteriosclerosis, Thrombosis, and Vascular Biology*, vol. 25, no. 10. pp. 2054–2061, 2005.

[35]   E. Dejana, E. Tournier-Lasserve, and B. M. Weinstein, "The Control of Vascular Integrity by Endothelial Cell Junctions: Molecular Basis and Pathological Implications," *Developmental Cell*, vol. 16, no. 2. pp. 209–221, 2009.

[36]   S. Hern and P. S. Mortimer, "In vivo quantification of microvessels in clinically uninvolved psoriatic skin and in normal skin," *British Journal of Dermatology*, vol. 156, no. 6. pp. 1224–1229, 2007.

[37]   R. K. Jain, "Molecular regulation of vessel maturation," *Nature Medicine*, vol. 9, no. 6. pp. 685–693, 2003.

[38] J. W. Baish and R. K. Jain, "Fractals and cancer," *Cancer Research*, vol. 60, no. 14. pp. 3683–3688, 2000.

[39] J. R. Less, M. C. Posner, Y. Boucher, D. Borochovitz, N. Wolmark, and R. K. Jain, "Interstitial hypertension in human breast and colorectal tumors," *Cancer Research*, vol. 52, no. 22. pp. 6371–6374, 1992.

[40] T. Nakahara, S. M. Norberg, D. R. Shalinsky, D. D. Hu-Lowe, and D. M. McDonald, "Effect of inhibition of vascular endothelial growth factor signaling on distribution of extravasated antibodies in tumors," *Cancer Research*, vol. 66, no. 3. pp. 1434–1445, 2006.

[41] P. Vaupel, "Tumor microenvironmental physiology and its implications for radiation oncology.," *Semin. Radiat. Oncol.*, vol. 14, no. 3, pp. 198–206, Jul. 2004.

[42] N. Pore, Z. Jiang, A. Gupta, G. Cerniglia, G. D. Kao, and A. Maity, "EGFR tyrosine kinase inhibitors decrease VEGF expression by both hypoxia-inducible factor (HIF)-1-independent and HIF-1-dependent mechanisms," *Cancer Research*, vol. 66, no. 6. pp. 3197–3204, 2006.

[43] A. R. Pries, A. J. M. Cornelissen, A. A. Sloot, M. Hinkeldey, M. R. Dreher, M. Höpfner, M. W. Dewhirst, and T. W. Secomb, "Structural adaptation and heterogeneity of normal and tumor microvascular networks," *PLoS Computational Biology*, vol. 5, no. 5. 2009.

[44] T. P. Pader, A. H. Kuo, T. Hoshida, S. Liao, J. Lobo, K. R. Kozak, D. Fukumura, and R. K. Jain, "Differential response of primary tumor versus lymphatic metastasis to VEGFR-2 and VEGFR-3 kinase inhibitors cediranib and vandetanib," *Molecular Cancer Therapeutics*, vol. 7, no. 8. pp. 2272–2279, 2008.

[45] G. Helmlinger, F. Yuan, M. Dellian, and R. K. Jain, "Interstitial pH and pO2 gradients in solid tumors in vivo: High-resolution measurements reveal a lack of correlation," *Nature Medicine*, vol. 3, no. 2. pp. 177–182, 1997.

[46] D. P. Bottaro and L. A. Liotta, "Out of air is not out of action," *Nature*, vol. 423, no. 6940. pp. 593–595, 2003.

[47] J. C. Waterton and D. Ph, "What imaging biomarkers are and how they are used John Waterton ISMRM Honolulu April 2008," no. April, pp. 104–107, 2008.

[48] R. D. Sriram, "Imaging as a Biomarker : Standards for Change Measurements in Therapy Workshop Summary Imaging as a Biomarker : Standards for Change Measurements in Therapy Workshop Summary," 2006.

[49] E. A. Handorf, S. McElligott, A. Vachani, C. J. Langer, M. B. Demeter, K. Armstrong, and D. A. Asch, "Cost effectiveness of personalized therapy for first-line treatment of stage IV and recurrent incurable adenocarcinoma of the lung," *J. Oncol. Pract.*, vol. 8, no. 5, pp. 267–274, 2012.

[50] World Health Organization, *WHO Handbook for Reporting Results of Cancer Treatment*, Offset Pub. Geneva: World Health Organization, 1979.

[51] P. Therasse, S. G. Arbuck, E. A. Eisenhauer, J. Wanders, R. S. Kaplan, L. Rubinstein, J. Verweij, M. Van Glabbeke, T. Van Oosterom, M. C. Christian, and S. G. Gwyther, "New Guidelines to Evaluate the Response to Treatment," vol. 92, no. 3, 2000.

[52] M. R. Sharma, M. L. Maitland, and M. J. Ratain, "RECIST: no longer the sharpest tool in the oncology clinical trials toolbox," *Cancer Res.*, vol. 72, no. 20, pp. 5145–9; discussion 5150, Oct. 2012.

[53] B. Escudier, T. Eisen, W. M. Stadler, C. Szczylik, S. Oudard, M. Siebels, S. Negrier, C. Chevreau, E. Solska, A. A. Desai, F. Rolland, T. Demkow, T. E. Hutson, M. Gore, S. Freeman, B. Schwartz, M. Shan, R. Simantov, and R. M. Bukowski, "Sorafenib in advanced clear-cell renal-cell carcinoma," *N. Engl. J. Med.*, vol. 356, no. 2, pp. 125–134, 2007.

[54] E. Van Cutsem, M. Peeters, S. Siena, Y. Humblet, A. Hendlisz, B. Neyns, J.-L. Canon, J.-L. Van Laethem, J. Maurel, G. Richardson, M. Wolf, and R. G. Amado, "Open-label phase III trial of panitumumab plus best supportive care compared with best supportive care alone in patients with chemotherapy- refractory metastatic colorectal cancer," *J. Clin. Oncol.*, vol. 25, no. 13, pp. 1658–1664, 2007.

[55] E. Raymond, L. Dahan, J.-L. Raoul, Y.-J. Bang, I. Borbath, C. Lombard-Bohas, J. Valle, P. Metrakos, D. Smith, A. Vinik, J.-S. Chen, D. Hörsch, P. Hammel, B. Wiedenmann, E. Van Cutsem, S. Patyna, D. R. Lu, C. Blanckmeister, R. Chao, and P. Ruszniewski, "Sunitinib malate for the treatment of pancreatic neuroendocrine tumors," *N. Engl. J. Med.*, vol. 364, no. 6, pp. 501–513, 2011.

[56] C. L. Mitchell, J. P. B. O'Connor, C. Roberts, Y. Watson, a Jackson, S. Cheung, J. Evans, J. Spicer, a Harris, C. Kelly, S. Rudman, M. Middleton, a Fielding, J. Tessier, H. Young, G. J. M. Parker, and G. C. Jayson, "A two-part phase II study of cediranib in patients with advanced solid tumours: the effect of food on single-dose pharmacokinetics and an evaluation of safety, efficacy and imaging pharmacodynamics.," *Cancer Chemother. Pharmacol.*, vol. 68, no. 3, pp. 631–41, Sep. 2011.

[57] F. Ng, R. Kozarski, B. Ganeshan, and V. Goh, "Assessment of tumor heterogeneity by CT texture analysis: Can the largest cross-sectional area be used as an alternative to whole tumor analysis?," *Eur. J. Radiol.*, vol. 82, no. 2, pp. 342–348, 2013.

[58] K. A. Miles, "Perfusion imaging with computed tomography: Brain and beyond," *Eur. Radiol. Suppl.*, vol. 16, no. 7, pp. M37–M43, 2006.

[59] R. K. Doot, M. Muzi, L. M. Peterson, E. K. Schubert, J. R. Gralow, J. M. Specht, and D. a Mankoff, "Kinetic analysis of 18F-fluoride PET images of breast cancer bone metastases.," *J. Nucl. Med.*, vol. 51, no. 4, pp. 521–7, Apr. 2010.

[60] E. J. Feleppaa, J. Mamoua, C. R. Porterb, and J. Machic, "Quantitative Ultrasound in Cancer Imaging," *Semin. Oncol.*, vol. 38, no. 1, pp. 136–150, 2012.

[61] B. E. Van Beers and V. Vilgrain, "Biomarkers in abdominal imaging," *Abdominal Imaging*, vol. 34, no. 6. pp. 663–667, 2009.

[62] H. W. M. van Laarhoven, D. W. J. Klomp, M. Rijpkema, Y. L. M. Kamm, D. J. T. Wagener, J. O. Barentsz, C. J. A. Punt, and A. Heerschap, "Prediction of chemotherapeutic response of colorectal liver metastases with dynamic gadolinium-DTPA-enhanced MRI and localized 19F MRS pharmacokinetic studies of 5-fluorouracil," *NMR in Biomedicine*, vol. 20, no. 2. pp. 128–140, 2007.

[63] M.-F. Bellin and A. J. Van Der Molen, "Extracellular gadolinium-based contrast media: An overview," *Eur. J. Radiol.*, vol. 66, no. 2, pp. 160–167, 2008.

[64] J. P. B. O'Connor, A. Jackson, G. J. M. Parker, C. Roberts, and G. C. Jayson, "Dynamic contrast-enhanced MRI in clinical trials of antivascular therapies.," *Nat. Rev. Clin. Oncol.*, vol. 9, no. 3, pp. 167–77, Mar. 2012.

[65] N. Ferrara, "Vascular endothelial growth factor: Molecular and biological aspects," *Current Topics in Microbiology and Immunology*, vol. 237. pp. 1–30, 1999.

[66] M. Kanematsu, S. Osada, N. Amaoka, S. Goshima, H. Kondo, H. Kato, H. Nishibori, R. Yokoyama, H. Hoshi, and N. Moriyama, "Expression of vascular endothelial growth factor in hepatocellular carcinoma and the surrounding liver and correlation with MRI findings," *Am. J. Roentgenol.*, vol. 184, no. 3, pp. 832–841, 2005.

[67] J. A. Jacquez, *Compartmental Analysis in Biology and Medicine*, 2nd ed. AnnArbor,MI: University of Michigan Press, 1985.

[68] W. Perl, N. A. Lassen, and R. M. Effros, "Matrix proof of flow, volume and mean transit time theorems for regional and compartmental systems," *Bulletin of Mathematical Biology*, vol. 37, no. 6. pp. 573–588, 1975.

[69] N. A. Lassen and W. Perl, *Tracer Kinetic Methods in Medical Physiology*. New York: Raven Press, 1979.

[70] S. P. Sourbron and D. L. Buckley, "Tracer kinetic modelling in MRI: estimating perfusion and capillary permeability.," *Phys. Med. Biol.*, vol. 57, no. 2, pp. R1–33, Jan. 2012.

[71] P. S. Tofts, "Modeling tracer kinetics in dynamic Gd-DTPA MR imaging," *J. Magn. Reson. Imaging*, vol. 7, no. 1, pp. 91–101, 1997.

[72] P. S. Tofts, G. Brix, D. L. Buckley, J. L. Evelhoch, E. Henderson, M. V Knopp, H. B. W. Larsson, T. Y. Lee, N. A. Mayr, G. J. M. Parker, R. E. Port, J. Taylor, and R. M. Weisskoff, "Estimating kinetic parameters from dynamic contrast-enhanced T-1-weighted MRI of a diffusable tracer: Standardized quantities and symbols," *J. Magn. Reson. Imaging*, vol. 10, no. 3, pp. 223–232, Sep. 1999.

[73] J. A. Johnson and T. A. Wilson, "A model for capillary exchange.," *The American journal of physiology*, vol. 210, no. 6. pp. 1299–1303, 1966.

[74] K. S. St Lawrence and T. Y. Lee, "An adiabatic approximation to the tissue homogeneity model for water exchange in the brain: I. Theoretical derivation," *J. Cereb. Blood Flow Metab.*, vol. 18, no. 12, pp. 1365–1377, Dec. 1998.

[75]   W. C. Sangren and C. W. Sheppard, "A mathematical derivation of the exchange of a labeled substance between a liquid flowing in a vessel and an external compartment," *The Bulletin of Mathematical Biophysics*, vol. 15, no. 4. pp. 387–394, 1953.

[76]   A. R. Padhani, C. Hayes, S. Landau, and M. O. Leach, "Reproducibility of quantitative dynamic MRI of normal human tissues," *NMR in Biomedicine*, vol. 15, no. 2. pp. 143–153, 2002.

[77]   P. L. Choyke, A. J. Dwyer, and M. V Knopp, "Functional tumor imaging with dynamic contrast-enhanced magnetic resonance imaging," *Journal of Magnetic Resonance Imaging*, vol. 17, no. 5. pp. 509–520, 2003.

[78]   D. J. Covarrubias, B. R. Rosen, and M. H. Lev, "Dynamic magnetic resonance perfusion imaging of brain tumors," *Oncologist*, vol. 9, no. 5. pp. 528–537, 2004.

[79]   M. O. Leach, K. M. Brindle, J. L. Evelhoch, J. R. Griffiths, M. R. Horsman, A. Jackson, G. C. Jayson, I. R. Judson, M. V Knopp, R. J. Maxwell, D. McIntyre, A. R. Padhani, P. Price, R. Rathbone, G. J. Rustin, P. S. Tofts, G. M. Tozer, W. Vennart, J. C. Waterton, S. R. Williams, and P. Workman, "The assessment of antiangiogenic and antivascular therapies in early-stage clinical trials using magnetic resonance imaging: Issues and recommendations," *British Journal of Cancer*, vol. 92, no. 9. pp. 1599–1610, 2005.

[80]   J. P. O'Connor, A. Jackson, M.-C. Asselin, D. L. Buckley, G. J. Parker, and G. C. Jayson, "Quantitative imaging biomarkers in the clinical development of targeted therapeutics: current and future perspectives," *The Lancet Oncology*, vol. 9, no. 8. pp. 766–776, 2008.

[81]   M. O. Leach, "Assessment of antiangiogenic and antivascular therapeutics using MRI: recommendations for appropriate methodology for clinical trials," *Br. J. Radiol.*, vol. 76, no. suppl_1, pp. S87–S91, Dec. 2003.

[82]   D. M. McGrath, D. P. Bradley, J. L. Tessier, T. Lacey, C. J. Taylor, and G. J. M. Parker, "Comparison of Model-Based Arterial Input Functions for Dynamic Contrast-Enhanced MRI in Tumor Bearing Rats," *Magn. Reson. Med.*, vol. 61, no. 5, pp. 1173–1184, 2009.

[83]   R. Lawaczeck, G. Jost, and H. Pietsch, "Pharmacokinetics of Contrast Media in Humans Model With Circulation, Distribution, and Renal Excretion," *Invest. Radiol.*, vol. 46, no. 9, pp. 576–585, Sep. 2011.

[84]   A. Shukla-Dave, N. Lee, H. Stambuk, Y. Wang, W. Huang, H. T. Thaler, S. G. Patel, J. P. Shah, and J. a Koutcher, "Average arterial input function for quantitative dynamic contrast enhanced magnetic resonance imaging of neck nodal metastases.," *BMC Med. Phys.*, vol. 9, p. 4, Jan. 2009.

[85]   Y. Yu, Q. Jiang, Y. Miao, J. Li, S. Bao, H. Wang, C. Wu, X. Wang, J. Zhu, Y. Zhong, E. M. Haacke, and J. Hu, "Quantitative analysis of clinical dynamic contrast-enhanced MR imaging for evaluating treatment response in human breast cancer," *Radiology*, vol. 257, no. 1, pp. 47–55, 2010.

[86] Y. Wang, W. Huang, D. A. Panicek, L. H. Schwartz, and J. A. Koutcher, "Feasibility of using limited-population-based arterial input function for pharmacokinetic modeling of osteosarcoma dynamic contrast-enhanced MRI data," *Magn. Reson. Med.*, vol. 59, no. 5, pp. 1183–1189, 2008.

[87] J. Moroz, C. L. Wong, A. C. Yung, P. Kozlowski, and S. a Reinsberg, "Rapid measurement of arterial input function in mouse tail from projection phases.," *Magn. Reson. Med.*, vol. 000, pp. 1–8, Feb. 2013.

[88] P. S. Tofts and A. G. Kermode, "Measurement of the Blood-Brain-Barrier Permeability and Leakage Space using Dynamic Mr Imaging .1. Fundamental-Concepts," *Magn. Reson. Med.*, vol. 17, no. 2, pp. 357–367, 1991.

[89] G. Brix, W. Semmler, R. Port, L. R. Schad, G. Layer, and W. J. Lorenz, "Pharmacokinetic Parameters in Cns Gd-Dtpa Enhanced Mr Imaging," *J. Comput. Assist. Tomogr.*, vol. 15, no. 4, pp. 621–628, 1991.

[90] H. J. Weinmann, M. Laniado, and W. Mutzel, "Pharmacokinetics of Gddtpa Dimeglumine After Intravenous-Injection into Healthy-Volunteers," *Physiol. Chem. Phys. Med. NMR*, vol. 16, no. 2, pp. 167–172, 1984.

[91] X. Fan, C. R. Haney, D. Mustafi, C. Yang, M. Zamora, E. J. Markiewicz, and G. S. Karczmar, "Use of a Reference Tissue and Blood Vessel to Measure the Arterial Input Function in DCEMRI," *Magn. Reson. Med.*, vol. 64, no. 6, pp. 1821–1826, Dec. 2010.

[92] L. E. Kershaw and H.-L. M. Cheng, "A general dual-bolus approach for quantitative DCE-MRI.," *Magn. Reson. Imaging*, vol. 29, no. 2, pp. 160–6, Feb. 2011.

[93] J. G. Korporaal, M. van Vulpen, C. a T. van den Berg, and U. a van der Heide, "Tracer kinetic model selection for dynamic contrast-enhanced computed tomography imaging of prostate cancer.," *Invest. Radiol.*, vol. 47, no. 1, pp. 41–8, Jan. 2012.

[94] B. C. MOORE, "Principal Component Analysis in Linear-Systems - Controllability, Observability, and Model-Reduction," *IEEE Trans. Automat. Contr.*, vol. 26, no. 1, pp. 17–32, 1981.

[95] D. D. Lee and H. S. Seung, "Learning the parts of objects by non-negative matrix factorization," *Nature*, vol. 401, no. 6755, pp. 788–791, 1999.

[96] A. L. Martel, S. J. Allder, G. S. Delay, P. S. Morgan, and A. R. Moody, "Perfusion MRI of infarcted and noninfarcted brain tissue in stroke: A comparison of conventional hemodynamic imaging and factor analysis of dynamic studies," *Invest. Radiol.*, vol. 36, no. 7, pp. 378–385, 2001.

[97] H. Mehrabian, L. Lindvere, B. Stefanovic, and A. L. Martel, "A constrained independent component analysis technique for artery-vein separation of two-photon laser scanning microscopy images of the cerebral microvasculature," *Med. Image Anal.*, vol. 16, no. 1, pp. 239–251, 2012.

[98] P. Comon, "Independent component analysis, A new concept?," *Signal Processing*, vol. 36, no. 3, pp. 287–314, 1994.

[99] F. Calamante, M. Mørup, and L. K. Hansen, "Defining a local arterial input function for perfusion MRI using independent component analysis," *Magn. Reson. Med.*, vol. 52, no. 4, pp. 789–797, 2004.

[100] X. Y. Wu and G. R. Liu, "Application of independent component analysis to dynamic contrast-enhanced imaging for assessment of cerebral blood perfusion," *Med. Image Anal.*, vol. 11, no. 3, pp. 254–265, 2007.

[101] R. E. Hendrick and E. M. Haacke, "Basic physics of MR contrast agents and maximization of image contrast.," *J. Magn. Reson. Imaging*, vol. 3, no. 1, pp. 137–148, 1993.

[102] J. E. McNeal, "Normal histology of the prostate," *Am. J. Surg. Pathol.*, vol. 12, no. 8, pp. 619–633, 1988.

[103] J. E. McNeal, E. A. Redwine, F. S. Freiha, and T. A. Stamey, "Zonal distribution of prostatic adenocarcinoma. Correlation with histologic pattern and direction of spread," *Am. J. Surg. Pathol.*, vol. 12, no. 12, pp. 897–906, 1988.

[104] V. Kundra, P. M. Silverman, S. F. Matin, and H. Choi, "Imaging in oncology from the University of Texas M. D. Anderson Cancer Center: diagnosis, staging, and surveillance of prostate cancer.," *Am. J. Roentgenol.*, vol. 189, no. 4, pp. 830–44, Oct. 2007.

[105] R. S. Snell, *Clinical Anatomy*, 7th ed. Lippincott Williams and Wilkins, 2004, p. 1012.

[106] F. V Coakley and H. Hricak, "Radiologic anatomy of the prostate gland: A clinical approach," *Radiol. Clin. North Am.*, vol. 38, no. 1, pp. 15–30, 2000.

[107] J. Ramon and L. J. Denis, Eds., *Prostate Cancer*. New York: Springer - Verlag Berlin Heidelberg, 2007.

[108] D. M. Parkin, F. Bray, J. Ferlay, and P. Pisani, "Global cancer statistics, 2002," *Ca-A Cancer J. Clin.*, vol. 55, no. 2, pp. 74–108, 2005.

[109] K. J. Pienta and P. S. Esper, "Risk factors for prostate cancer," *Ann. Intern. Med.*, vol. 118, no. 10, pp. 793–803, 1993.

[110] G. Cancel-Tassin and O. Cussenot, "Prostate cancer genetics," *Minerva Urol. e Nefrol.*, vol. 57, no. 4, pp. 289–300, 2005.

[111] J. L. Stanford, J. E. Damber, W. R. Fair, H. Sancho-Garnier, K. Griffiths, and F. L. Gu, "Epidemiology of prostate cancer," in *2nd International Consultation on Pros- tate Cancer*, 1999, pp. 23–55.

[112] F. H. Martini, *Fundamentals of Anatomy and Physiology*, 4th ed. upper Saddle River, NJ: Prentice Hall, 1998.

[113] V. M. Velonas, H. H. Woo, C. G. dos Remedios, and S. J. Assinder, "Current status of biomarkers for prostate cancer," *Int. J. Mol. Sci.*, vol. 14, no. 6, pp. 11034–11060, 2013.

[114] S. Egawa, D. R. Greene, W. F. Flanagan, T. M. Wheeler, and P. T. Scardino, "Transrectal ultrasonography in stage a prostate cancer: Detection of residual tumor after transurethral resection of prostate," *J. Urol.*, vol. 146, no. 2, pp. 366–371, 1991.

[115] C. M. A. Hoeks, J. O. Barentsz, T. Hambrock, D. Yakar, D. M. Somford, S. W. T. P. J. Heijmink, T. W. J. Scheenen, P. C. Vos, H. Huisman, I. M. Van Oort, J. A. Witjes, A. Heerschap, and J. J. Fütterer, "Prostate cancer: Multiparametric MR imaging for detection, localization, and staging," *Radiology*, vol. 261, no. 1, pp. 46–66, 2011.

[116] R. J. Bast, D. Kufe, R. Pollock, R. Weichselbaum, J. Holland, and E. Frei, Eds., *Holland-Frei Cancer Medicine*, 5th ed. Hamilton (ON): BC Decker, 2000.

[117] M. T. Carriaga and D. E. Henson, "The histologic grading of cancer," *Cancer*, vol. 75, no. 1 SUPPL., pp. 406–421, 1995.

[118] D. F. Gleason, "histologic grading and clinical staging of prostatic carcinoma," in *Urologic Pathology: The Prostate*, M. Tannenbaum, Ed. Philadelphia: Lea & Febiger, 1977, p. 419.

[119] D. F. Gleason, "Classification of prostatic carcinomas.," *Cancer Chemother. Rep.*, vol. 50, no. 3, pp. 125–128, 1966.

[120] A. Wall, T. Persigehl, P. Hauff, K. Licha, M. Schirner, S. Müller, A. von Wallbrunn, L. Matuszewski, W. Heindel, and C. Bremer, "Differentiation of angiogenic burden in human cancer xenografts using a perfusion-type optical contrast agent (SIDAG)," *Breast Cancer Res.*, vol. 10, no. 2, 2008.

[121] T. S. Koh, S. Hartono, C. H. Thng, T. K. H. Lim, L. Martarello, and Q. S. Ng, "In vivo measurement of gadolinium diffusivity by dynamic contrast-enhanced MRI: A preclinical study of human xenografts," *Magn. Reson. Med.*, vol. 69, no. 1, pp. 269–276, 2013.

[122] J. R. Jones, D. L. G. Rowlands, and C. B. Monk, "Diffusion coefficient of water in water and in some alkaline earth chloride solutions at 25°C," *Trans. Faraday Soc.*, vol. 61, pp. 1384–1388, 1965.

[123] H. Benoit-Cattin, G. Collewet, B. Belaroussi, H. Saint-Jalmes, and C. Odet, "The SIMRI project: a versatile and interactive MRI simulator.," *J. Magn. Reson.*, vol. 173, no. 1, pp. 97–115, Mar. 2005.

[124] P. Latta, M. L. H. Gruwel, V. Jellúš, and B. Tomanek, "Bloch simulations with intra-voxel spin dephasing," *J. Magn. Reson.*, vol. 203, no. 1, pp. 44–51, 2010.

[125] L. Cochlin, A. Blamire, and P. Styles, "Dependence of T1 and T2 on high field strengths in doped agarose gels; facilitating selection of com- position for specific T1/T2 at relevant field," in *International Society of Magnetic Resonance in Medicine*, 2003, p. 885.

[126] I. Pang, "Design and Characterization of a multi-modality phantom for contrast enhanced ultrasound and magnetic resonance imaging," University of Toronto, 2011.

[127] W. A. Ritschel and G. L. Kearns, *Handbook of Basic Pharmacokinetics-- Including Clinical Applications* . Washington, D.C.: American Pharmaceutical Association, 1999.

[128] C. Chandrana, P. Bevan, J. Hudson, I. Pang, P. Burns, D. Plewes, and R. Chopra, "Development of a platform for co-registered ultrasound and MR contrast imaging in vivo," *Phys. Med. Biol.*, vol. 56, no. 3, pp. 861–877, 2011.

[129] L. Curiel, Y. Huang, N. Vykhodtseva, and K. Hynynen, "Focused ultrasound treatment of VX2 tumors controlled by local harmonic motion," *Phys. Med. Biol.*, vol. 54, no. 11, pp. 3405–3419, 2009.

[130] L. Curiel, R. Chopra, and K. Hynynen, "Progress in multimodality imaging: Truly simultaneous ultrasound and magnetic resonance imaging," *IEEE Transactions on Medical Imaging*, vol. 26, no. 12. pp. 1740–1747, 2007.

[131] M. Viallon, S. Terraz, J. Roland, E. Dumont, C. D. Becker, and R. Salomir, "Observation and correction of transient cavitation-induced PRFS thermometry artifacts during radiofrequency ablation, using simultaneous Ultrasound/MR imaging," *Medical Physics*, vol. 37, no. 4. pp. 1491–1506, 2010.

[132] S. R. Wilson, L. D. Greenbaum, and B. B. Goldberg, "Contrast-enhanced ultrasound: what is the evidence and what are the obstacles?," *AJR. Am. J. Roentgenol.*, vol. 193, no. 1, pp. 55–60, Jul. 2009.

[133] C. Greis, "Ultrasound contrast agents as markers of vascularity and microcirculation," *Clin. Hemorheol. Microcirc.*, vol. 43, no. 1–2, pp. 1–9, 2009.

[134] F. Stuart Foster, P. N. Burns, D. H. Simpson, S. R. Wilson, D. A. Christopher, and D. E. Goertz, "Ultrasound for the visualization and quantification of tumor microcirculation," *Cancer Metastasis Rev.*, vol. 19, no. 1–2, pp. 131–138, 2000.

[135] R. Williams, J. M. Hudson, B. A. Lloyd, A. R. Sureshkumar, G. Lueck, L. Milot, M. Atri, G. A. Bjarnason, and P. N. Burns, "Dynamic microbubble contrast-enhanced US to measure tumor response to targeted therapy: A proposed clinical protocol with results from renal cell carcinoma patients receiving antiangiogenic therapy," *Radiology*, vol. 260, no. 2, pp. 581–590, 2011.

[136] H. Hricak, R. D. Williams, D. B. Spring, K. L. Moon Jr., M. W. Hedgcock, R. A. Watson, and L. E. Crooks, "Anatomy and pathology of the male pelvis by magnetic resonance imaging," *American Journal of Roentgenology*, vol. 141, no. 6. pp. 1101–1110, 1983.

[137] J. H. Steyn and F. W. Smith, "Nuclear magnetic resonance imaging of the prostate," *British Journal of Urology*, vol. 54, no. 6. pp. 726–728, 1982.

[138] H. Hricak, G. C. Dooms, J. E. McNeal, A. S. Mark, M. Marotti, A. Avallone, M. Pelzer, E. C. Proctor, and E. A. Tanagho, "MR imaging of the prostate gland: Normal anatomy," *American Journal of Roentgenology*, vol. 148, no. 1. pp. 51–58, 1987.

[139] L. Wang, Y. Mazaheri, J. Zhang, N. M. Ishill, K. Kuroiwa, and H. Hricak, "Assessment of biologic aggressiveness of prostate cancer: Correlation of MR signal intensity with gleason grade after radical prostatectomy," *Radiology*, vol. 246, no. 1. pp. 168–176, 2008.

[140] O. Akin, E. Sala, C. S. Moskowitz, K. Kuroiwa, N. M. Ishill, D. Pucar, P. T. Scardino, and H. Hricak, "Transition zone prostate cancers: Features, detection, localization, and staging at endorectal MR imaging," *Radiology*, vol. 239, no. 3. pp. 784–792, 2006.

[141] A. P. S. Kirkham, M. Emberton, and C. Allen, "How Good is MRI at Detecting and Characterising Cancer within the Prostate?," *European Urology*, vol. 50, no. 6. pp. 1163–1175, 2006.

[142] E. O. Stejskal and J. E. Tanner, "Spin diffusion measurements: Spin echoes in the presence of a time-dependent field gradient," *The Journal of Chemical Physics*, vol. 42, no. 1. pp. 288–292, 1965.

[143] M. A. Jacobs, R. Ouwerkerk, K. Petrowski, and K. J. MacUra, "Diffusion-weighted imaging with apparent diffusion coefficient mapping and spectroscopy in prostate cancer," *Topics in Magnetic Resonance Imaging*, vol. 19, no. 6. pp. 261–272, 2008.

[144] D. Le Bihan, E. Breton, D. Lallemand, M.-L. Aubin, J. Vignaud, and M. Laval-Jeantet, "separation of diffusion and perfusion in intravoxel incoherent motion MR imaging," *Radiology*, vol. 168, no. 2, pp. 497–505, 1988.

[145] K. Katahira, T. Takahara, T. C. Kwee, S. Oda, Y. Suzuki, S. Morishita, K. Kitani, Y. Hamada, M. Kitaoka, and Y. Yamashita, "Ultra-high-b-value diffusion-weighted MR imaging for the detection of prostate cancer: Evaluation in 201 cases with histopathological correlation," *European Radiology*, vol. 21, no. 1. pp. 188–196, 2011.

[146] K. Hosseinzadeh and S. D. Schwarz, "Endorectal diffusion-weighted imaging in prostate cancer to differentiate malignant and benign peripheral zone tissue," *Journal of Magnetic Resonance Imaging*, vol. 20, no. 4. pp. 654–661, 2004.

[147] A. R. Padhani, "Dynamic contrast-enhanced MRI in clinical oncology: Current status and future directions," *J. Magn. Reson. Imaging*, vol. 16, no. 4, pp. 407–422, 2002.

[148] G. J. Jager, E. T. G. Ruijter, C. A. Van De Kaa, J. J. M. C. H. De La Rosette, G. O. N. Oosterhof, J. R. Thornbury, and J. O. Barentsz, "Local staging of prostate cancer with endorectal MR imaging: Correlation with histopathology," *American Journal of Roentgenology*, vol. 166, no. 4. pp. 845–852, 1996.

[149] F. Calamante, M. Mørup, and L. K. Hansen, "Defining a local arterial input function for perfusion MRI using independent component analysis," *Magn. Reson. Med.*, vol. 52, no. 4, pp. 789–797, 2004.

[150] A. Araujo Giné, E.,, *The central limit theorem for real and Banach valued random variables*. NY: Wiley, 1980.

[151] A. Hyvärinen, "Fast and robust fixed-point algorithms for independent component analysis," *IEEE Trans. Neural Networks*, vol. 10, no. 3, pp. 626–634, 1999.

[152] H. L. M. Cheng, "Investigation and optimization of parameter accuracy in dynamic contrast-enhanced MRI," *J. Magn. Reson. Imaging*, vol. 28, no. 3, pp. 736–743, 2008.

[153] M. Novey and T. Adali, "Complex ICA by negentropy maximization," *IEEE Trans. Neural Networks*, vol. 19, no. 4, pp. 596–609, 2008.

[154] A. van den Bos, "Complex gradient and Hessian," *IEEE Proc. Vision, Image Signal Process.*, vol. 141, no. 6, pp. 380–382, 1994.

[155] M. Novey and T. Adalt, "Adaptable nonlinearity for complex maximization of nongaussianity and a fixed-point algorithm," in *Proceedings of the 2006 16th IEEE Signal Processing Society Workshop on Machine Learning for Signal Processing, MLSP 2006*, 2007, pp. 79–84.

[156] O. Bernard, J. D'hooge, and D. Friboulet, "Statistical modeling of the radio-frequency signal in echocardiographic images based on Generalized Gaussian distribution," in *2006 3rd IEEE International Symposium on Biomedical Imaging: From Nano to Macro - Proceedings*, 2006, vol. 2006, pp. 153–156.

[157] M. S. Davis, P. Bidigare, and D. Chang, "Statistical modeling and ML parameter estimation of complex SAR imagery," in *Conference Record - Asilomar Conference on Signals, Systems and Computers*, 2007, pp. 500–502.

[158] D. Gonzalez-Jimenez, F. Perez-Gonzalez, P. Comesana-Alfaro, L. Perez-Freire, and J. L. Alba-Castro, "Modeling Gabor coefficients via generalized Gaussian distributions for face recognition," *Proc. IEEE Int. Conf. Image Process*, vol. 4, pp. 485–488, 2007.

[159] W. Rudin, *Real and Complex Analysis*. New York: McGraw-Hill, 1987.

[160] M. Moradi, S. E. Salcudean, S. D. Chang, E. C. Jones, N. Buchan, R. G. Casey, S. L. Goldenberg, and P. Kozlowski, "Multiparametric MRI maps for detection and grading of dominant prostate tumors.," *J. Magn. Reson. Imaging*, vol. 35, no. 6, pp. 1403–13, Jun. 2012.

[161] D. L. Langer, A. J. Evans, A. Plotkin, J. Trachtenberg, B. C. Wilson, and M. A. Haider, "Prostate Tissue Composition and MR Measurements : Investigating the Relationships between ADC, T2, Ktrans,Ve and corresponding Histologic features," *Radiology*, vol. 255, no. 2, pp. 485–494, 2010.

[162] I. Ocak, M. Bernardo, G. Metzger, T. Barrett, P. Pinto, P. S. Albert, and P. L. Choyke, "Dynamic contrast-enhanced MRI of prostate cancer at 3 T: a study of pharmacokinetic parameters.," *AJR. Am. J. Roentgenol.*, vol. 189, no. 4, p. 849, Oct. 2007.

[163] J. G. Korporaal, C. a T. van den Berg, M. J. P. van Osch, G. Groenendaal, M. van Vulpen, and U. a van der Heide, "Phase-based arterial input function measurements in the femoral arteries for quantification of dynamic contrast-enhanced (DCE) MRI and comparison with DCE-CT.," *Magn. Reson. Med.*, vol. 66, no. 5, pp. 1267–74, Nov. 2011.

[164] C. Li, M. Chen, S. Li, X. Zhao, C. Zhang, and C. Zhou, "Diagnosis of Prostate Cancer : Comparison of MR Diffusion Tensor Imaging , Quantitative Dynamic Contrast- Enhanced MR Imaging and the Two Techniques Combined at 3 . 0T," in *International Society of Magnetic Resonance in Medicine*, 2011, vol. 19, p. 3069.

[165] M. Heisen, X. Fan, J. Buurman, N. A. W. Van Riel, S. Gregory, M. Bart, and H. Romeny, "The Influence of Temporal Resolution in Determining Pharmacokinetic Parameters From DCE-MRI Data," *Magn. Reson. Med.*, vol. 63, no. 3, pp. 811–816, 2010.

[166] F. Peeters, L. Annet, L. Hermoye, and B. E. Van Beers, "Inflow Correction of Hepatic Perfusion Measurements Using T 1-Weighted, Fast Gradient-Echo, Contrast-Enhanced MRI," *Magn. Reson. Med.*, vol. 51, no. 4, pp. 710–717, 2004.

[167] S. C. L. Deoni, B. K. Rutt, and T. M. Peters, "Rapid combined T1 and T2 mapping using gradient recalled acquisition in the steady state.," *Magn. Reson. Med.*, vol. 49, no. 3, pp. 515–26, Mar. 2003.

[168] H.-L. M. Cheng and G. A. Wright, "Rapid high-resolution T(1) mapping by variable flip angles: accurate and precise measurements in the presence of radiofrequency field inhomogeneity.," *Magn. Reson. Med.*, vol. 55, no. 3, pp. 566–74, Mar. 2006.

[169] F. M. Fennessy, A. Fedorov, S. N. Gupta, E. J. Schmidt, C. M. Tempany, and R. V Mulkern, "Practical considerations in T1 mapping of prostate for dynamic contrast enhancement pharmacokinetic analyses.," *Magn. Reson. Imaging*, vol. 30, no. 9, pp. 1224–33, Nov. 2012.

Appendix I

Relationship between Numerical Phantom and PK

Parameters

In the Tofts-Kety PK model it is assumed that the distribution of the contrast agent is due to diffusion of the solute through a semi-permeable membrane (blood vessel wall). However in calculating the K^{trans} parameter in the model several simplifications are made. In our numerical study we modeled the leaking process using diffusion, and added a range of diffusion values to the voxels of the images to account for a more general and realistic case. This model provided high variability in the perfusion parameter of the data to account for more complex situations of having different tissue types. We did not use K^{trans} directly as it would simplify the simulations, however the derivation of K^{trans} parameter from the diffusion parameter that was used is given below:

Consider a cylindrical tube (blood vessel) as shown in Figure I-1. Based on the mass continuity equation the difference between the total influx and outflux of the contrast agent equals the rate of change in the total amount of contrast agent in any section of the tube:

$$\frac{\partial c(t,x)}{\partial t} = -\nabla J(t,x)$$

$$= \sum_{i \in inlets} J_i(t,x) - \sum_{o \in outlets} J_o(t,x)$$

(I-1)

where c is the contrast agent concentration and J is the contrast agent flux. We can write the following equation for the segment of the tube (at location x) that is shown in Figure I-1:

$$A\Delta x_1 \frac{\partial c_p(t,x)}{\partial t} = \left[F_p(t,x)c_p(t,x)\right] - \left[F_p(t,x+\Delta x_1)c_p(t,x+\Delta x_1)\right] - J_l$$

$$\approx -\Delta x_1 \frac{\partial\left[F_p(t,x)c_p(t,x)\right]}{\partial x} - J_l$$

(I-2)

where A is the cross section of the vessel, F_p is the flow of the solute through the tube, Δx_1 is the thickness of the segment, c_p is the contrast agent concentration inside the tube, and J_l is the flux of contrast agent through the tube's wall.

On the other hand according to Fick's Law of diffusion we have:

$$J_l = -D\frac{\partial c(t,x)}{\partial x}$$

$$= -D_w \frac{S\Delta x_1}{L}\frac{\left[c_E(t,x) - c_P(t,x)\right]}{\Delta x_2}$$

(I-3)

where S is the surface area of the tube wall (for the entire tube), L is the length of the tube, Δx_2 is the thickness of the tube wall, c_E is the contrast agent concentration outside of the tube close to the tube wall, and D_w is the diffusion coefficient through the pores of tube wall, thus:

$$A\Delta x_1 \frac{\partial c_p(t,x)}{\partial t} = -\Delta x_1 \frac{\partial\left[F_p(t,x)c_p(t,x)\right]}{\partial x} + D_w \frac{S\Delta x_1}{L}\frac{\left[c_E(t,x) - c_P(t,x)\right]}{\Delta x_2}$$

(I-4)

Some of the simplifying assumptions in compartmental Tofts-Kety model are:

1- F_p is constant and is not a function of x and t, or $F_p(t,x) = F_p$

2-   As the contrast agent arrives, it instantaneously gets mixed and provides a well mixed solute, thus c_p inside the tube (including at the outlet) is not a function of x, or $c_p(t,x) = c_p(t)$. Thus, the concentration change along the tube is the difference between the c that enters the tube (c_a) and the c that exits the tube (c_p).

Assuming that there is no contrast agent outside the tube at time zero we can ignore the $c_E(t,x)$ term. Using these assumptions we can rewrite the equation I-4 as:

$$\frac{v_p\Delta x_1}{L}\frac{\partial c_p(t)}{\partial t} = \Delta x_1 F_p \frac{\left[c_a(t) - c_p(t)\right]}{L} - \frac{D_w}{\Delta x_2}\frac{S\Delta x_1}{L}c_p(t)$$

(I-5)

133

dropping the term $\frac{\Delta x_1}{L}$, the above equation can be simplified to:

$$v_p \frac{\partial c_p(t)}{\partial t} = F_p[c_a(t) - c_p(t)] - D_w \frac{S}{\Delta x_2} c_p(t) \qquad \text{(I-6)}$$

This equation is similar to the governing equation of Tofts-Kety compartmental model which is given as [70]:

$$v_p \frac{\partial c_p(t)}{\partial t} = F_p[c_a(t) - c_p(t)] - PS c_p(t) \qquad \text{(I-7)}$$

where PS is the permeability surface area product. Comparing these two equations we have:

$$PS = D_w \frac{S}{\Delta x_2} \qquad \text{(I-8)}$$

The K^{trans} parameter in this Tofts-Kety model is given as:

$$K^{trans} = F_p \frac{PS}{PS + F_p} \qquad \text{(I-9)}$$

Thus, the K^{trans} parameter in terms of the diffusion coefficient in our simulation would be:

$$K^{trans} = F_p \frac{D_w S}{D_w S + F_p \Delta x_2} \qquad \text{(I-10)}$$
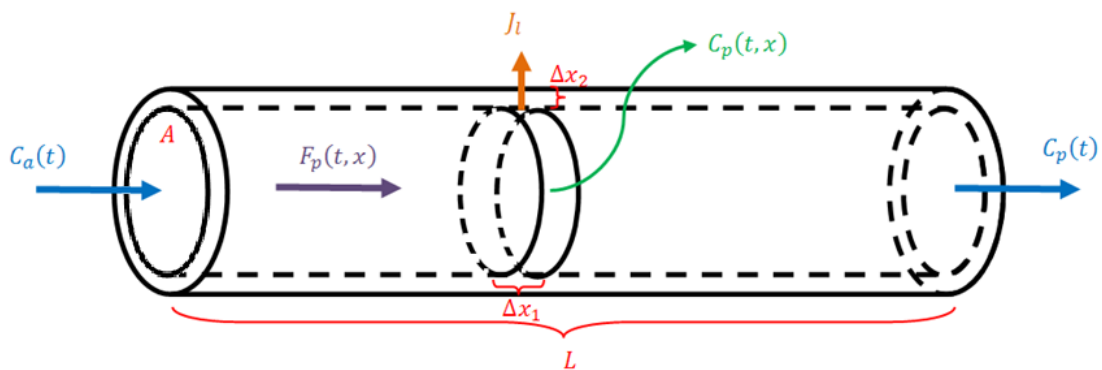

Figure I-1 A cylindrical blood vessel of length L and cross section area of A through which blood flows with flow rate F_p.

Appendix II

Inflow Effects in the Physical Tissue-Mimicking Phantom

The flow rate in the tubes of the physical tissue-mimicking phantom was very low $(0.047 \left[\frac{ml}{s}\right])$ which is in the same range as arterioles. Thus, the flow artifact in the physical tissue-mimicking phantom is negligible (less than 1%). The following gives a quantitative analysis of the flow artifact in our physical phantom (based on the analysis given by Peeters *et al.* [166]) which shows it was less than 1%:

If there is no flow, for a T_1 weighted SPGR sequence, assume that $M(n)$ is the longitudinal magnetization at $t = nTR$ (just before excitation). The magnetization at $t = (n + 1)TR$ can be written as (just before excitation):

$$M(n + 1) = \cos\alpha \, E_1 M(n) + M_0(1 - E_1), \qquad \text{(II-1)}$$

where $E_1 = \exp(-TR/T_1)$, α is the flip angle, and M_0 is the thermal equilibrium magnetization. When there is flow perpendicular to the imaging plane, we assume a compartmental model of the slice where we have 2 populations of spins:

1- Fresh spins flowing into the slice $(f(n))$

2- Spins that remain in the slice between two excitations $(1 - f(n))$

The fraction of the fresh spins in the voxel that arrive during one repetition time (TR) interval is given as:

$$f(n) = \frac{1}{L} \int_{nTR}^{(n+1)TR} v(t)dt \qquad \text{(II-2)}$$

where L is the slice thickness and $v(t)$ is the flow velocity. The longitudinal magnetization at time $t = (n + 1)TR$ could be written as:

$$M(n + 1) = [1 - f(n)]\cos\alpha \, E_1 M(n) + [1 - f(n)]M_0(1 - E_1) + f(n)M_i(n) \qquad \text{(II-3)}$$

where $M_i(n)$ is the longitudinal magnetization of the fresh spins entering the slice at time $t = nTR$. In the case of our experiments we have:

Diameter of each tube $D = 200$ [µm], thus the cross section of a tube is:

$$s_i = \pi \left(\frac{D}{2}\right)^2 = \pi(100 \, [\mu m])^2 = \pi \times 10^{-8} \, [m^2]$$

We had 100 tubes in the phantom, thus the total cross section is:

$$S = 100 \times s_i = \pi \times 10^{-6} \, [m^2]$$

The flow rate is $flow = 0.047$ $[\frac{ml}{s}]$, thus the velocity of the flow is:

$$v = \frac{flow}{S} = 0.0149 \, [\frac{m}{s}] = 14.9 \, [\frac{mm}{s}]$$

The slice thickness in DCE-MRI data of our physical tissue-mimicking phantom was $L = 5$ [mm] and $TR = 12.5$ [ms], thus the fresh spin fraction is:

$$f(n) = \frac{1}{5} \int_0^{12.5 \times 10^{-3}} 14.9 dt = 0.037 \approx 0.04 \qquad \text{(II-3)}$$

The fraction of the fresh spins in the voxel is less than four percent (f(n)<0.04), thus it is negligible in our experiments.

Appendix III

Converting MR Signal Intensity to Contrast Agent

Concentration

Dynamic contrast enhanced (DCE)-MR imaging involves intravenous injection of a bolus of low molecular weight contrast agent, e.g., Gadolinium (Gd)-DTPA, followed by repeated T_1-weighted imaging of the tissue to track the passage of the bolus through its vasculature. The spoiled gradient recalled (SPGR) pulse sequence is used for DCE-MR imaging whose signal intensity in a voxel without any contrast agent is expressed as:

$$SI(0) = g\rho \, sin \, \alpha \, \frac{1 - exp(-TR/T_1)}{1 - cos \, \alpha \, exp(-TR/T_1)} exp(-TE/T_2^*) \qquad \text{(III-1)}$$

where $SI(0)$ is the signal intensity measured in the voxel at $t = 0$ (pre-contrast), g is the scanner gain, ρ is the proton density, α is the flip angle, TE is the echo time, TR is the repetition time, T_2^* is the transverse relaxation time, and T_1 is the longitudinal relaxation time of the tissue. As the contrast agent arrives in the tissue, it changes magnetic characteristics of the tissue and hence changes its signal intensity which will be explained in the next subsection.

Converting MR signal intensity to Contrast Concentration

Once the gadolinium-based (e.g. Magnevist) contrast agent enters the voxel it alters the transverse and longitudinal relaxation times which can be explained by the following [101]:

$$\frac{1}{T_1} = \frac{1}{T_{10}} + R_1c(t), \qquad \frac{1}{T_2^*} = \frac{1}{T_{20}^*} + R_2c(t) \qquad \text{(III-2)}$$

where T_{10} and T_{20}^* are the longitudinal and transverse relaxations times with no contrast agent respectively. T_1 and T_2^* are the longitudinal and transverse relaxations times after the contrast agent enters the voxel. $R_1 = 3.3 \left[\frac{1}{mM \cdot s}\right]$ and $R_2 = 5.2 \left[\frac{1}{mM \cdot s}\right]$ are the longitudinal and transverse relaxivities of the contrast agent (which is Magnevist in our prostate cancer studies) at main magnetic field strength of $B_0 = 3$ [T], and $c(t)$ is the contrast agent concentration in the voxel at time t. The MR signal intensity of the voxel at $t = t_0$, after administration of contrast agent, is given by:

$$SI(t_0) = g\rho \sin\alpha \; \frac{1 - exp\left(-TR\left(\frac{1}{T_{10}} + R_1 c(t_0)\right)\right)}{1 - \cos\alpha \, exp\left(-TR\left(\frac{1}{T_{10}} + R_1 c(t_0)\right)\right)} \, exp\left(-TE\left(\frac{1}{T_{20}^*} + R_2 c(t_0)\right)\right) \qquad \text{(III-3)}$$

In order to calculate the contrast agent concentration in the voxel at each time point the term T_{10} has to be calculated first (next section). Then, the right and left hand sides of equation III-3 are divided by the right and left hand sides of equation III-1 respectively, and the resultant equation is solved for the only unknown (note that the term T_{20}^* cancels out when dividing the two equations) in the equation which is $c(t_0)$.

Pre-contrast T1-mapping (Multiple Flip Angles)

The native T_1 value (T_{10}) of the tissue (also known as T_1-map) is needed to convert the MR signal intensity to contrast agent concentration. Rapid and accurate measurement of this parameter is challenging, however there are several methods for calculating T_1-map such as 1) multiple inversion time (TI) method using inversion recovery spin echo (IR-SE) imaging [167], and 2) multiple flip angle method using spoiled gradient recalled-echo (SPGR) imaging [168]. In this thesis the latter approach was used.

In multiple flip-angle imaging method a set of two or more pre-contrast SPGR images are acquired with variable flip angles [168] and are used to calculate the T_1-map. The advantages of this method over the multiple inversion time method are low power deposition, and low spatial distortion. Moreover, the accuracy of multiple flip angle method has been shown to be similar to multiple inversion time method, and more importantly has significant reduction

in imaging time [168]. Another advantage of this method is that it provides T_1-map using the same imaging parameters that are used in DCE-MRI acquisition.

The signal intensity of SPGR imaging is used for T_1-map analysis (neglecting the T_2^* effects):

$$SI(\alpha_i) = M_0 \, sin \, \alpha_i \, \frac{1 - exp(-TR/T_1)}{1 - cos \, \alpha_i \, exp(-TR/T_1)} \qquad \text{(III-4)}$$

where $M_0 = g\rho$. Having several measurements for each voxel in the image (one measurement for each flip angle), the above equation is solved for the value of T_{10} (the parameters α and TR are known and M_0 is constant).

In order to solve for T_{10} in equation III-4, α_i is assumed to be the flip angle that is applied by the scanner ($\alpha_i^{applied}$) which might not be the same as the flip angle that is seen by the tissue at a given spatial coordinate (α_i^{actual}). This causes error in the calculated T_{10} value which has to be corrected. Fennessy *et al.* [169] introduced a flip angle correction method for T_1-map calculation of prostate tissue using the known T_{10} value of the pelvic muscle. The method substitutes the α_i^{actual} in equation III-4 with $K\alpha_i^{applied}$ ($\alpha_i^{actual} = K\alpha_i^{applied}$) where K is the correction factor. The correction factor is calculated by fitting the pelvic muscle data whose T_{10} is known (e.g. 1420 [ms] at 3 [T]) with free parameters K and M_0 using equation III-4 [169]. Once K is calculated, the corrected flip angle is used in equation III-4 for each voxel of the prostate tissue to generate its T_1-map.

Appendix IV

Vascular Input Function (VIF) Normalization

A normalization step was introduced in chapter 5 of the thesis which was derived based on the fact that if two VIFs satisfy the tofts-Kety model equations for a specific tissue type, their areas under the curve (AUC) have to be equal. This appendix proves this assumption:

The Tofts-Kety model equation (equation 1-16) can be reformulated as:

$$\frac{dc_t(t)}{dt} = K^{trans}c_p(t) - \frac{K^{trans}}{v_e}c_t(t) \tag{IV-1}$$

If we calculate the integral of both sides of equation IV-1 with respect to time we have:

$$\int_0^\tau \frac{dc_t(t)}{dt} = \int_0^\tau K^{trans}c_p(t) - \int_0^\tau \frac{K^{trans}}{v_e}c_t(t) \tag{IV-2}$$

The above equation can be simplified as:

$$c_t(T) = K^{trans}\left(\int_0^T c_p(t) - \frac{1}{v_e}\int_0^T c_t(t)\right) \tag{IV-3}$$

where T is the time point for the last acquired DCE-MRI frame. As both $c_p(t)$ and $c_t(t)$ are zero before the arrival of contrast agent in the prostate tissue, we assume that time zero ($t = 0$) is the time at which contrast agent arrives in the prostate tissue. The AUC of the VIF is:

$$\int_0^T c_p(t) = \frac{1}{K^{trans}}\left(c_t(T) - \frac{1}{v_e}\int_0^T c_t(t)\right) \tag{IV-4}$$

The PK parameters are characteristics of the tissue and $c_t(t)$ is derived directly from MRI measurements, thus they do not depend on the VIF calculation method. Thus, if two VIFs satisfy equation 1-16, their AUC has to be equal. These results are shown for Tofts-Kety model but they hold for other models as well.